Mineralisation of collagen studied by *in situ* X-ray and Raman spectroscopy

Emma Tong

PhD

University of York

School of Physics,

Engineering and Technology

August 2023

Abstract

Bone is a fascinating biocomposite material combining hardness and toughness through the hierarchical and nano-level organisation of a hard mineral (hydroxyapatite) and a soft protein (collagen type I). The mechanism behind the mineralisation of the collagen matrix, which is constituted of fibrils, is still a central problem in the field of biomineralisation research. Current understanding is that the mineral is formed via an amorphous precursor phase that infiltrates the collagen fibrils and subsequently crystallises. However, the mechanisms controlling infiltration and crystal growth remain unclear. To identify the processes involved in the precursor transport and phase transformation across varying length scales, an *in vitro* model system was used, the polymer-induced liquid-precursor (PILP) process, by which collagen mineralisation can be achieved both intra- and extra-fibrillar [1][2]. The *in vitro* model system employs a process-directing polymer e.g. osteopontin a biogenic non-collagenous protein (NCP) in native bone formation. Using a bespoke *in-situ* heated liquid cell to maintain physiological temperatures, for use in a Raman spectrometer and on I22 beamline, collagen mineralisation was successfully achieved and observations were made in real time of the transition from an amorphous precursor phase through to the formation of hydroxyapatite (HAP) crystals. nano- X-ray fluorescence (n-XRF) was performed on I14 beamline which showed the distribution of Ca and P across the fibre revealing there was a higher degree of mineralisation on the edge of the fibre than in the centre of the fibre. In addition, transmission electron microscopy (TEM) was used to examine the mineralised collagen fibre, which revealed HAP crystals both on the surface and embedded within the collagen fibre. Our findings allow for the quantitative characterisation of the kinetics of precursor infiltration and crystallisation across different length scales.

Contents

List of Figures

List of Tables

Acknowledgements

I would like to thank several people who have made this work possible.

First and foremost I would like to thank my supervisors Professor Roland Kröger (University of York) and Dr Julia Parker (Diamond Light Source, Oxford, UK) for their support, guidance and encouragement throughout the course of my PhD and also for their patience and time attempting to explain physics to an archaeologist. I would like to say a special thank you to Julia for the many hours of help analysing the SAXS and WAXS data throughout lockdown.

I am grateful for the opportunity I was given to conduct research at Diamond Light Source, Oxford, UK. It was a truly fascinating and fantastic experience.

I thank the staff at the York JEOL Nanocentre and the Biology department at the University of York for the use of their electron microscopy facilities. I would like to extend my thanks to Meg Stark and Karen Hodgkinson for their help in preparing my samples for TEM analysis. I would also like to thank John Emery and Tim Ayers of the Electronics department at University of York for all their help in designing and making the *in situ* heating cell. I would like to thank Paul Gunning at Smith and Nephew.

Finally, I want to thank my family for supporting me all the way. Most importantly, I want to thank my children Ewan and Beau for being my constant source of "get up and go", I love you both dearly.

Declaration

I declare that this thesis is a presentation of original work and I am the sole author. This work has not previously been presented for an award at this, or any other, University. All sources are acknowledged as References.

Emma Tong

Publications

Wingender, B., Tong, E., Emery, J., Gower, L., & Kröger, R. (2019). Time- Resolved in situ Raman Spectroscopic Observations of a Biomineralization Model System. Microscopy and Microanalysis, 25(S2), 826-827. doi:10.1017/S1431927619004860

Chapter 1 **Introduction**

The motivation of this thesis has two main objectives **1)** to study the biomineralising process at varying length scales using advanced techniques to further existing knowledge within the biomineralisation community on this elusive process and to move a step closer in answering one of the fundamental questions that remains unanswered: What are the dynamics and mechanisms of the formation of hydroxyapatite at the organic (type 1 collagen) / inorganic interface (hydroxyapatite). **2)** to aid the biomedical industry in developing biomedical applications. Bone is one of the strongest naturally forming biocomposite materials and the ability to further understand and mimic its formation would be both beneficial to scholars aiming to solve the ambiguous mechanisms of the organic- inorganic interface in bone and to the biomedical industry to produce synthetic bone like material.

Biomineralisation is a phenomenon whereby living organisms produce minerals. The process of biomineralisation leads to the development and formation of complex biological structures, such as silicates in algae and diatoms, calcium in invertebrates and calcium phosphates and carbonates in the hard tissues of vertebrates [3]. It has been a subject of interest to scholars from various disciplines since the early 1900's. The subject saw major works first published in the first half of the century by scholars O.B Bøggild [4] W.J Schmidt (1924) [5], F.W Clarke (1922) [6]. However, it was the advancements in microscopy and the invention of the electron microscope by Ernst Ruska (1938) that allowed scholars to for the first time observe collagen and bone at the nanometer level and to shed light on the complexities of the mineralisation mechanisms in detail. As a result, biomineralisation entered a new era of interest.

One area of the mineralisation process that remains elusive is the dynamics of the formation of hydroxyapatite at the organic/inorganic interface. Amorphous calcium phosphate (ACP) and octacalcium phosphate (OCP) are considered as the first precipitates in mineralisation which then via complex physiochemical processes morph into the crystal phase, HAP [7][8]. However, this hypothesis is still widely debated. It is postulated that HAP is formed via an amorphous precursor phase which infiltrates the collagen fibrils before crystallisation [1]. The extracellular matrix (osteoid), which regulates the process of collagen mineralisation is made up primarily of type 1 collagen fibrils including water, ions and several different non-collagenous proteins (NCP's) and other macromolecules [9][10]. Each NCP plays a different role in the mineralisation process such as control of cell

proliferation, cell–matrix interactions, and mediation of hydroxyapatite deposition [9]. The collagen fibrils are aligned parallel to each other in a staggered formation, creating gap and overlap regions. HAP crystals nucleate in the gap regions between the collagen fibrils, once the gap regions have been filled, the HAP crystals proceed to penetrate the collagen fibrils (intrafibrillar mineralisation) and continue to grow along the surface (extrafibrillar mineralisation) in such a way that they are oriented with their c-axes parallel to the longitudinal axis of the fibrils [11][12]. This project will conduct a detailed study of the growth of collagen/apatite composites and investigate the collagen- mineral interface over a range of length scales from the nano to microscale in both biomimetic systems and bone in an attempt to shed new light on this complex physiological/chemical process.

1.1. Bone Composition and Structure

The skeleton is the framework of the human body. It not only serves as a structural support but also as a protective encasement for vital organs. At birth, the human skeleton is composed of 270 bones. Once the human skeleton has fully matured, typically around the age range of 18-20 the total number of bones in the adult human skeleton decreases to 206 this is because various bones fuse. The human skeleton performs several major functions; support, movement, protection, production of blood cells, storage of minerals, and endocrine regulation [10]. Bone is a heterogeneous hierarchical structured composite material [10][13][11]. The major components of bone are type 1 collagen fibrils, hydroxyapatite crystals ($Ca_{10}(PO4)_6(OH)_2$) and water [6,7,8]. The organic component of bone is type 1 collagen, which gives bone its elasticity. The inorganic component of bone is hydroxyapatite, which gives bone its stiffness and rigidity.

1.1.1 Macrostructure

To understand bone and the complexities of bone structure and the mineralisation process, it is important to understand the complex hierarchical structures that bone possesses. It has long been accepted that bone has seven levels of hierarchy [11] (Figure 1.1). However, more recently Reznikov *et al* [14] have proposed twelve levels of hierarchy (Figure 1.1).

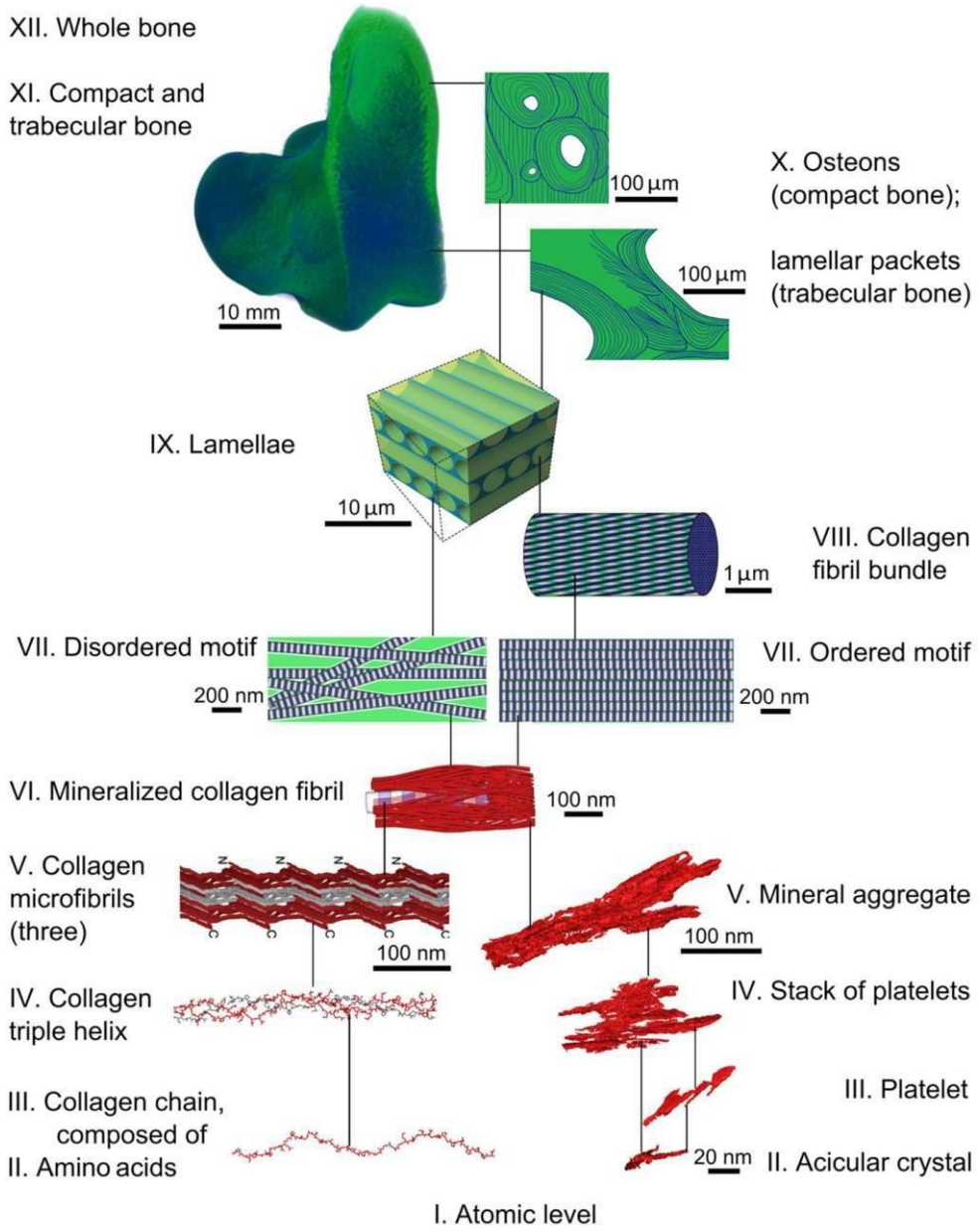

Figure 1.1 Twelve structural levels of bone. At the macro scale the whole bone (XII) is formed of compact and trabecular bone (XI) which is formed of cortical osteons and lamellar packets (X) which contain lamellar bone made of lamellae (IX) which is composed of ordered collagen motifs (VII) that form collagen fibril bundles (VIII) surrounded by the disordered collagen motif (VII). At the atomic scale, the collagen fibril bundles (VIII) are composed of collagen fibrils (V) that are made up of the collagen triple helix (IV) which is made up of a collagen chain (III) composed of amino acids (II). The mineralised collagen fibril (VI) contain the mineral aggregate (V) which is made up of stacked crystals (IV) which are made up of platelets (III) and acicular crystals (II). For ease of reading, the hierarchical structure has been explained from macroscale to atomic scale. [14].

At the macroscale, all bone has two structural components, cortical bone and trabecular (cancellous) bone (Figures 1.1 and 1.2). Cortical bone, is a compact, dense bone that can be seen in the diaphysis (shafts) and on the external surface of bones, and constitutes 80% of skeletal mass [10]. The denseness of cortical bone allows it to withstand higher stresses than trabecular bone. Cortical bone also provides a protective layer around vital organs, e.g. skull to protect the brain. Trabecular bone, found in the epiphysis (extremities) of long bones and short bones, constitutes 20% of the skeletal mass and is a lightweight, porous bone with a honeycomb

like structure formed of thin bony spicules (trabeculae) [10]. The combination of the hardness of the cortical bone and the cortical bone and the honeycomb like structure of trabecular bone provides bone with maximum mechanical strength and elasticity making bone one of the strongest biological materials [8].

1.2.1 Microstructure

At the microstructural level, two types of bone can be identified, woven bone and lamellar bone. Woven bone (primary bone) is the first bone to form in the embryonic skeleton as the foetus matures this is then replaced with lamellar bone. Woven bone is also formed in adults where there is damage, fractures or breaks. Woven bone forms rapidly whereby collagen fibrils lay down in an unorganized orientation making woven bone weaker. Woven bone is then replaced by lamellar bone. Lamellar bone (secondary bone) forms much slower and in a highly organized manner of concentric layers filled with many collagen fibrils, arranged in opposite directions in alternating layers making lamellar bone much stronger [15][11]. The concentric layers of lamellar bone are the principle structural unit of cortical bone known as osteons [15][11] (Figure 1.2).

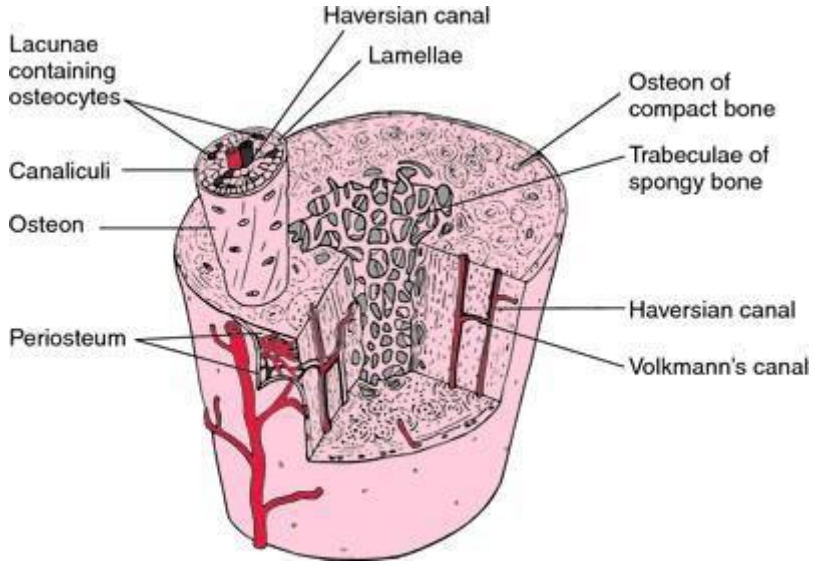

Figure 1.2 Lamellar bone also known as secondary bone (adult bone) consists of highly organised sheets of mineralised osteoid. Lamellar bone is made up of two types of bone, compact bone and spongy bone. A layer of connective tissue called the periosteum surrounds both types of bone. In compact bone the lamellae are organised onto concentric circles which surround the Haversian canal. The whole structure is known as the osteon, the functional unit of bone. The Haversian canals are connected by the Volkamans canals. Osteocytes are located between the lamellae in small cavities known as lacunae. The lacunae are interconnected by a series of channels known as canaliculi.

The Haversian canal is one of several longitudinal canals approximately 0.05mm diameter which contain blood vessels, nerve filaments, and lymphatic vessels [11]. The Haversian

system (Osteon) is the principle structural unit of cortical bone. Osteons are approximately 400mm in length and 200mm wide [11]. They are aligned parallel to the long axis of the bone. They are cylindrical in shape and consist of concentric lamellae which surround the Haversian canal (Figure 1.2). The Haversian canal is the sole route for blood supply for the osteocytes. The Haversian canal is interconnected to the Volkmann's canal via an intricate network which carries nutrients through bone.

1.3.1 Collagen

When observing bone at the nano structural level, bone tissue can be defined as two composite materials, collagen and hydroxyapatite. Collagen is a natural insoluble, fibrous protein and is the most abundant protein in the body. Type 1 collagen represents the major organic component of bone, approximately 85% - 90% of the total bone protein [10], [11], [16], [17]. Collagen type 1 is composed of 3 polypeptide alpha chains, two identical $\alpha 1(I)$, chains and 1 $\alpha 2(I)$ chain (Figure 1.3). Individual collagen polypeptide chains contain approximately 1000 amino acids [18]. Collagen has a distinctive regular arrangement of amino acids (Figure 1.3).

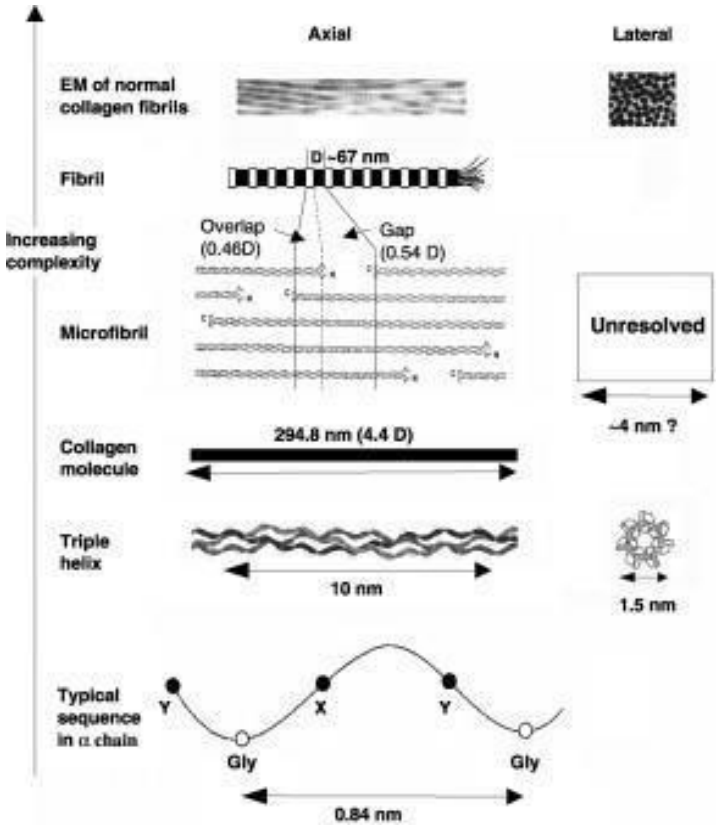

Figure 1.3 The structural hierarchy of the collagen peptide chain to the collagen fibril is shown in the figure above from the bottom to the top. The structural hierarchy of the collagen peptide chain to the collagen fibril is shown in the figure above from the bottom to the top. [18].

The arrangement follows the sequence Gly-X-Y; X can be any amino acid but it is usually a proline and Y is usually hydroxyproline [10], [11], [16], [17], [19]. Proline residues point

outwards from the helix while the smaller glycine side chains face inwards; glycine is the smallest amino acid and is required in every third position in order to occupy the limited space in the centre of the triple helix [16]. It is this distinct sequence, the hydrogen bonds linking the peptide bond NH of a glycine residue with a peptide carbonyl (C═O) group in an adjacent polypeptide, which help hold the three chains together [16]. Each individual polypeptide chain has a left-handed helix formation. These three helices weave around one another to form a right handed triple helix called tropocollagen measuring 300 nm in length and 1.5 nm in diameter [16][20]. Short sections at either end of the collagen chains, N- and C-propeptide domains are cleaved by specific proteases to allow the collagen molecules to form stable collagen fibrils with a normal structure. The cleavage of procollagen propeptides exposes telopeptides. Telopeptides do not possess the triple helical arrangement and the cleaved c and n termini do not conjoin leaving a gap and it is proposed that it is in this gap region that nucleation takes place (Figure 1.3) [16] [20]. The triple helices assemble in a quasi-hexagonal formation forming a parallel array of collagen micro fibrils , resulting in a gap/overlap pattern, known as the periodic d- spacing of 68-70 nm (Figure 1.3). This model is known as the quarter stagger model and was proposed by Petruska and Hodge [21] and it is this model that is largely accepted for describing fibrillar organisation.

1.4.1 Bone mineral and Mineralisation

Bone mineral is a nano crystalline solid formed by the precipitation of calcium and phosphate. The main crystal formed in bone is hydroxyapatite $Ca_{10}(PO4)_6(OH)_2$, and is essentially the sole naturally occurring mineral in human bone, constituting approximately 60% weight [22]. Hydroxyapatite has a hexagonal structure and is a form of calcium phosphate also containing traces of carbonate, magnesium and acid phosphates [23]. However, other crystals are known to occur in bone in the form of OCP $Ca_8H_2(PO4)_6 \cdot 5H_2O$. HAP and OCP have very similar chemical structures making it very difficult to differentiate between the two [24]. OCP has a triclinic structure and has a hydrated layer, therefore is less stable than HAP and is known to biodegrade *in vivo* [24]. The tightly packed arrangement of nanocrystals surrounds and occupy the collagen fibrils that act as a scaffold, which the mineral crystals nucleate and grow and, at the same time, control their growth habits (size and orientation) [25][26]. There continues to be much debate regarding the morphologies of the mineral crystals as to whether they are platelet shaped or needle like in shape. The size of the mineral crystals is still also contested but again the general acceptance is their thickness is in the range of 2 to 7 nm, a length of 15 to 200 nm and a width of 10 to 80 nm [10], [26], [27]. The exact mechanism surrounding bone mineralisation is unknown and continues to be widely debated. The earliest theory to be

proposed was the classical nucleation theory that describes how the bone mineral is formed by the precipitation of Ca and P ions from the surrounding interstitial fluid and the formation of bone mineral does not involve a precursor [7], [28]–[30]. [30][31][32] In recent years, studies have shown that bone mineral forms via a precursor phase and the mechanism is controlled by kinetic and thermodynamic parameters [8], [30]-[32]. The thermodynamic parameters that govern collagen mineralisation are pH, ionic strength and temperature all of which affect the dynamics of the mineralisation process including the occurrence of intermediate phases. Meyer and Eanes [8] conducted a thermodynamic analysis of the intermediate phases of the mineralisation process and by controlling these parameters; the data obtained in their study identified three distinct consecutive chemical phases in the initial formation in the apatitic crystals whereby the mineral initially precipitates as the thermodynamically least stable form ACP which then transforms into a crystalline phase with characteristic properties of OCP and if left long enough in the precipitation solution reaches the most thermodynamically stable phase HAP. The data obtained in the *in situ* and *ex situ* experiments, conducted for the purpose of this thesis, strongly suggest, that this sequence of precipitation occurs also in the context of PILP induced collagen mineralisation as discussed in the ensuing chapters.

1.5.1 Non-collagenous proteins (NCPs)

Non-collagenous proteins (NCPs) are known to promote mineralization and bone formation. All NCPs have different roles to play in the mineralization process such as control of cell proliferation, cell–matrix interactions, and mediation of hydroxyapatite deposition [9]. Although collagen acts as a scaffold in the mineralization process it is not known to initiate nucleation of hydroxyapatite [9]. The major structural proteins present within the extracellular matrix are proteoglycans, glycoproteins, and γ -glutamic acid-containing proteins [9]. Osteopontin, Osteonectin, Osteocalcin and fetuin-A are known to play a role the mineralisation process. Osteopontin (OPN), also known as bone sialoprotein1 (BSP1), is a secreted glycoprotein produced by osteoblasts [33]. OPN in bone is thought to control the crystal size and shape of hydroxyapatite. Further studies have shown that OPN adsorbs tightly to HAP and is an inhibitor of crystal growth [34]. Osteonectin is an acidic glycoprotein and is known to bind to type I collagen and hydroxyapatite crystals, and is reported to promote crystal growth [35]. Osteocalcin contains three γ-carboxylglutamic acid (Gla) residues that are known to bind calcium, however, its role in mineralization remains uncertain [34]. Fetuin-A, also known as α2-Heremans-Schmid glycoprotein, plays a critical role in intrafibrillar mineralisation [35]. The presence of fetuin A promotes mineral growth exclusively within the fibril, whereas in its

absence the mineral grows outside the fibril [35].

It is purported that the liquid phase mineral precursor infiltrates the collagen fibrils via capillary action initially in the gap regions inducing both extra and intra fibrillar mineralisation [1], [49]. The acidic polymer is added to the mineralisation solution super saturated with respect to calcium and phosphate, in turn inducing liquid-liquid phase separation of ion-rich droplets, referred to as PILP droplets [49]. After infiltrating the collagen scaffold, the ion rich PILP droplets undergo a mineralisation transition from a liquid-like amorphous calcium phosphate to crystalline bone apatite mineral, carbonated hydroxyapatite [49]. In order to achieve mineralisation of the collagen fibrils the PILP process was used. To form the PILP phase equal volumes of 9mM CaC12 and 4.2mM K_2 HPO_4 are mixed with a Tris- buffered saline solution containing 0.9% (w/v) NaCl to maintain the pH at 7.4. The process directing agent (OPN/pAsp/Fetuin A) (Lacprodan OPN-10, kindly supplied by Arla Foods) was added at a concentration of 50µg/ml to the calcium solution before mixing it with an equal volume of phosphate solution.

Much of the mineralisation work conducted by Professor Laurie Gower and her group have used pAsp (27000kDa) as the mineral directing agent. pAsp exists as several different molecular weights, 6800kDa, 14000kDa and 27000kDa. Professor Gower's group has mainly used pAsp of 27000kDa. For the purpose of this study several *ex-situ* experiments were conducted using the varying molecular weights of pAsp to determine if the molecular weight played a role in the in the time scale of mineralisation. This is a well-established and reliable acidic polymer for the successful mineralisation of collagen fibres, however, *ex situ* experiments have shown to require >72 hours for pAsp to promote mineralisation. OPN is a non-collagenous protein that is intricately involved in bone formation (ref). Using OPN as opposed to pAsp dramatically improves the kinetics of the reaction resulting in an effect mineralisation of the collagen within a few hours rather than 72 hours to 2 weeks as observed for pAsp. As the OPN induced mineralisation could be performed within 12 hours, it was chosen as main polymer, since providing stable conditions over time frames of several days for the *in situ* Raman spectroscopy and X-ray scattering experiments was found to be inhibitive. To compare the OPN results with another key NCP found in bone, fetuin-A was employed for a number of selected experiments also because it has been shown to be an effective promotor of bone mineralisation [35], [50], [51]. To our knowledge, no *in situ* studies of this kind have been conducted with fetuin-A (the resulting data are provided in the Appendix). Overall, OPN and fetuin-A were chosen as the process directing agents to investigate their influence on the

mineralisation process in the context of this study. OPN serves as a directing agent influencing the mineralisation process and fetuin-A is associated with the regulation of mineralisation in the body and known to be an inhibitor of the formation of bone mineral. By choosing the mentioned directing agents their role in extra and intrafibrillar mineralisation can be investigate particularly with respect to the direction and uniformity of mineral formation within the fibrils as well as the crystal size distribution and morphology. The aim is to obtain a better understanding of the molecular level interaction between mineralising agents and the collagen matrix with potential implications for tissue engineering, biomaterial design and regenerative medicine research.

1.6.1 Water

Water comprises about 25% of adult bone mass [36]. Despite being the third main component in bone water is the least studied component of bone matrix [11]. However, in recent decades studies have been carried out to establish the various roles water plays in bone [36], [37]. Using various techniques, such as solid state magnetic nuclear resonance (ssMNR) spectroscopy, three structural roles for water in bone have been identified from the microstructure to the molecular structure i) bulk water or pore water, ii) bound water, which can be further sub divided into loosely bound water and tightly bound water and iii) structural water [37] (Figure 1.4).

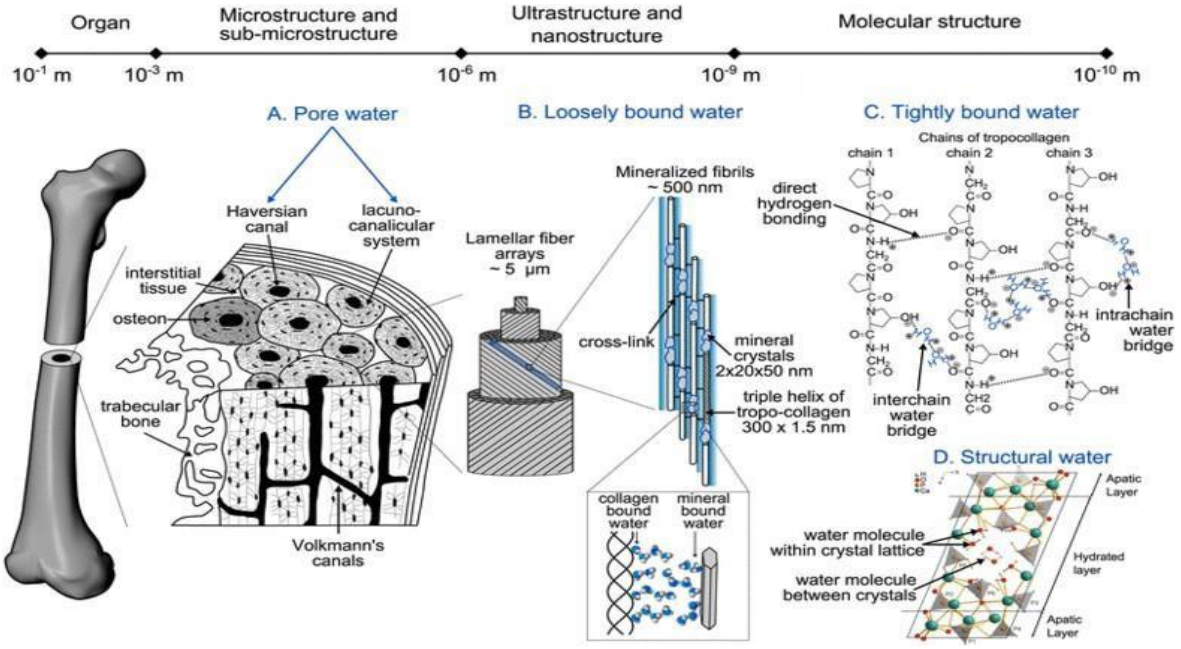

Figure 1.4 A schematic showing the presence of water in bone at different levels of organisation. A. Pore water at the macro level, B. Loosely bound water at the micro level, C. Tightly bound water and D. Structural water at the molecular level. [37].

Bulk water is one component of the unmineralised bone matrix (osteoid) and exists in the pores of the Haversian canal and the lacuno-canalicular system [37]. Water found in the osteoid is steadily replaced by calcium apatite during the mineralisation process, however this does not change the volume of the osteoid or the volume of the collagen fibrils nor their position [38]. Bulk water existing in the channels within the lacuno-canalicular aids the mineralisation process by promoting the flow and diffusion of calcium and phosphate ions in and out of bone tissue [39]. Loosely bound water is associated with the organic-inorganic interface and at the surface of the collagen fibrils. Studies have shown that, along with NCPs, loosely bound water

plays a significant role in influencing the orientation of mineral crystals via an amorphous calcium phosphate layer, as certain residues of the collagen molecule are hydrophilic (e.g., lysine, arginine, and hydroxyproline), water molecules naturally associate themselves with the matrix, therefore allowing the water molecules to bind to the apatite crystals influencing their orientation [37], [39], [40]. Tightly bound water directly affects the structure of the collagen triple helix, where the water molecules act as a bridge forming direct hydrogen bonds [41]. Structural water is the water found in the mineral crystal and between the crystal lattice [37], [42], [43].

1.7.1 Modelling and remodelling

It is easy to think of our bones as static entities, but actually, the human body is in a constant state of flux. Encased within our bones is a nano aqueous environment teaming with cell activity continuously modelling and remodelling our bone throughout our lives, through repeated cycles of bone resorption and rebuilding [10], [44], [45]. Bone remodelling relies on the unique integration and communication of two cell types, osteoblasts and osteoclasts [10], [45],[46] and is composed of three stages: resorption, reversal and formation [10].

Resorption: Osteoclasts are bone resorbing cells and originate from hematopoietic stem cells [47]. They are large multi nuclear cells (polykaryon) central to bone health, bone mass and bone quality [47]. The osteoclasts form a plasma membrane layer with a ruffled border to attach to the surface of the bone known as the ‘sealing zone’. They then secrete H+ ions and enzymes (cathepsin k) which dissolves the bone mineral matrix, as well as the flexible soft-tissue component of bone creating depressions in the bones surface known as Howship’s lacunae [45].

Reversal: The reversal phase is the point where bone resorption ceases and bone formation begins. After bone resorption is complete, the resorption pits contain activated mononucleated progenitor cells such as osteocytes, monocytes and preosteoblasts, which then begin the process of new bone formation [10], [48].

Formation: Osteoblasts are bone forming cells and originate from mesenchymal stem cells (MSC) [45], which are responsible for synthesizing and laying down bone material. Bone formation occurs in two phases, osteoblasts synthesise a matrix know as osteoid, the un-mineralized organic component of bone, made mostly of collagen type 1 and NCPs which is

secreted between the cell wall and new bone structure [45][46]. Osteoblasts secrete alkaline phosphate allowing the bone mineral to grow and therefore forming new bone [45]. Many osteoblasts become surrounded by this matrix and in turn transform into an osteocyte [10].

Osteocytes (living bone cells) help to maintain bone tissue, they inhabit small depressions in the calcified matrix called lacunae and communicate with one another via long cytoplasmic extensions that occupy tiny canals called canaliculi, which are used for exchange of nutrients and waste.

In an attempt to answer the fundamental question: What are the dynamics and mechanisms of the formation of hydroxyapatite at the organic (type 1 collagen) / inorganic interface (hydroxyapatite), several research objectives have been set out:

- Conduct a detailed study of the growth of collagen/apatite composites
- Investigate the collagen-mineral interface over a range of length scales from the nanoscale to microscale in collagen fibres
- Focus on the dynamics of the formation of hydroxyapatite in collagen
- Explore the imaging and spectroscopy of the crystallisation dynamics

A unique set of techniques will be employed to help answer these research questions and further our understanding of this complex biological process:

- Optical microscopy - macro and microstructure characterisation and imaging
- Raman spectroscopy - In situ time resolved experiments, monitor phase transformation during mineralisation process, chemical composition and structural information of materials
- Transmission electron microscopy - structural and crystallographic characterisation, chemical composition and imaging
- Small angle X- ray scattering (SAXS) - In situ time resolved experiments, monitor phase transformation during mineralisation process, chemical composition and structural characterisation

- Wide angle X- ray scattering (WAXS) - crystallographic information
- X- Ray fluorescence (XRF) - chemical composition

Combined, the data gathered from these set of techniques will not only complement one another but will have the ability to provide new in depth information on the mineralisation process adding additional knowledge to the open biological questions surrounding biomineralisation of collagen that remain ubiquitous

Chapter 2 **Materials and Methods**

2.1. Extraction of Type 1 Collagen fibres

Type 1 collagen fibres were surgically extracted from 10 week old male Sprague Dawley® rats (supplied by Charles River, Kent, UK). The anatomy of a rat tail consists of three layers. The innermost part of the tail- vertebra surrounded by a layer of tendons which is surrounded by the skin. The 15 tendons are attached to one another and to the bone by connective tissue such as cartilage and collagenous membrane. Each tendon is around 1cm in diameter and is made up of fibril bundles of about 100μm in diameter; these fibril bundles are aligned within the tendon (running parallel to the tendon's length) and are constructed of well aligned collagen fibrils, each being about 1μm in diameter. The rat tails were stored whole in the freezer at -80°C and removed 24 hours prior to dissection to allow them to thaw in preparation for dissection. The dissection was performed using a surgical scalpel and tweezers. A new scalpel blade was used for each dissection to ensure ultimate sharpness for clean incisions. All tools were cleaned with ethanol prior to dissection to prevent sample contamination. The dissection process begins with removing the skin. An incision is made running the full length of the tail and then the skin is peeled back and fully removed along with any connective tissues. The tendons containing the bundles of collagen fibres are attached to the vertebrae episodically. Each of the collagen fibres from within the tendons are carefully removed by simply pulling them out using sharp tweezers. Subsequent to extraction, the collagen fibres were placed in 4M NaCl to lyse any cells. The collagen fibres were then immersed in ethanol for 20 minutes to sterilise them. Following sterilisation, the collagen fibres were placed in 1X PBS for 5 minutes to remove any residual blood (this step was repeated three times). The fibres were then rinsed in DI water. Finally, the fibres were stored for future use at 4°C in 1X PBS with 0.02% sodium azide to prevent bacterial contamination (pers comm Dr Brian Wingender 2018). After discussions with Professor Laurie Gower and Dr Brian Wingender, it is thought that the collagen is able to be stored for 6 months when using this sample preparation. It should be noted that native collagen fibres were used for all of the experiments conducted in this project we did not use reconstituted collagen.

2.2. Mineralisation of collagen using the standard Polymer Induced Liquid Precursor (PILP) Process

It is purported that the liquid phase mineral precursor infiltrates the collagen fibrils via capillary action initially in the gap regions inducing both extra and intra fibrillar mineralisation [1], [49]. The acidic polymer is added to the mineralisation solution super saturated with respect to calcium and phosphate, in turn inducing liquid-liquid phase separation of ion-rich droplets, referred to as PILP droplets [49]. After infiltrating the collagen scaffold, the ion rich PILP droplets undergo a mineralisation transition from a fluidic amorphous calcium phosphate to crystalline bone apatite mineral, hydroxyapatite [49].

In order to achieve mineralisation of the collagen fibrils the PILP process was used. To form the PILP phase equal volumes of 9mM $CaC1_2$ and 4.2mM $K_2\ HPO_4$ are mixed with a Tris-buffered saline solution containing 0.9% (w/v) NaCl to maintain the pH at 7.4. The process directing agent (OPN/pAsp/Fetuin A) (Lacprodan OPN-10, kindly supplied by Arla Foods) was added at a concentration of 50µg/ml to the calcium solution before mixing it with an equal volume of phosphate solution.

Much of the mineralisation work conducted by Professor Laurie Gower and her group have used pAsp (27000kDa) as the mineral directing agent. pAsp exists as several different molecular weights, 6800kDa, 14000kDa and 27000kDa. Professor Gower's group have mainly used 27000kDa. For the purpose of this study several *ex-situ* experiments were conducted using the varying molecular weights of pAsp to determine if the molecular weight played a role in the in the time scale of mineralisation. This is a well established and reliable acidic polymer for the successful mineralisation of collagen fibres, however, *ex situ* experiments have shown it takes approximately >72 hours for pAsp to promote mineralisation making this particular acidic polymer unsuitable to use for the *in situ* time resolved experiments. Therefore, it was decided to concentrate on using OPN for the purposes of this project. OPN is a non-collagenous protein that is intricately involved in bone formation. Using OPN as opposed to pAsp dramatically improves the kinetics of the reaction, so mineralisation can occur in a matter of hours rather than 72 hours to 2 weeks. As the experiments conducted for this study were performed under *in situ* conditions, OPN was ideal because of the minimum time it takes to promote mineralisation.

It was also decided to use fetuin A. Fetuin A has been used to a much lesser extent but there are several studies showing that fetuin A plays a part in the mineralisation process [35], [50], [51]. To our knowledge, no *in situ* studies of this kind have been conducted using fetuin A. Due to time constraints, only one time resolved *in situ* experiment was conducted using fetuin A and several hours of data were not collected therefore the results can be found in the Appendix.

2.3. Sample preparation

After mineralisation the collagen fibres were subjected to a dehydration process through solvent series (25%, 50% 70% 90% 100% acetone) and embedded in epoxy resin in preparation for microtome sectioning.

Microtome sections of the mineralised fibres were kindly prepared by Meg Stark at the University of York, Biology department using the Leica EM UC7 ultra microtome. Cured resin blocks were trimmed down as far as the edge of the tendon (as this was where the resin infiltration was the best) and trimmed to a mesa shape for best sectioning. A 1 μm section was taken and the slide stained with toluidine blue to determine the best area for thin sections. The block was trimmed smaller for thin sections (100nm) which were collected onto 200μm copper formvar coated mesh grids in preparation for characterisation using electron microscopy (EM).

Chapter 3 **Experimental Techniques**

Many experimental techniques have been used over the decades in biomineralisation research; however, this chapter will only discuss the experimental techniques used in this project to investigate the collagen mineralisation process. A theoretical explanation is given for how the techniques used, work and how the data was collected, processed and analysed.

3.1. Electron Microscopy

Electron microscopy has the capabilities to provide detailed information on the nano scale interactions between collagen and hydroxyapatite crystals. A unique combination of electron microscopy, x-ray spectroscopy and synchrotron techniques will be employed (Figure 3.1). The basic principle of electron microscopy is analogous to that of light microscopy, only electron microscopy uses a beam of electrons as opposed to light waves to produce a magnified image of an object. Electrons have much shorter wavelengths, enabling better resolution. With spectroscopy, a beam of electromagnetic radiation is projected onto a sample obtaining information about the structure and properties of matter.

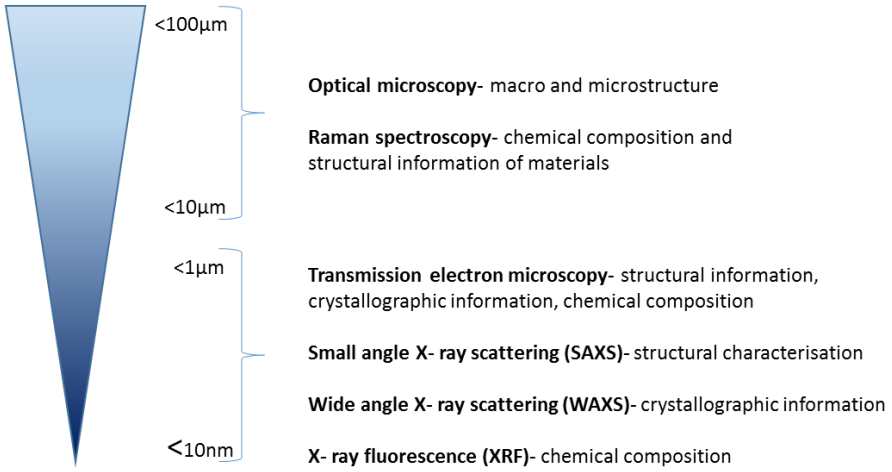

Figure 3.1 Schematic showing the techniques used for structural and chemical characterisation of the bone mineral.

3.1.1 Transmission electron microscopy (TEM)

The transmission electron microscope (TEM) is used to examine the structure, composition, crystallography, chemical composition and properties of materials [52]. The electron gun

within the TEM emits a high velocity beam of electrons that are focused into an ultra-thin beam using electromagnetic lenses, which are then transmitted through a sample (<100nm) (Figure 3.2). The interaction between the electrons and the sample forms a high resolution image or diffraction pattern [53]. The image is projected onto an imaging device allowing the sample to be observed and analysed. When electrons interact with the sample the electrons can be transmitted through the sample or scatter in various ways by either elastic (no loss of energy) or inelastic scattering (measurable loss of energy) [53] (Figure 3.3).

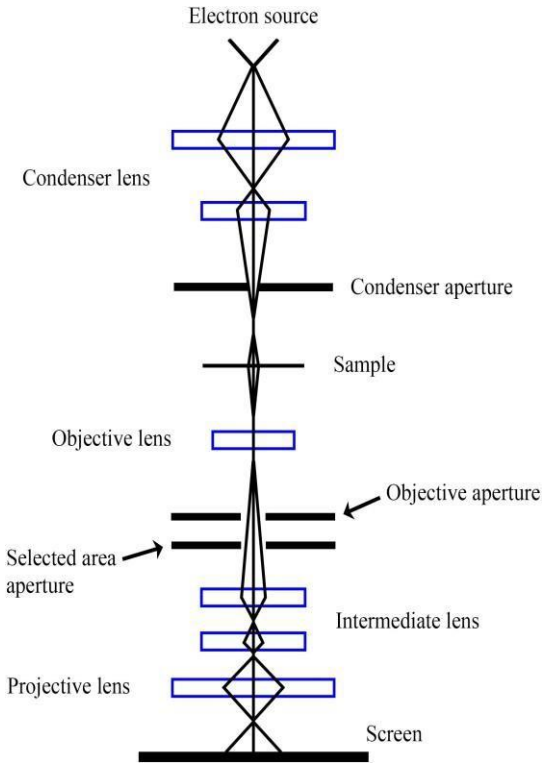

Figure 3.2 A schematic of a Transmission Electron Microscope (TEM).

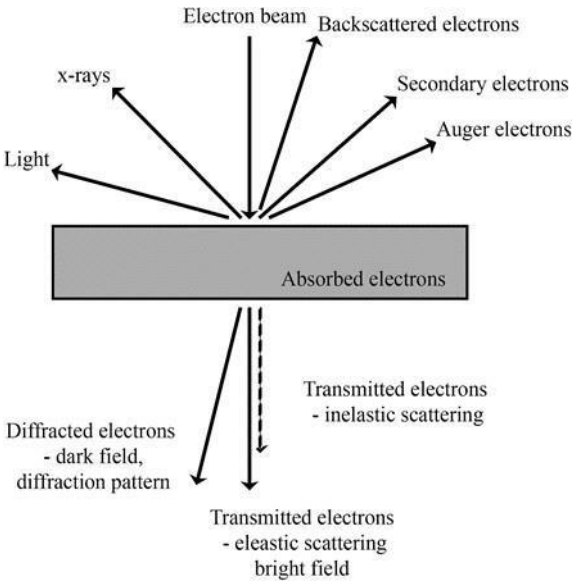

Figure 3.3 Schematic showing scattering events generated when electrons interact with a sample. (adapted from [52]).

Scattered electrons are also described as coherent and incoherent, which refers to their wave nature. Elastic electrons are coherent and usually scatter at low angles (1-10°), where the sample is thin and crystalline, and become more incoherent at higher angles (>10°) [54]. Inelastic electrons are incoherent and scatter at low angles (<1°) [55]. Scattering events are also categorised as forward scattering (<90°) or back scattering (>90°) this refers to the angle of scattering in relation to the beam [53]. The forward scattering events provide valuable structural and compositional information as well as diffraction patterns [53]. Where the sample is thicker, electrons are more backscattered (backscattered and secondary electrons) although, this provides useful information on topography [53]. It is imperative that the TEM sample is electron transparent (<100nm) to reduce/avoid multiple scattering events making interpretation of the sample less problematic. The two basic functions of the TEM are imaging and diffraction (Figure 3.4).

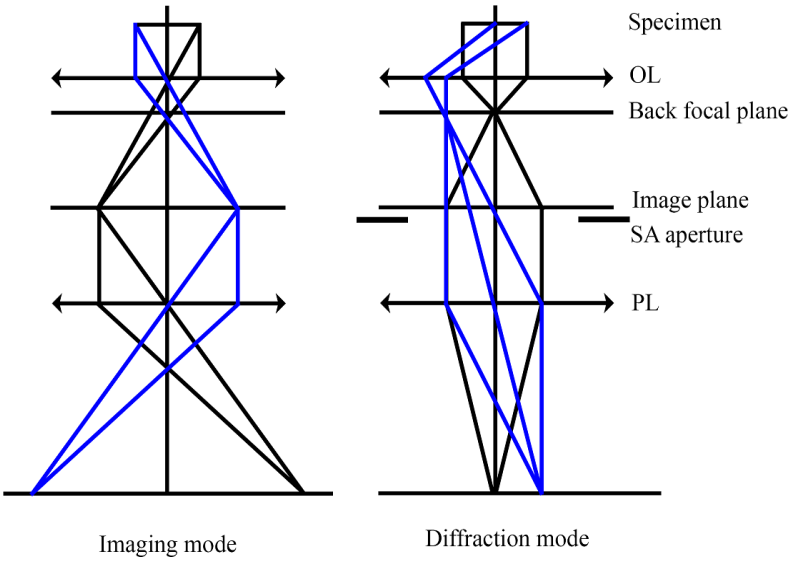

Figure 3.4 An optic ray diagram showing the imaging and diffraction modes in TEM.

Diffraction patterns provide information on the crystalline nature of a sample. Diffraction patterns are the result of the electron beam interacting with the crystal lattice structure which acts as a diffraction grating, the back scattered electrons create a diffraction pattern in the back focal plane, which then forms an image in the image plane. Diffraction patterns are presented in the form of regular dots/spots or concentric rings. Selected area electron diffraction (SAED) can be used by inserting the selected area aperture located in the image plane below the sample to define a particular area of interest. There are two imaging options when using the TEM, bright field (BF) imaging and dark field (DF) imaging (Figure 3.5).

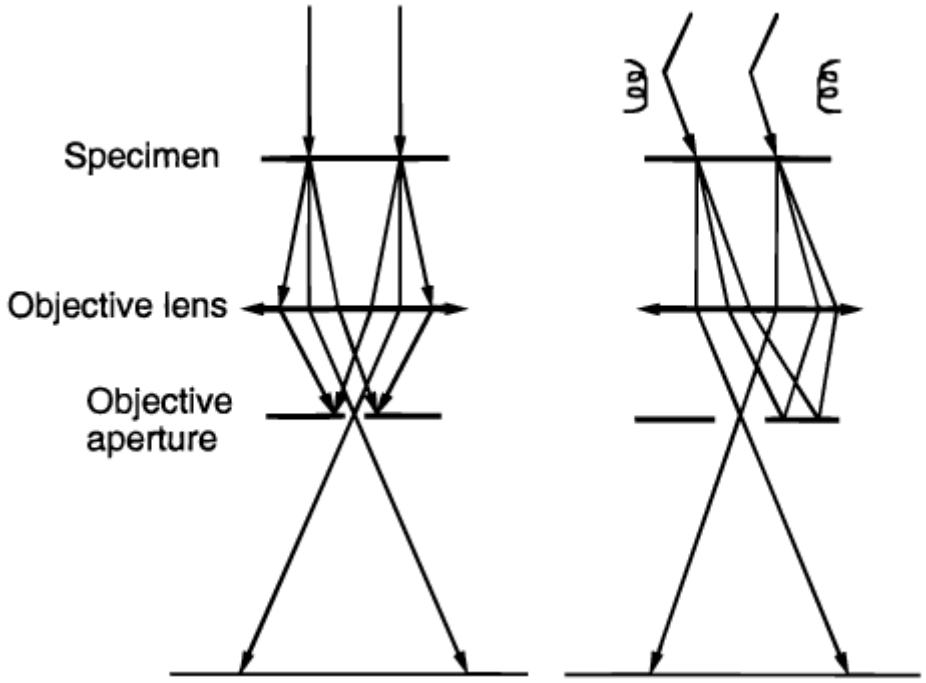

Figure 3.5 Optic ray diagram showing an overview of the bright field imaging mode (left) and dark field imaging mode (right).

Some areas of the sample scatter or absorb electrons and appear darker. Other areas transmit electrons and appear brighter. In bright field (BF) images the objective aperture is inserted to allow the unscattered beam to illuminate the sample while blocking the scattered electrons from interacting with the sample, this provides higher contrast in the image (Figure 3.5). In dark field (DF) images, the unscattered beam is blocked by the primary aperture allowing the scattered electrons to interact with the sample this can give particularly interesting information on particle size (Figure 3.5).

3.2. Raman Spectroscopy

Raman spectroscopy is a vibrational spectroscopic technique used to determine chemical composition and structural information of materials. It provides chemically specific information of materials such as molecular structure and composition and is a non-invasive, non-destructive technique that requires minimal sample preparation. Samples can be analysed in a variety of environments e.g. gas and liquid. Raman spectroscopy has gained significant traction in materials science including biominerals in recent years because of these reasons. Infrared spectroscopy (IR spectroscopy) is a technique analogous to Raman spectroscopy which has already been extensively used to analyse mineralised bone material [56]–[60] as well as teeth [61]. IR spectroscopy has some key advantages over Raman spectroscopy. When using

IR spectroscopy to study biological materials there are no problems with fluorescence (excitation and relaxation of electrons into and from continuum states) whereas with Raman spectroscopy, this can be a problem and in many cases IR spectroscopy offers therefore a better signal to noise ratio. However, there are several key limitations of IR spectroscopy, that are not existing for Raman spectroscopy, which makes Raman spectroscopy the method of choice for this project to analyse the molecular and crystalline makeup of the investigated samples. Raman spectra show a weak interaction with OH bonds whereas IR spectroscopy shows a significant interaction with water molecules due to strong absorption of the OH-bond in the infrared spectral region. Hence, unlike the standard IR spectroscopy, Raman spectroscopy allows the study of samples with high amounts of absorbed water or samples in aqueous environments. Further, Raman spectroscopy does not require samples to be extensively prepared since it is based on inelastic scattering.

In Raman spectroscopy, a monochromatic laser source is used to irradiate a sample, which interacts with molecular vibrational modes and phonons. Key for the application of Raman spectroscopy is the polarizability, i.e. the potential to induce charge fluctuations by an electromagnetic field, of the atoms and ions constituting the sample. Lattice and molecular vibrations trigger a distortion of the electron cloud that surrounds the molecule and a small fraction of the energy associated with the exciting laser photons is exchanged with the sample, causing the phenomenon known as Raman scattering (Figure 3.6) which is comparably weak, as only one in every 10^6-10^8 photons scatters [62]. There are in general three types of scattering events that can occur, elastic Rayleigh scattering, and the inelastic Stokes and anti-Stokes scattering (Figure. 3.6).

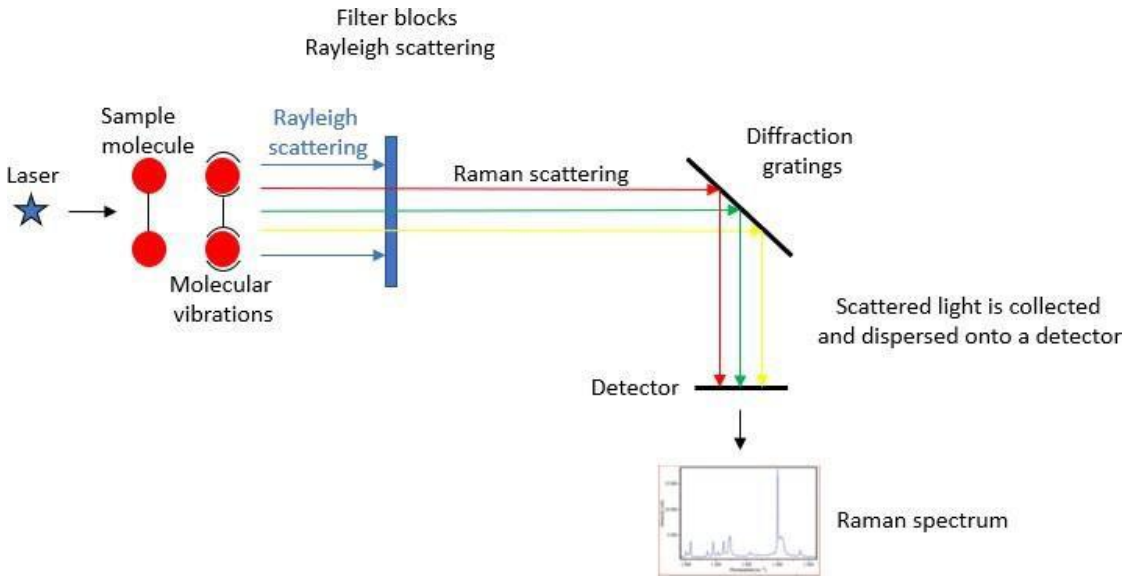

Figure 3.6 A schematic diagram of the experimental apparatus the Micro-Raman spectrometer. A laser irradiates a sample, which interacts with the molecular vibrations and phonons of a sample. The vibrations trigger a distortion of the electron cloud that surrounds the molecule and a small fraction of the energy produced by the laser photons is exchanged with the molecular vibrations, which causes Raman scattering to occur.

Rayleigh scattering (elastic scattering) occurs when a photon interacts with a molecule, distorting the electron cloud and causing it to enter into a higher energy state (virtual level). This is a momentary event (10^{-14} seconds) and rapidly returns to its ground state, emitting a photon of the same energy and wavelength as the incident photon, resulting in no loss of energy (Figure 3.7). **Stokes Raman scattering** also referred to as Stokes scattering is different in that it is caused by inelastic scattering, i.e. the energy of the exciting photon changes during this process. As the molecule moves from the ground state to a virtual state and then returns to a higher energy vibrational state the scattered photon has a lower energy than the incident photon resulting in a longer wavelength (Figure 3.7). **Anti-Stokes Raman scattering** occurs when a molecule already in an excited phonon state is excited to a higher virtual state, then goes back to its ground state emitting a photon with a higher energy than the incident photon, corresponding to a decrease of the wavelength (Figure 3.7). Light undergoing Rayleigh scattering, is the dominating process, and needs to be blocked by an edge filter allowing for the remaining scattered light to be collected and dispersed onto a CCD detector. Stokes scattering

has a greater intensity because initially there is a different number of molecules in each vibrational state. The population follows the Boltzmann distribution

$$N \propto \exp\left(-\frac{E}{k_B T}\right)$$

Eq. 1

The intensity of Stokes lines is proportional to the number of atoms in the ground state whereas the intensity of the anti Stokes lines is proportional to the number of atoms in the excited state. As the number of atoms in the ground state is more than the number of atoms in the excited states, the Stokes lines are more intense than the anti Stokes lines

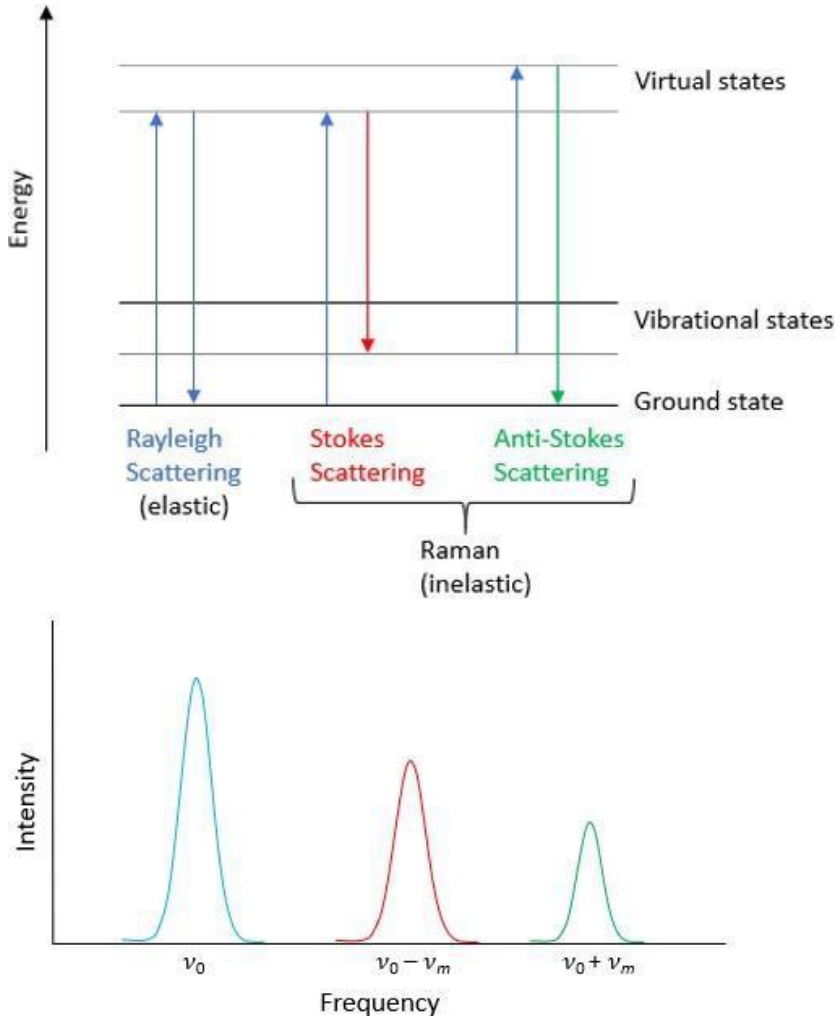

Figure 3.7 Jablonksi diagram of the energy transfer mechanisms between molecules and photons in Raman spectroscopy.

Raman scattering is therefore an inelastic process and Raman peaks (intensity maxima) at specific spectral positions given in wavenumbers (cm^{-1}) provide both quantitative and qualitative information regarding chemical composition, strain and crystallographic configurations.

3.1.2 Mechanism of Raman scattering

The theory behind both Raman spectroscopy and IR spectroscopy is centred around molecular vibrations. IR is based on absorption of photons with energies corresponding to the vibrational energy of molecules and Raman spectroscopy is based on the scattering of incident light at an energy shifted by the vibrational energy *hν* (*h* represents Planck's constant) of the molecule.

The difference behind the theory of each technique differs in that IR spectroscopy relies on molecular absorption at specific vibrational frequencies which causes a change in the dipole moment and Raman spectroscopy relies on the change in polarizability of a molecule.

In contrast to IR, where the photon/bond interaction depends on the polarity of the bond, Raman scattering requires a change in polarizability, $\boldsymbol{\alpha}$ during molecular vibration for vibrational excitation to occur in order to acquire a Raman spectrum. Hence, for a molecular bond to be Raman active, a change in its polarizability is required. The polarizability is a measure for how easily the electron cloud around a molecule can be distorted by the electric field component of the electromagnetic light wave $\vec{E}$, which interacts with the bond associated charges. The resulting electromagnetic field induces a dipole moment

$$\vec{P} = \boldsymbol{\alpha}\,\vec{E}$$

Eq. 2

The polarizability $\boldsymbol{\alpha}$ is a tensor and hence dependent on the direction

3.2.2 Raman shift

The Raman shift is expressed in wavenumbers.

$$\Delta\bar{\upsilon} = \frac{1}{\lambda_0} - \frac{1}{\lambda_1}$$

Eq. 3

Where $\Delta\bar{v}$ is the Raman shift λ_0 is the wavelength of the incident light and λ_1 the wavelength of the scattered light in cm.

The Raman shift is the energy difference between the incidence light and the inelastically scattered light. A shift in Raman peaks towards either higher or lower wavenumbers depends on the mass of the atom and the chemical bond lengths associated with them. Atoms with heavy masses and weak bonds have low Raman wavenumbers whereas atoms with light masses and strong bonds lead to higher Raman wavenumbers. This can be explained quantum mechanically by the dependence of the bond energy $\vec{E}_n$ on the frequency v as derived for the case of a simple harmonic oscillator (SHO)

$$\vec{E}_n = h\left(n + \frac{1}{2}\right) v$$

Eq. 4

where the index $n = 0,1,2,\ldots$ is an integer number assigning the different possible energy states. Since the frequency for a periodic oscillation

$$2\pi v = \sqrt{\frac{k}{m}}$$

Eq. 5

Eq. 5 becomes

$$\vec{E}_n = h\sqrt{\frac{k}{m}}\left(n + \frac{1}{2}\right)$$

Eq. 6+1

which shows, that for a given n and strong bond (large spring constant k) or low values for the atomic masses m the bond energy increases and vice versa.

3.3.2 Raman data collection

Raman Spectra were collected using a HORIBA Xplora PLUS Raman micro spectrometer. A spectral range from 600-3600 cm^{-1} was collected using the following settings, 532nm laser, long working distance (LWD) objective with x50 magnification, a diffraction grating of 1800T grooves/mm, the filter was set at 100%, hole 300µm, slit 100µm, 15 (seconds) acquisition

,10 (scans) accumulation.

3.4.2 Raman data analysis

The spectra were normalised with respect to the C-H stretching bond peak (2900^{cm-1}). The mineral to collagen ratio was derived by dividing the height of the phosphate peak by the average height of the C- H stretching bond peak. The data were analysed using a MATLAB programme written by Professor Roland Kröger (University of York).

3.5.2 Raman peaks in collagen Type 1

A Raman spectrum of collagen gives chemical information about collagen itself and bioapatite. The characteristic peaks in collagen can be seen in figure 3.8. The peak that is of particular interest for the purpose of this study and the time- resolved *in situ* experiments is the phosphate peak at 962 $^{cm-1}$. Other bands associated with the collagen are proline 851 $^{cm-1}$, hydroxyproline 873 $^{cm-1}$, $\nu_1 PO_4^{3-}$ 958 $^{cm-1}$, phenylalanine 1001 $^{cm-1}$, $\nu_1 CO_3^{2-}$ 1 070 $^{cm-1}$, Amide III 1246 $^{cm-1}$, CH_2 Deformation 1450 $^{cm-1}$ and Amide I 1656 $^{cm-1}$.

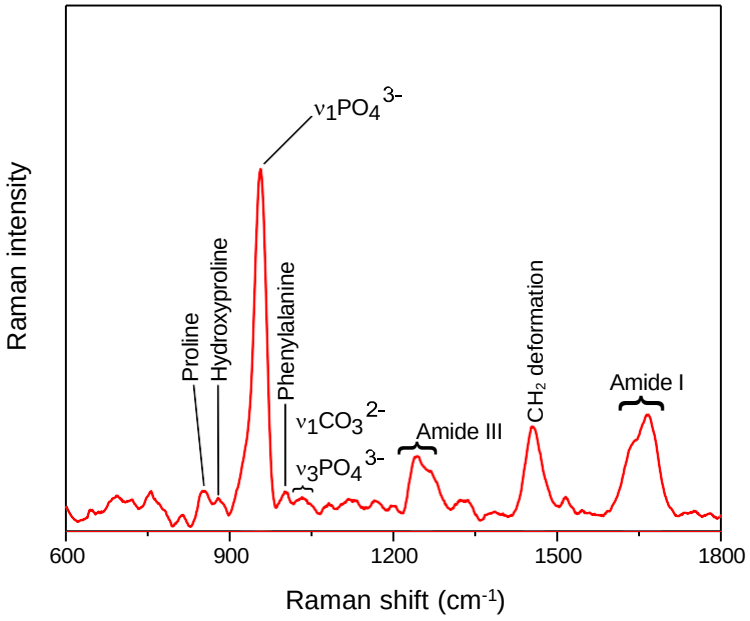

Figure 3.8 Raman spectrum of a mineralised collagen fibre extracted from a rat tail of a 12 week old Sprague Dawley® rat showing the characteristic peaks modes observed in bone and collagen Type 1.

It is widely acknowledged that prior to bone crystals fully mineralising into HAP their pre cursor phases exists firstly as ACP which transforms into OCP then to HAP [32]. This transformation process of bone mineral has successfully been observed using *in situ* Raman Spectroscopy. Raman spectra were taken of each of the pre cursor phases (ACP/OCP) ACP 936 – 942 cm^{-1}, synthetic OCP 955 cm^{-1} and the mineral phase HAP 962 cm^{-1} (Figure 3.9) to determine the characteristic peaks.

[63][63]

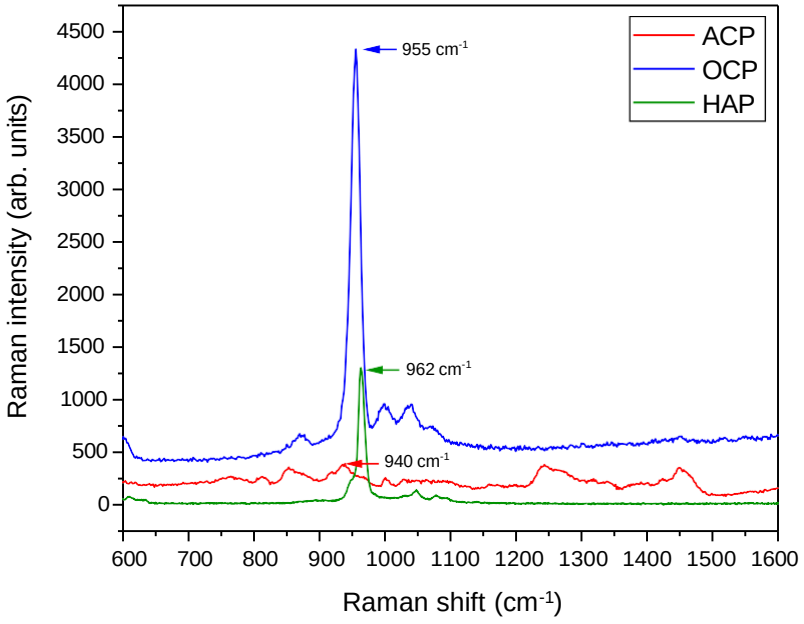

Figure 3.9 Raman spectra of synthetic ACP, OCP and synthetic hydroxyapatite. The characteristic peak of ACP is shown in red. The characteristic peak of OCP is shown in blue and the characteristic peak of HAP is shown in green. These peaks define the amorphous phases (red and blue lines) from the crystalline phase (green line).

Reference spectra were taken of the synthetic acidic polymers (Figure 3.9 and 3.10) that were used in the mineralisation experiments to provide an indication of the characteristic wavelengths that needed to be observed when analysing the Raman data.

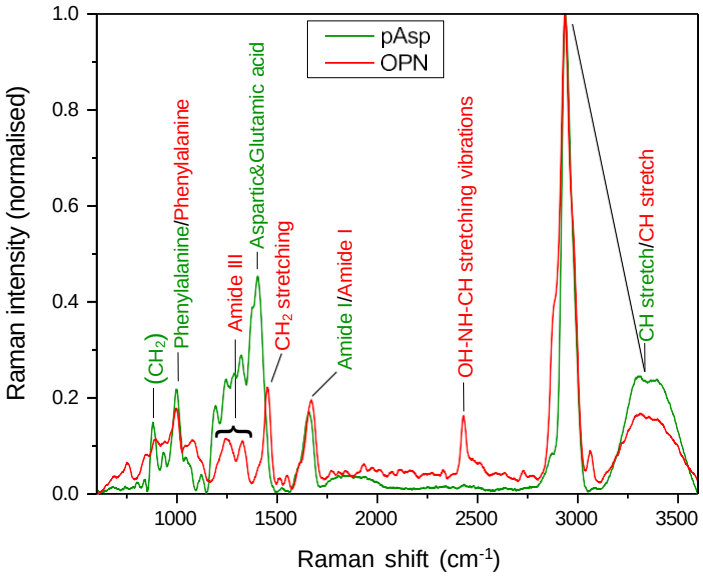

Figure 3.10 Raman spectra of the acidic polymers, osteopontin (OPN) and polyaspartic acid (pAsp) used in the mineralisation experiments. The red line denotes OPN and the green line denotes pAsp.

3.3. Synchrotron Techniques

All synchrotron experiments were conducted at Diamond Light Source, Didcot (UK). The *in-situ* SAXS/WAXS experiments were conducted on I22 beamline [64] and nXRF mapping, was conducted on I14 Hard X-ray nanoprobe beamline [65]. Synchrotron techniques have numerous advantages over conventional laboratory based microscopy and X-ray techniques. One of the most important advantages is the high brilliance of synchrotron light enabling time resolved in situ measurements and structural investigation of non crystalline biological materials. SAXS/WAXS experiments can be conducted in liquid under *in situ* conditions. These features including the advantages of synchrotron abilities were required conditions to study the crystallisation dynamics of the mineralisation process with nanometre spatial resolution *in situ* to quantify the transport and phase transition processes controlling the formation of hydroxyapatite/collagen composites. Using WAXS simultaneously, allowed for

the study and characterisation of the crystalline structure of the forming crystals. The *in situ* SAXS/WAXS experiments were conducted to complement the *in-situ* Raman work.

3.1.3 Synchrotron Light

The synchrotron accelerates electrons to close to the speed of light producing high intensity beams of light from infra-red to X-rays. The high intensity beams are channeled into each of the beamlines allowing scientists to use the synchrotron light to carry out experiments and gather extremely detailed information not possible elsewhere.

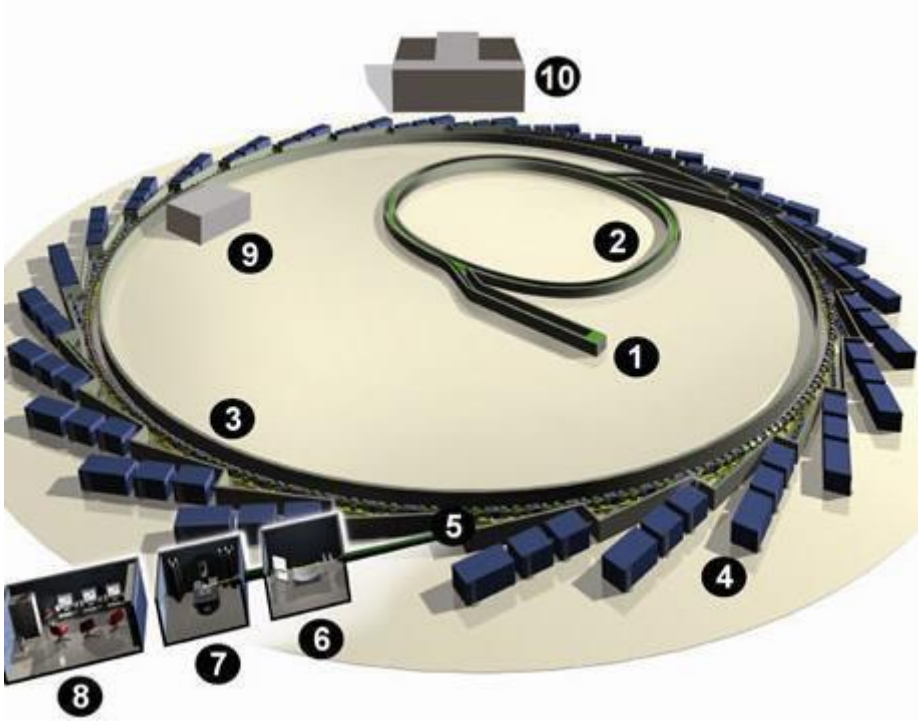

Figure 3.11 Layout of the synchrotron at Diamond Light Source, Oxford, UK. 1- Linear accelerator (LINAC) 2- Booster synchrotron 3- Storage ring 4- Beamlines 5- Front end 6- Optics hutch 7- Experimental hutch 8- Control cabin 9- Radio frequency system (RF) 10- Main control room (www.diamond.ac.uk/Home/Technology.html)

To produce a high intensity beam bunches of electrons are injected into the storage ring and circulated around the ring at near the speed of light. A series of magnets situated at points around the ring keep them circulating, and bend and control their trajectories. Bending magnets (dipole magnets) primary function is to bend the electrons round the storage ring. Electrons that are deflected when passing through the bending magnets emit a fan of X-rays. The synchrotron light from a bending magnet covers a broad spectrum, from microwaves to hard

X-rays. The beam is less collimated and brighter than the fine beam of X-rays from an insertion device. An undulator is made up of a complex array of small magnets that forces the electrons to follow an undulating trajectory. Undulators produce very bright light in a highly collimated beam. The peak energy generated (wavelength of the x-rays) by the undulator can be changed by altering the distance of the gap between the array of magnets. A wiggler consists of an array of magnets which forces the electrons to "wiggle". Wigglers produce a wide cone of light. Wigglers are used on beamlines where very high energy x-rays are needed. The high speed at which the electrons are travelling and the change in their trajectories forces the electrons to emit energy which is at X-ray wavelength.

Electrons are produced by an electron gun. The electrons that have escaped due to thermionic emission are accelerated by earthed (positive) anodes which produce a stream of electrons with an energy of 90kev. The series of chambers in which the electrons pass though have alternating electric fields so as the electrons pass through the chambers the electrons are always attracted to a positive field in front of them constantly making them accelerate. The linac (Figure 3.11) accelerates these electrons close to the speed of light (100 MeV) before they enter the booster synchrotron. Electrons are injected from the linac into the booster synchrotron (Figure 3.11). The booster is made up of two straight sections and a semi-circle attached to the top and bottom of these sections. Because electrons do not naturally follow a curved trajectory thirty-six bending magnets are positioned in the curved areas to manipulate the electrons around the curves. Once the electrons reach an energy of 3 GeV they are transferred into the storage ring. The storage ring is where the electron beam is stored for use by the beamlines. The storage ring (Figure 3.11) is made up of straight and curved sections and a series of bending magnets are used to curve the electron beam around the ring. Synchrotron light is emitted when the electrons travel round the storage ring. The storage ring is under vacuum to reduce the scattering of electrons with gas and air molecules. The very few gas molecules that are trapped in the vacuum collide with the electrons and cause them to lose energy, therefore, the storage ring is topped up with new electrons every 10 minutes to ensure an optimum beam. Because electrons loose energy and momentum as they produce synchrotron light the storage ring has a radio frequency system (RF system) (Figure 3.11) which provides the electrons with a boost of energy and momentum that they previously lost.

3.2.3 Wide angle X-ray scattering (WAXS) and X -ray diffraction

Wide angle X-ray scattering is a technique that measures the elastic scattering of monochromatic X-rays by a sample at wide angular ranges (5-60 °). WAXS provides information on the crystalline structure of materials as well as crystal size and orientation, which can be determined from 2D WAXS patterns. When X-rays hit a sample, they are scattered by the electrons in the material. Crystalline materials can be made up of regularly spaced atoms known as imaginary planes. The distance between the imaginary lines is referred to as the interplanar spacing or the d spacing. Crystals can diffract X-rays because the interplanar spacing in a crystal lattice is of the same order as that of the wavelength of the X-rays. When the reflected beams are in phase and interfere constructively this is known as Bragg diffraction (Figure 3.12) as described by

$$n\lambda = 2dsin\theta$$

Eq. 7

where λ is the wavelength of the radiation used, d is the inter-planar spacing involved and θ is the angle between the incident (or diffracted) ray and the relevant crystal planes; n is an integer, referred to as the order of diffraction.

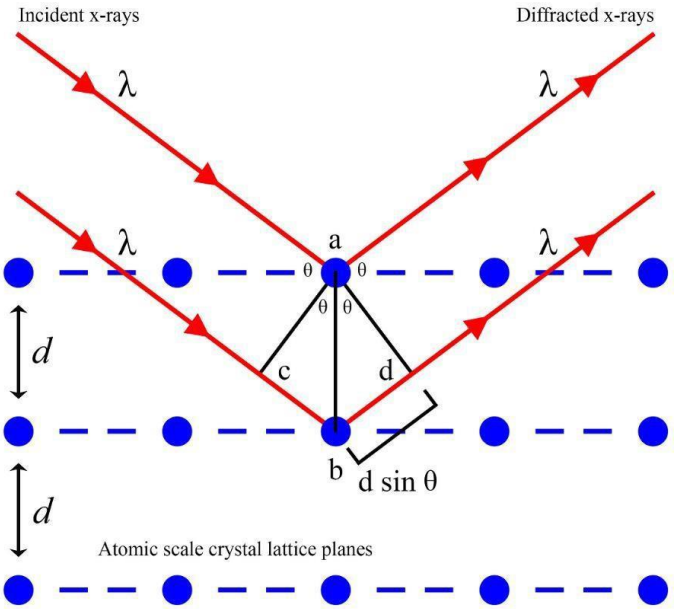

Figure 3.12 Bragg diffraction showing constructive interference occurring. Constructive interference can only occur if the incident and scattered X-rays travel an equal distance. The incident X-rays interact with the atoms in the crystal lattice at angle θ and reflect at certain angles. Two incident waves are diffracted by two crystal lattice planes: ab = d, sin θ = cb/ab/bd so cb/bd = d sin θ.

3.3.3 Small angle X-ray scattering (SAXS)

SAXS is an analytical technique that measures the elastic scattering of monochromatic X-rays by a sample. Measurements are made at small scattering angles ($0.1° - 5°$). The decrease in the scattering angle allows for the observation of larger features in a sample. SAXS provides information on structural characterisation of nanomaterials, in the range of 1-100 nm. SAXS scattering is a versatile technique as samples require little or no sample preparation, samples can be amorphous, crystalline or semi-crystalline, and can be studied *in-situ* with fluid flow at varying temperatures. SAXS patterns give information on morphology, size and volume of

particles and macromolecules such as proteins and polymers. SAXS patterns are plotted as intensity against the scattering vector q

$$q = \frac{4\pi}{\lambda}\sin\theta$$

Eq. 8

$$q = \frac{2\pi}{d}$$

Eq. 9

where λ is the wavelength and 2θ is the scattering angle and d is the characteristic spacing within the sample.

In a SAXS pattern, two regions can be studied, the Guinier region and the Porod region to give characteristic information on the material under investigation [66]–[68] (Figure 3.13).

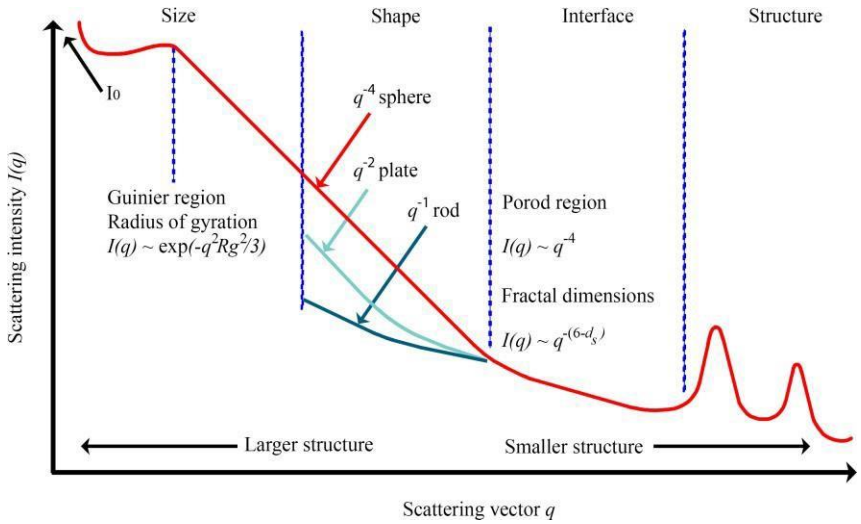

Figure 3.13 Typical 1D SAXS plot showing the characteristic parameters that can be obtained from the scattering pattern of the investigated sample.

The Guinier region which lies in the lower q range provides information on particle size and growth. In the Guinier regime the measured intensity follows the relationship

$$(q) = I_0 \exp\left[-\frac{q^2 R_g{}^2}{3}\right]$$

Eq. 10

Where I_0 is the intensity at θ and R_g is the radius of gyration

The radius of gyration is related to the size of the particle. For a sphere the radius R is related to R_g by

$$R^2 = \frac{3}{5} R^2$$

Eq. 11

R_g can be calculated from the gradient of the plot of

$$(q) = I_0 \exp\left[-\frac{q^2 R_g{}^2}{3}\right] \ln(q) = lnI_0 - \frac{1}{3} q^2 R_g{}^2$$

Eq. 12

The equation above relates to the Rg of a sphere however, equation for the Rg of other shaped particles are shown in Glatter and Kratky [67].

The Porod region which lies in the higher q range provides information on the shape and morphology [68]. For the Porod regime the $I(q)$ relates to the morphology and shape of the particle

$$I(q)\alpha q^{-p}$$

Eq. 13

where p is the Porod slope which can be determined from the slope of a log lnI(q) vs ln(q) plot. For example a slope of ⁻4 indicates a smooth sphere whereas a slope of ⁻2 denotes plates/lamellar and a slope of ⁻1 is a signature of rods (Figure 3.13).

3.4. Experimental Design and Setup

The *in situ* experiments were conducted on the small and wide angle X-ray scattering (SAXS and WAXS) beamlime I22 at Diamond Light Source (Oxford, UK). The heating cell used to perform the time resolved *in-situ* Raman experiments was also used for the SAXS/WAXS experiments. A single collagen fibre was placed into the sample holder and sealed using vacuum grease and a glass cover slip. An inlet and outlet tube were connected to the sample holder allowing for the PILP solution to be continuously pumped through the sample holder, via a syringe pump, immersing the collagen fibre in the PILP solution for the duration of the experiment. (Figure 3.14). Once the sample holder was sealed and the collagen fibre was immersed in the PILP solution and the heating cell was placed into position on the beamline. The PILP solution was then pumped through at a rate of 5 ml per hour and the temperature of the heating cell was set to 37°C. SAXS and WAXS data were collected simultaneously.

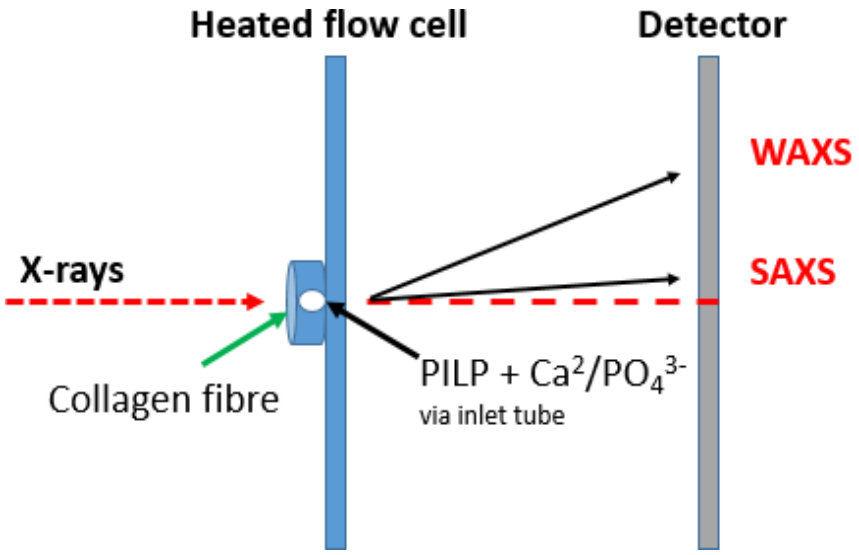

Figure 3.14 Schematic of the in situ set up on I22 beamline.

3.5. Data Collection and Analysis

SAXS data was collected as a function of time using a Pilatus P3-2M (2D detector). A camera distance of 9.806m and energy of 12.4keV, with beamstop in the centre of the detector, was employed to give access to the spacing, suitable for observation of the collagen gap spacing, (67nm). A beam size of v = 16µm x h = 21µm was chosen. The WAXS data was collected simultaneously using the Pilatus 3-2 M-DLS-L at a distance of 225.6mm, which at 12.4 keV is suitable for collecting the major hydroxyapatite diffraction peaks q = 1.82 A^{-1} (002) and q = 2.23 A^{-1} (combination of (211), (112) and (300)). All data was collected as a spatially resolved map with the micro focus beam at 15 minute intervals, all subsequent SAXS and WAXS data were summed over all pixels in the map to give an average SAXS and WAX pattern at each time point. This was to improve the statistics and reduce the beam damage.

An optical image was taken using an on axis sample camera to check the position of the collagen fibre in the *in situ* cell (Figure 3.15) whilst in position on the beamline. This is important for aligning the maps to the correct region of the sample.

Figure 3.15 An image showing the positon of the collagen fibre in the in situ cell during the time resolved in situ experiment on I22 beamline.

The corresponding images in figure 3.16 are collected from this fibre. The scatter from the multiple d spacing of the collagen fibre can be observed as incomplete rings aligned to the collagen fibre axis (Figure 3.16 a, b, c, d). The scatter from the growing crystals can be seen to increase in a diffuse band perpendicular to the fibre axis (Figure 3.16 a and b).

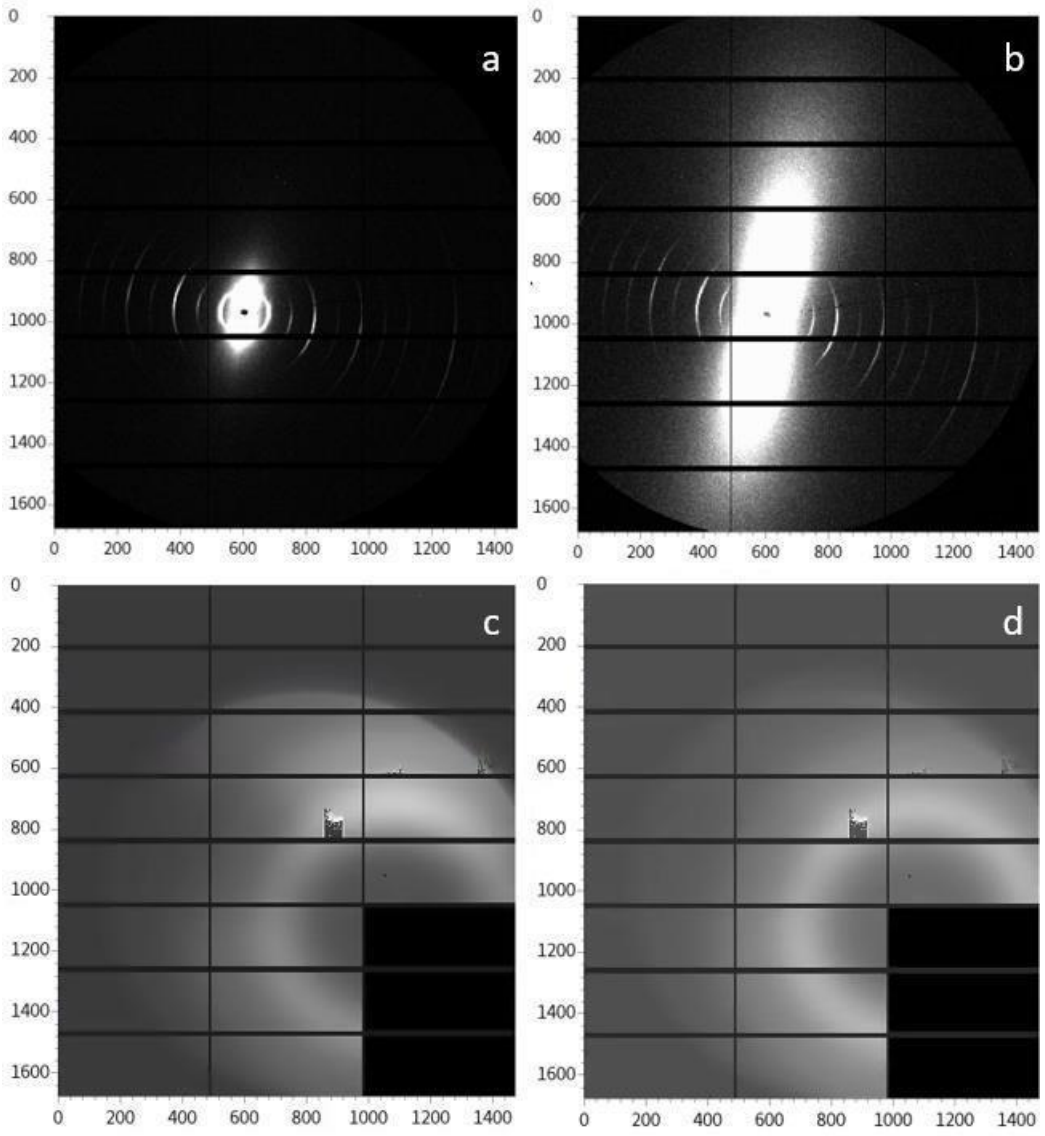

Figure 3.16 a) 2D SAXS data at the beginning of the experiment. The collagen d banding can be observed as the curved lines. b) 2D SAXS data at the end of the experiment. The collagen d banding can still be clearly observed at the end of the experiment. The elongated shape represents the scattering from the crystals due to mineralisation c) 2D WAXS data at the beginning of the experiment d) 2D WAXS at the end of the experiment. The axis are in pixels – where 1 pixel on the Pilatus detector is 172um x 172 um.

The SAXS and WAXS data was processed using a software package The *Data Analysis Workbench* (DAWN) developed at the Diamond Light Source (DLS) [69].

The 2D SAXS detector data/images were sectioned into 8 wedges (Figure 3.17). The wedges were positioned so that data could be collected independently from along the collagen fibre axis (0 and 4) and off the collagen fibre axis (2 and 6). The data collected in wedges 1, 5, 3 and 7 were disregarded as the data was a mix of the different axis therefore it was not useable.

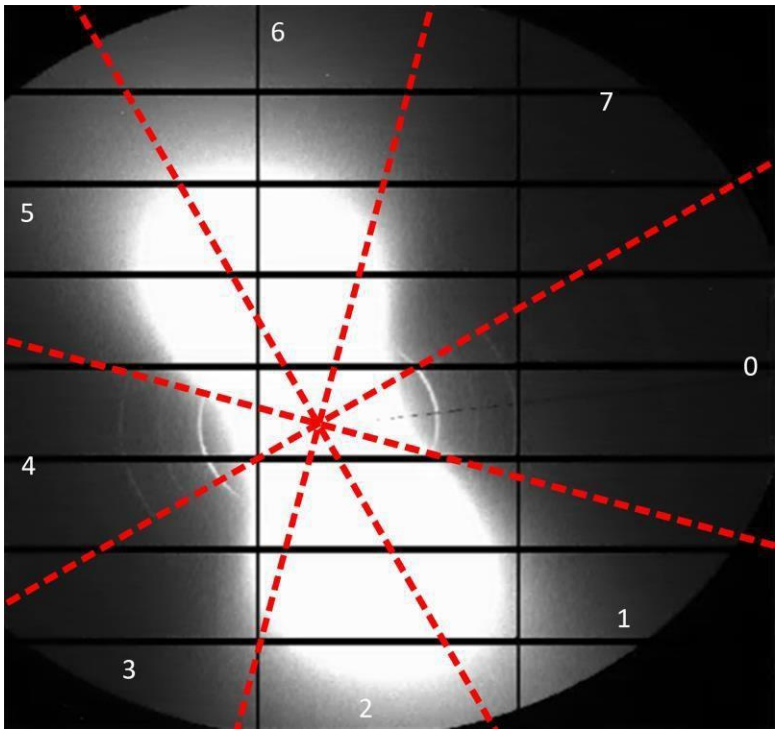

Figure 3.17 Schematic showing the 2D detector data sectioned into 8 wedges. Wedges 0 and 4 contains data from the collagen fibre axis. Wedges 2 and 6 contains data from off the collagen axis. Wedges 1,3,5,7 contains a mix data of from data from both axis.

The raw data were collected as maps using the micro beam. All frames that form a map were summed together to give a single 2D pattern per time point for both the WAXS and SAXS data. A background subtraction was added to the both the SAXS and WAXS pipeline because the sample has a large liquid background.

Several different combinations of background signal were collected to observe the effect on the WAXS pattern (Figure 3.18). Background subtraction from the Cell+PILP was used as this would only the leave the signal from the collagen and any forming mineral in the final dataset. For the SAXS plots, observations were made for subtle changes in the slope. If changes in the slope are coming from differences in the background then these differences need to be subtracted for SAXS. (Figure 3.18). Again, the background subtraction from the Cell+PILP was used as this would only the give the signal from the collagen and any forming mineral in the final dataset.

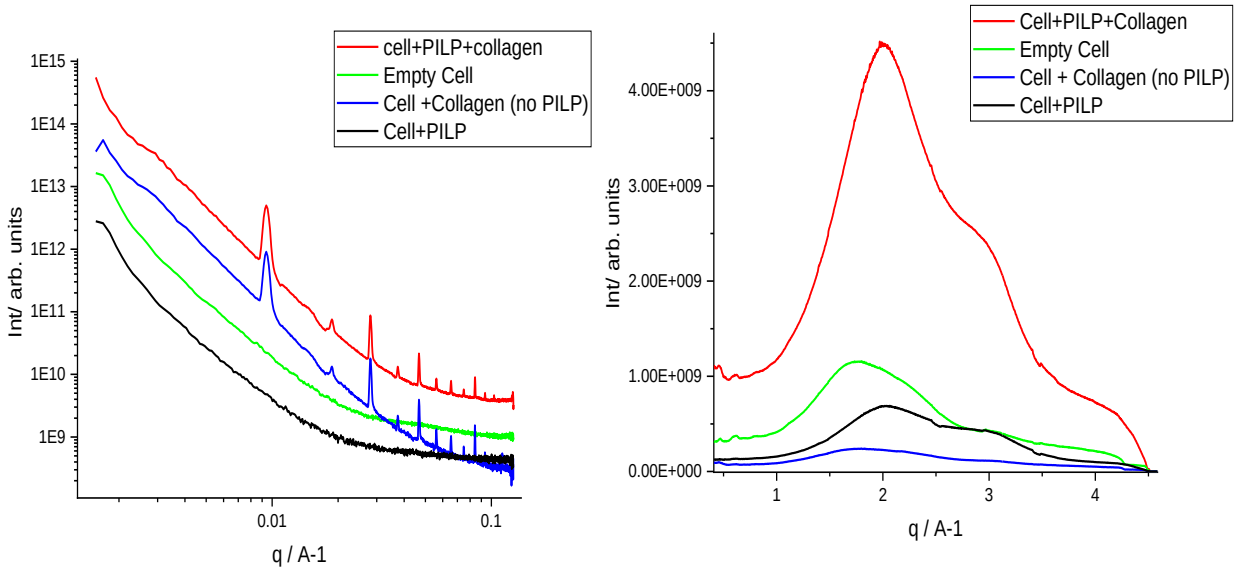

Figure 3.18 a) background signals using various combinations of cell, PILP and collagen collected from the WAXS detector b) background signals from various combinations of cell, PILP and collagen collected from the SAXS detector.

A mask was added to the SAXS and WAXS pipeline. Adding a custom mask masks the detector grid and masks any dead pixels (Figure 3.19) so they will not be considered in the correction and results [70].

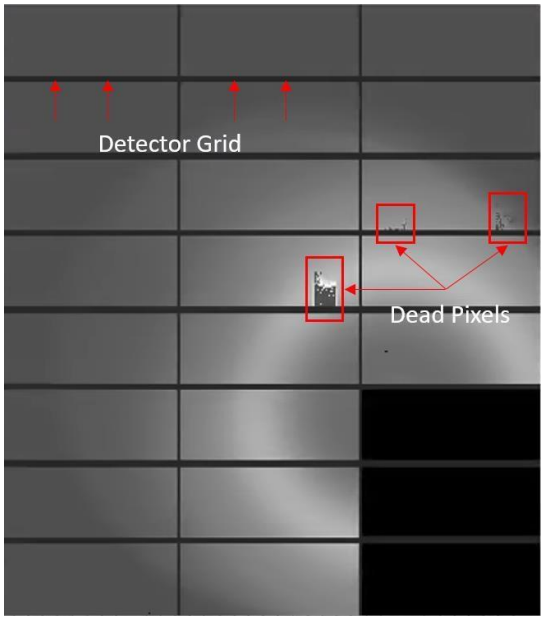

Figure 3.19 Image of the 2D data collected before a mask was added. The detector grid and the dead

pixels can be seen in the image.

To transform the 2D images collected by the SAXS and WAXS detector to 1D plots an azimuthal integration function was integrated in to the pipeline. The peaks in figure 3.21 correspond to the collagen periodicity (d banding). The allows measurements to be taken of changes in order of the d banding as a function of time. Azimuthal integration converts the detector images as a function of *azimuthal angle* vs *q* rather than *x* and *y* pixel values [69] (Figure 3.20 a and b and Figure 3.21 a, b, c,d and e).

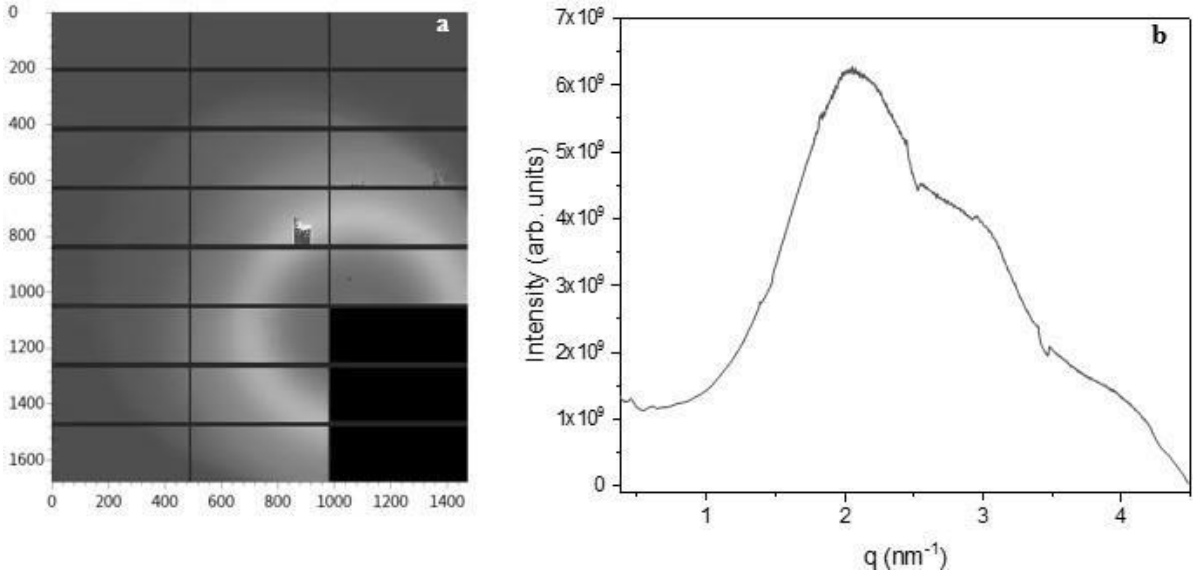

Figure 3.20 2D image collected by the WAXS detector b) 1D plot after applying the azimuthal integration function to the data processing pipeline.

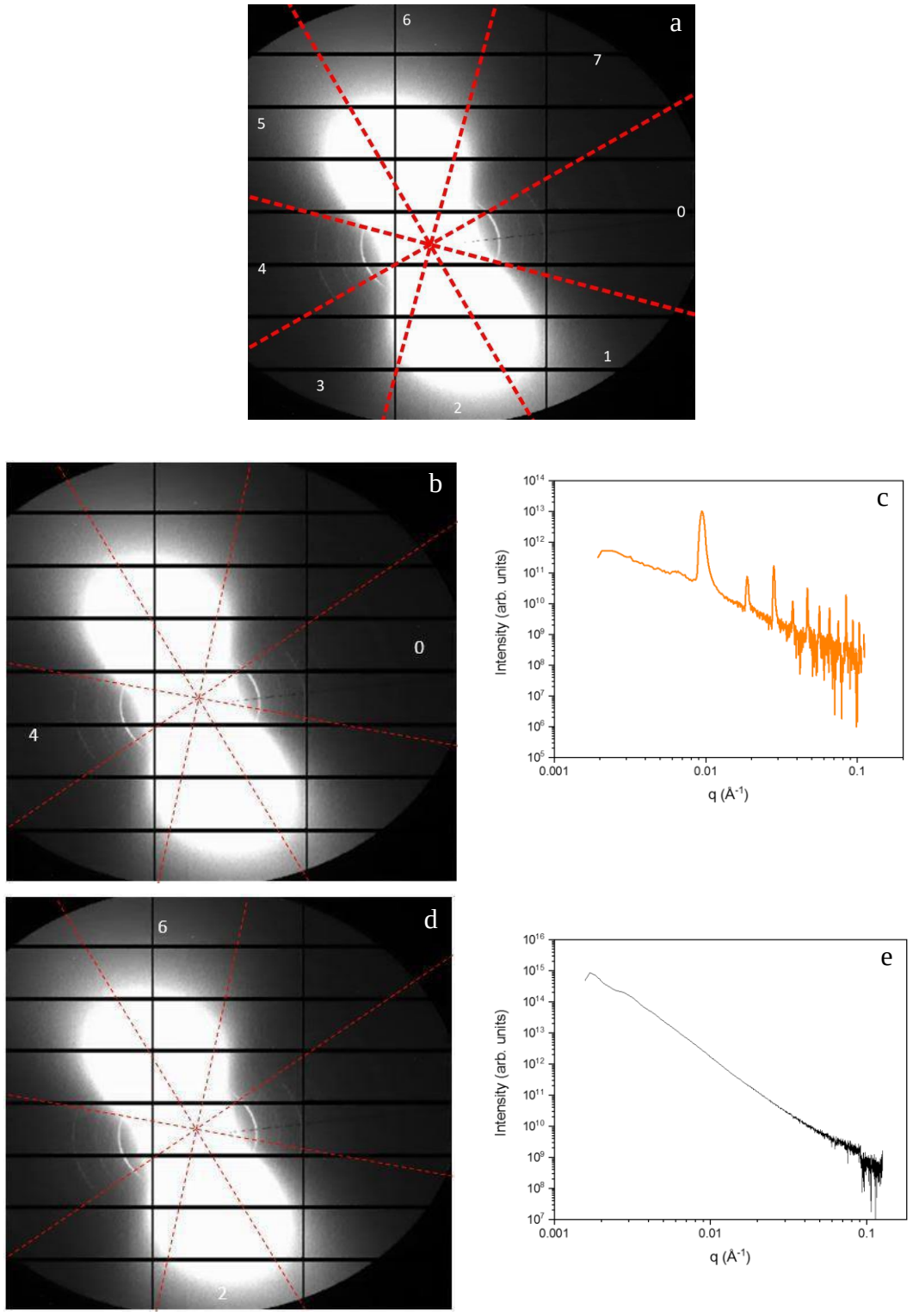

Figure 3.21 a) 2D image collected by the SAXS detector. b) Data from on the collagen axis in wedges 0 and 4. c) 1D plot of summed data from on the collagen axis in wedges 0 and 4 after applying the azimuthal integration function to the data processing pipeline. d) 2D image collected by the SAXS detector. Data from off the collagen axis in wedges 6 and 2. e) 1D plot of summed data from off the collagen axis in wedges 2 and 6 after applying the azimuthal integration function to the data processing pipeline.

3.6. nano- X- ray Fluorescence (n-XRF)

n-XRF experiments were performed on the Hard X-ray Nanoprobe beamline, I14 at Diamond Light Source, Oxford, UK [65]. This beamline is a facility for nanoscale microscopy providing special mapping of elemental composition by X-ray fluorescence (XRF), structural phase by nano-X-ray diffraction (n- XRD), speciation by X-ray absorption near-edge spectroscopy (XANES) and phase or electron density through differential phase contrast (DPC) and ptychography. The beamline is 185 meters long and has an energy range of 5keV to 23keV providing a beam size of 50nm [65].

The XRF detector provides the chemistry of a sample by measuring the fluorescent x- ray emitted from a sample when it is excited by a primary x- ray source (Figure 3.22). Each of the elements present in a sample produces a set of characteristic fluorescent x- rays (fingerprint) that is unique for that specific element. In n-XRF mapping a focused spot is used to irradiate a small area of the sample to determine the elemental composition of the area of interest. The sample is then moved in a grid pattern to create a 2D image of the chemical composition of the sample. A sample is irradiated with high energy x-rays. When an atom is struck in a sample with an x- ray of sufficient energy (greater than the atoms K or L shell binding energy) an electron from one of the atoms inner orbital is dislodged. The atom regains stability, filling the vacancy left in the inner orbital shell with an electron from one of the atoms higher energy orbital shell. The electron drops to a lower energy state by releasing a fluorescent x-ray. The energy of the x-ray is equal to the specific different in energy between the two quantum states of the electron. The measure of this energy is the basis of XRF analysis. Most atoms have several electron orbitals (e.g., shell K, L, M). When X-ray energy causes electrons to transfer in and out of these shell levels, XRF peaks with varying intensities are created. The peak energy identifies the element, and the peak height/intensity is indicative of its concentration.

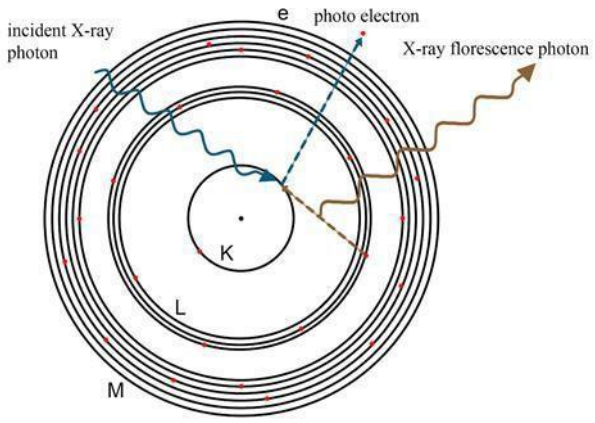

Figure 3.22 A diagram of the XRF process.

3.7. Materials and sample preparation

Collagen fibres were mineralised *ex situ* for 7 days at 37°C using OPN and pAsp PILP solution (27000kDa). The mineralised fibres were then washed, freeze dried, resin embedded and 500nm thick microtome sections were prepared and mounted on TEM grids (as discussed in Chapter 2)

3.8. Data Collection and analysis

The mineralised collagen fibre was placed into the beamline sample holder and the sample holder mounted onto the beamline. n-XRF measurements were performed on mineralised collagen fibres. Nano XRF maps were collected using I14 beamline using 8keV X-rays. Samples were raster scanned through a 50nm focussed beam and fluorescence spectra collected using a 4-channel SDD (Rayspec). The Ca-Ka and P-Ka maps were extracted by fitting the fluorescence spectra using PyMCA [71].

A set of coarse maps were obtained from each image with details of the distribution of the different elements in the region of interest. In this case, the fluorescence signal from Ca-Ka and P-Ka was of interest. Initially, measurements were taken of larger areas. In the case of the n-XRF maps, measurements were taken from an area measuring 200nm x 200nm. Using a coarse step size of 1μm allows for low resolution maps of a large area to be created in a short space of time (Figure 3.23a). Regions of interest can then be focused upon and subjected to a fine scan producing a higher resolution map (Figure 3.23b).

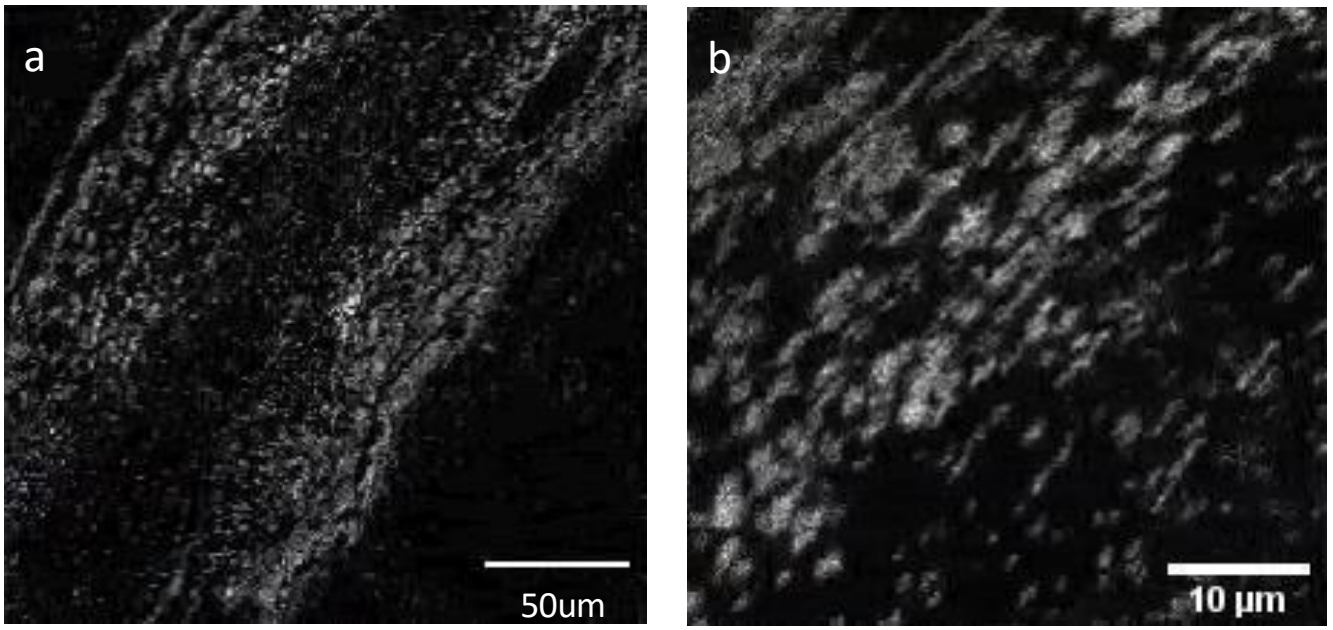

Figure 3.23 A coarse map of the mineralised collagen fibre b) a fine scan of the mineralised collagen fibre.

Chapter 4 **Characterisation of Bone Mineral using Electron Microscopy**

After several decades of research focusing on the characterisation of bone mineral there continues to be active debates on the bone mineral structure particularly regarding the mineral morphology, hierarchical organisation and the presence of an amorphous phase [25], [72]–[77]. Electron microscopy was used to characterise the bone mineral phases in the *in-situ* mineralised collagen fibres. The aim of these studies was to assess the extent of mineralisation of the *in-situ* mineralised collagen fibres, and to determine whether the mineral phase shows likeness to the mineral organisation observed in native bone. To differentiate between and amorphous phase and a crystalline phase and overall to provide a deeper insight into the structural morphology and organisation of the bone mineral.

4.1. Results

Collagen fibres were mineralised *in situ* for varying periods of time, (4 hours, 9 hours and 7 days) using OPN as the directing agent. Poly-aspartic acid (pAsp) and fetuin-A were also used to mineralise collagen fibres and to observe the impact of different directing agents on the crystal nucleation and growth.

The bright field TEM (BFTEM) images show longitudinally cut microtome sections of collagen fibres. The edge of the fibre is visible, whilst revealing the interior of the collagen fibre showing that both intrafibrillar and extrafibrillar mineralistion of the collagen fibres has been achieved (Figure 4.1). The crystals appear to be aligned with their c-axes roughly parallel to the longitudinal axis of the fibrils (Figure 4.1 a,c and e) mimicking a mineral organisation pattern similar to that observed in bone [14].

The d-banding of approx. 67 nm periodicity can be observed in the fibres mineralised for 4 hours and 9 hours which matches that of native collagen, whereas it cannot be identified for the 7 days deposition time, which is likely due to the much higher crystal density dominating the contrast in the latter case. It is noteworthy, that for 4 hours deposition time large unmineralised collagen regions can be seen in comparison to the 9 hour sample, which could be due to an inhomogeneous progression of nucleation and crystal growth at the early stage of mineralisation. The corresponding diffraction patterns shown in Figure 4.1 (b, d and f) reveal

the presence of hydroxyapatite in all cases. The red circles in these figures show the regions of interest selected for SAED. The 002 and the 004 reflection arcs can be observed in the diffraction patterns indicating that the [001] c-axis of the HAP crystals are aligned with the collagen fibril axis within an angular range of approx. ±20˚ (Figure 4.1 b,d and f).

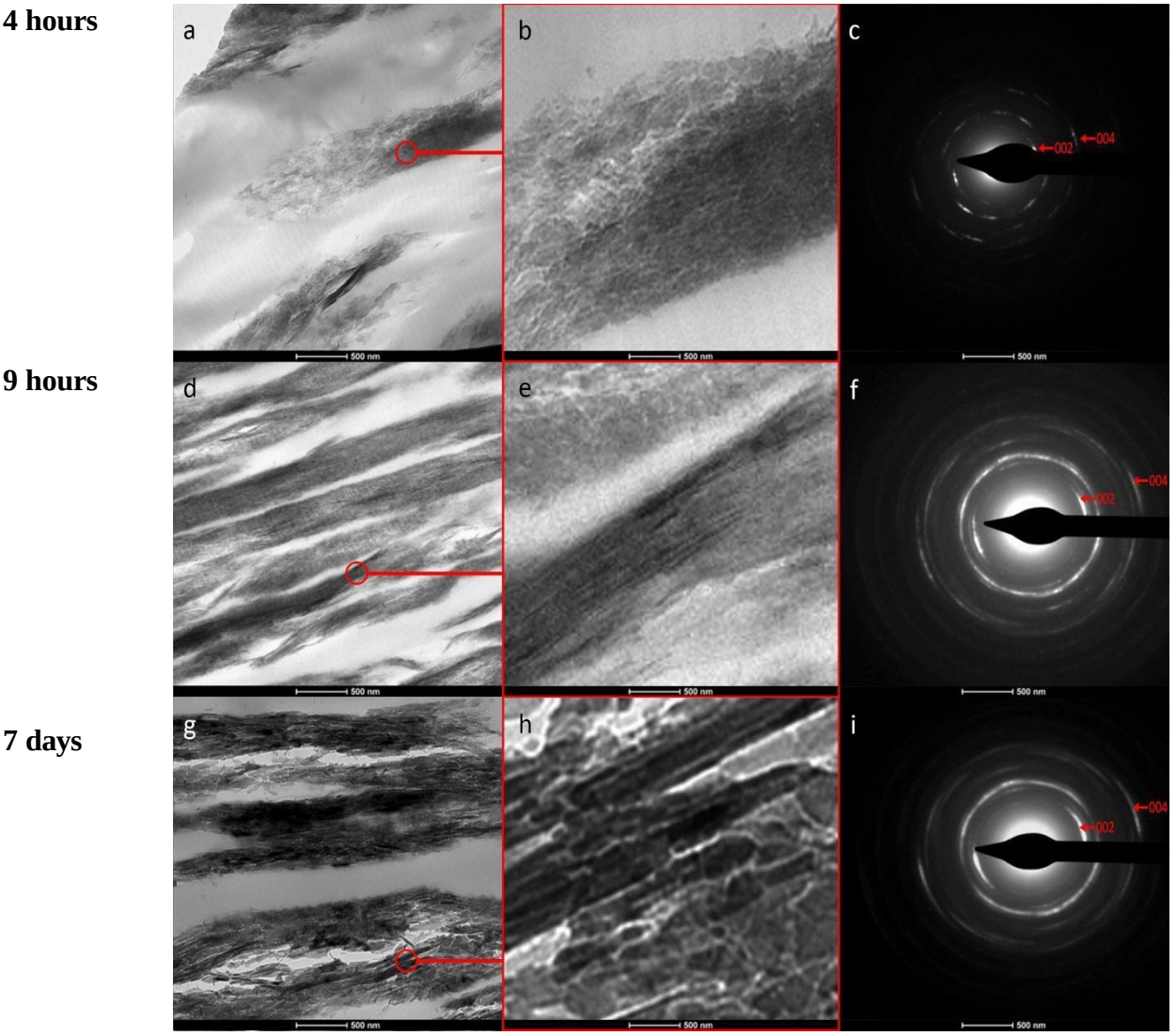

Figure 4.1 a, d and g) BFTEM images of mineralised collagen fibres at 4 hours 9 hours and 7 days, respectively. b, e and h) SAED patterns of the region indicated by red circles in (a, d and g). c, f and i) The 002 and the 004 reflection arcs can be observed in the diffraction patterns indicating that the [001] c-axis of the HAP crystals are roughly aligned with the collagen fibril axis with an angular distribution of ± 20˚.

Besides the acicular crystals, we observe in all samples the presence of plate-shaped nano-crystals with very different spatial extensions. We find for the acicular crystals typical diameter values of 5-10 nm and c-axis extensions of several hundred nm, whereas the plate-shaped crystals dimensions of approx. 30-50 nm (figure 4.6). These two distinct morphologies give rise to the question whether they represent different phosphate phases, in HAP and OCP. This

question was addressed by comparing the diffraction patterns of regions containing dominantly one of the two morphologies. In order to identify the possible presence of OCP synthetic OCP was synthesised.

Observations from the TEM images show that it is particularly difficult to differentiate between OCP and HAP by just looking at the images of the crystals (Figures 4.2 and 4.3). However, the diffuse ring in the diffraction pattern of the OCP is indicative of an amorphous phase (Figure 4.2b) whereas the diffraction patterns of the mineralised collagen fibres are spot patterns (Figure 4.1 b,d,f), which is indicative of a crystalline phase, in this case HAP. The *in situ* Raman experiments further indicate that the mineral phase is HAP.

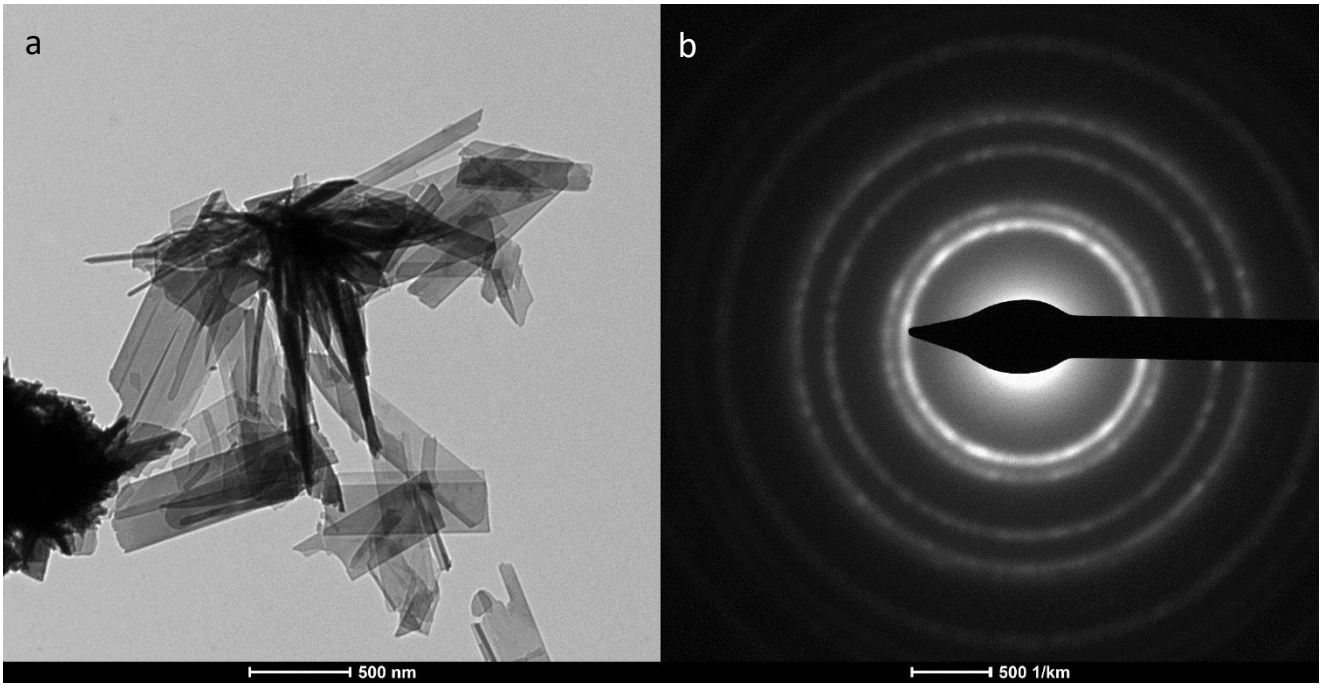

Figure 4.2 a) BFTEM image of OCP b) Diffraction pattern of OCP crystals.

It appears from the TEM images that there are two morphologies of crystals, platelets and acicular crystals (Figure 4.2). It could be questioned, do the platelets represent the amorphous phase and do platelets grow into acicular crystals as the transformation phase takes place? However, the images seem to suggest that both co-exist (Figure 4.1 and 4.3).

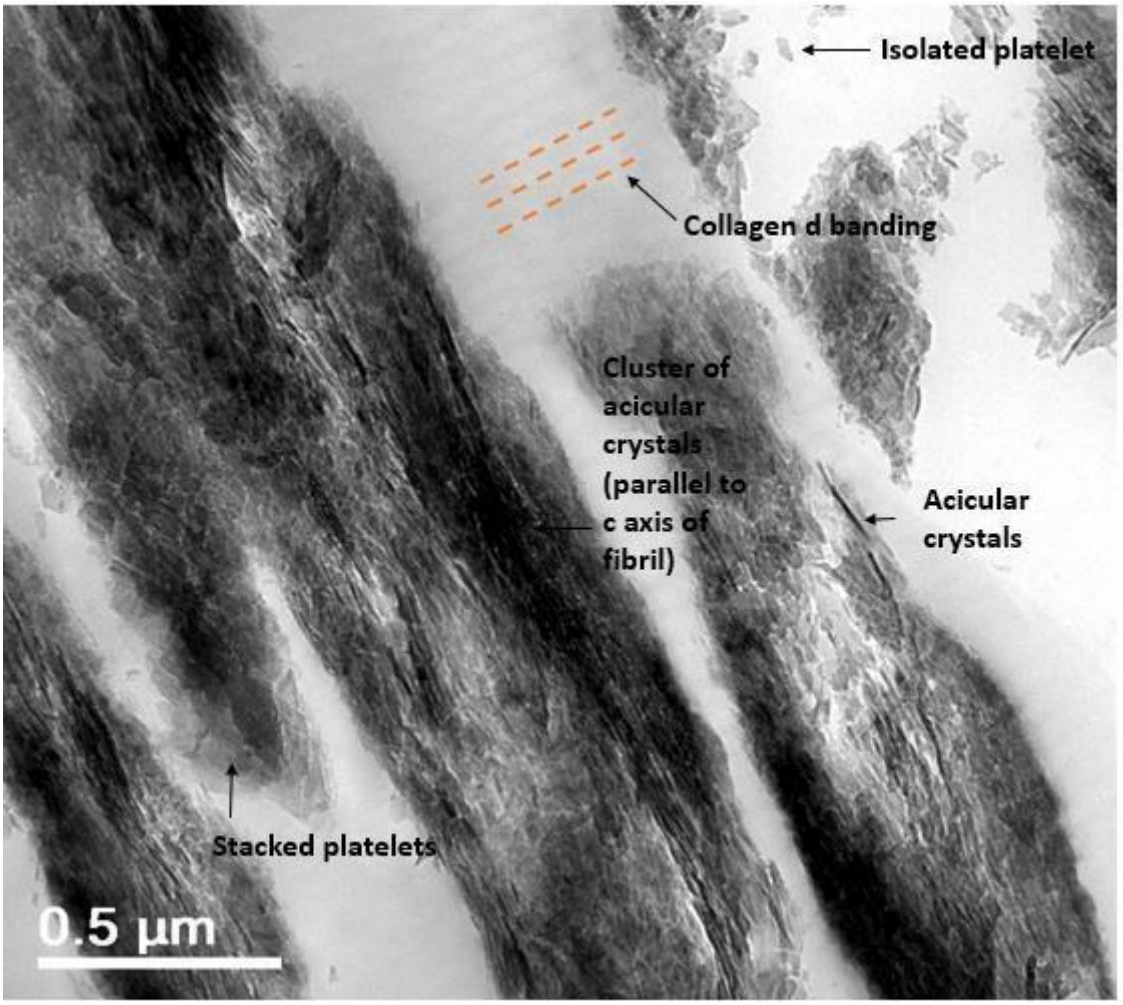

Figure 4.3 BFTEM image of collagen fibre mineralised for 9 hours showing two crystal morphologies in the form of platelets and acicular crystals.

The platelets have a broad range of size, in the region of 10 – 100 nm or more (Figure 4.3). The needles have a dense, dark appearance and strong scattering. The needles are long and thin with strong axial anisotropy. The needles are ~ 100's nm long in length and 5-8 nm in width that corresponds to the literature (Figure 4.3) [2].

To further attempt to distinguish between an amorphous phase (OCP) and a crystalline phase (HAP) in the mineralised collagen fibres SAED patterns were taken of isolated platelets and needles (Figure 4.4). Both of the diffraction patterns of the cluster of platelets and needles show

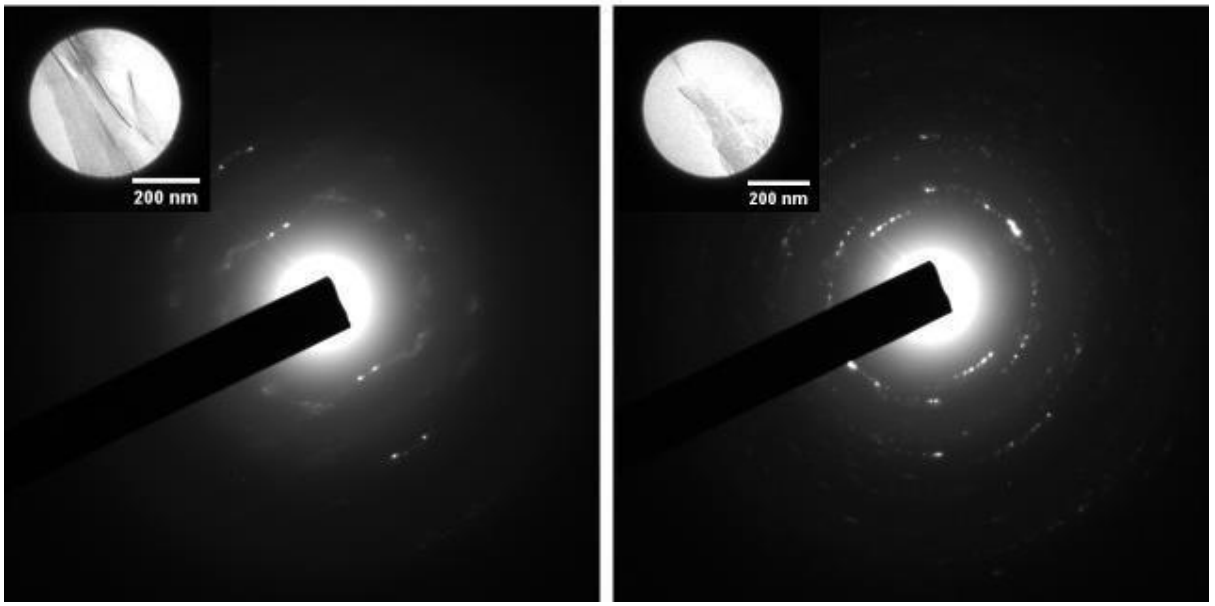

Figure 4.4 Regions of interest selected using SAED and the corresponding diffraction patterns. Left: diffraction pattern of an acicular crystal cluster Right: Diffraction pattern of a platelet cluster.

spot pattern indicative of a crystalline material (Figure 4.4). The diffraction pattern of the platelets from the collagen fibre mineralised for 4 hours, which is the time point just after infiltration, and the very early stages of the mineralisation process also shows a spot pattern indicative of a crystalline material. It would therefore be interesting to follow on from this work and look at a sequence collagen fibre from earlier time points from 1-3 hours to attempt to distinguish an amorphous phase.

A more detailed quantitative analysis of the crystal morphologies and their size distribution for the OPN induced precipitation was undertaken to extract information on their dependence on time. Clear differences can be found for the two different identified crystal morphologies apart from their diffraction patterns, which show that the acicular crystals and platelets have different crystallographic characters. This approach helps to quantify the relationship between morphology evolution and time whereas other studies [76], [78], [79] usually only consider the overall crystal sizes and not anisotropic behaviour which could be indicative for the presence of different mineral phases.

A total of 30 acicular crystals and platelets at 3 different time points (4 hours, 9 hours and 168

hours) were evaluated using the measurement tool in the ImageJ software. These time points were chosen since they correspond to the time points in the *in situ* experiments showing significant changes. The length (in long axis direction) and diameter (perpendicular to the long axis) of the acicular crystals the area, as well as the diameter of the platelets were measured manually. Error bars were calculated using the standard deviation. This was calculated by dividing the standard deviation by the square root of the number of measurements that make up the mean. The results are shown in Table 1 together with the standard deviation.

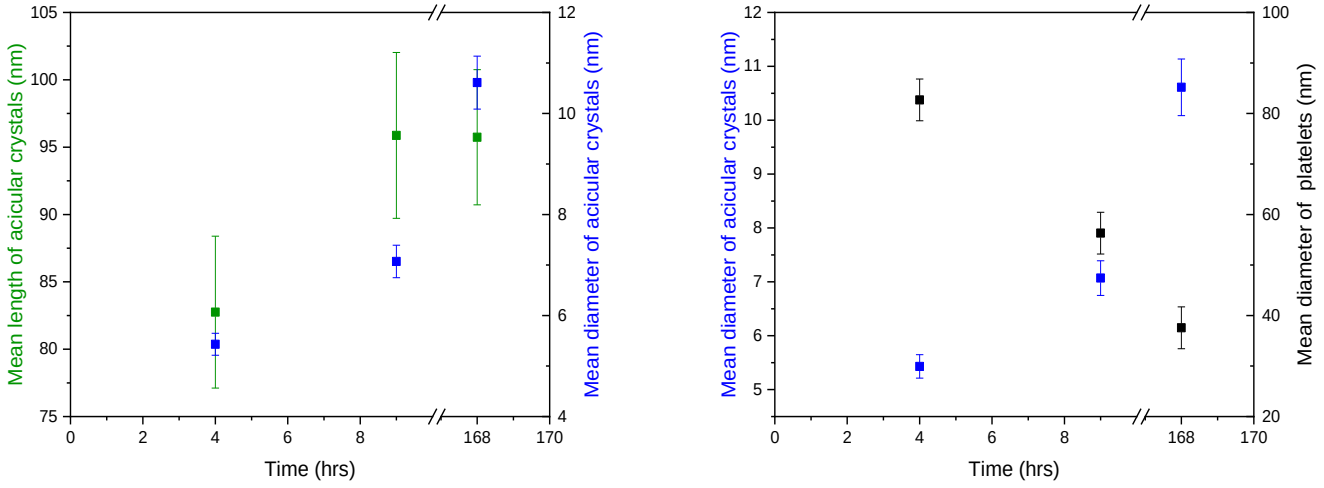

Figure 4.5 Left: Mean length (green) and diameter (blue) of acicular crystals plotted as a function of time. Right: Mean diameter of the acicular crystals (blue) and mean diameter of platelets (black) plotted as a function of time.

The mean length of the acicular crystals become larger as a function of time (Figure 4.4). At 4 hours during the transformation phase from an amorphous phase to a crystalline phase the mean length of the acicular crystals is approx. ~80 nm (Figure 4.5). Whereas at 9 hours and 168 hours the mean length plateaus and measures approx.. 95 nm (Figure 4.5). The length of the acicular crystals varied substantially by ± 5 nm. As with the length the diameter of the acicular crystals continues to expand as a function of time. At 4 hours the mean diameter of the crystals increases from 5 nm at 4 h to 10 nm at 168 h with the long axis length increasing from 85 to 95 nm showing that the fraction of acicular crystals continuously dominates the morphology distribution within the mineralised fibrils (Figure 4.5). The measurements of the crystals discussed are consistent with the measurements reported in the literature [2].

In comparison, the diameter and length of the acicular crystal increased as a function of time whereas the diameter of the platelets decreased from approx. 80 nm to 40 nm within the observed time frame (Figure 4.5). Further analysis shown in figure 4.6 clearly shows that over time the platy crystals diminish in size while the acicular crystals grow in width and length. Hence, it can be concluded that the platelet structures diminish over time whereas the acicular structures increase in occurrence suggesting that the platelet structures gradually dissolve to provide calcium and phosphate for the growth of the acicular phase. Furthermore, the ratio of acicular crystals to platelets increases over time making the platelets more difficult to measure as can be seen in (Figure 4.4), which indicates that the measurements provide an upper value for the platelet geometry and size distribution.

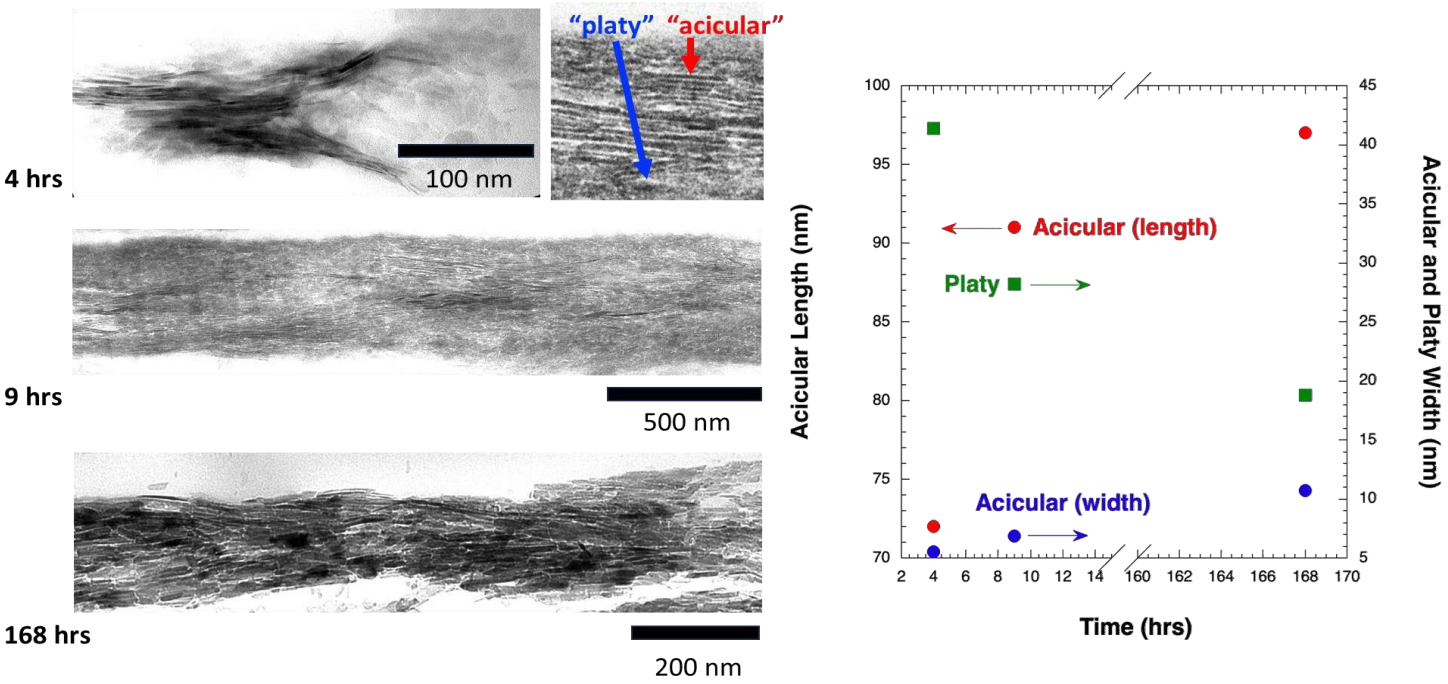

Figure 4.6 TEM size analysis showing how the platy crystals shrink in size as the acicular crystal grown in length and width as a function of time.

Time	Mean length of acicular crystals (nm)	Mean diameter of acicular crystals (nm)	Mean diameter of platelets (nm)
4 hours	82.75	5.43	82.68
9 hours	95.87	7.07	56.31
168 hours	95.73	10.61	37.56

Table 1 Characteristic lengths for the acicular crystals and platelets as determined for 4, 9 and 168 h reaction time.

Another interesting aspect is the change of size distribution for both the acicular and platelet shaped particles. The length and diameter distribution for the acicular crystals varied for the three different time points as shown in Figure 4.7 with each parameter roughly following a Gaussian characteristic. Overall, the crystal length range spread from 20 – 160 nm for 4 h, from 50 – 180 nm for 168 h and for the diameter the range spread was 2 – 6 nm for 4 h and 6 – 18 nm for 168 h. Whereas the length distribution appears to be similar for the 9 h and 168 h time points the diameter gradually increases from the earliest to the latest mineralisation time. For the platelets, a diameter distribution of 20 – 220 nm is found for 4 h to shrink to a spread of 20 – 100 nm for 168 h (Figure 4.7).

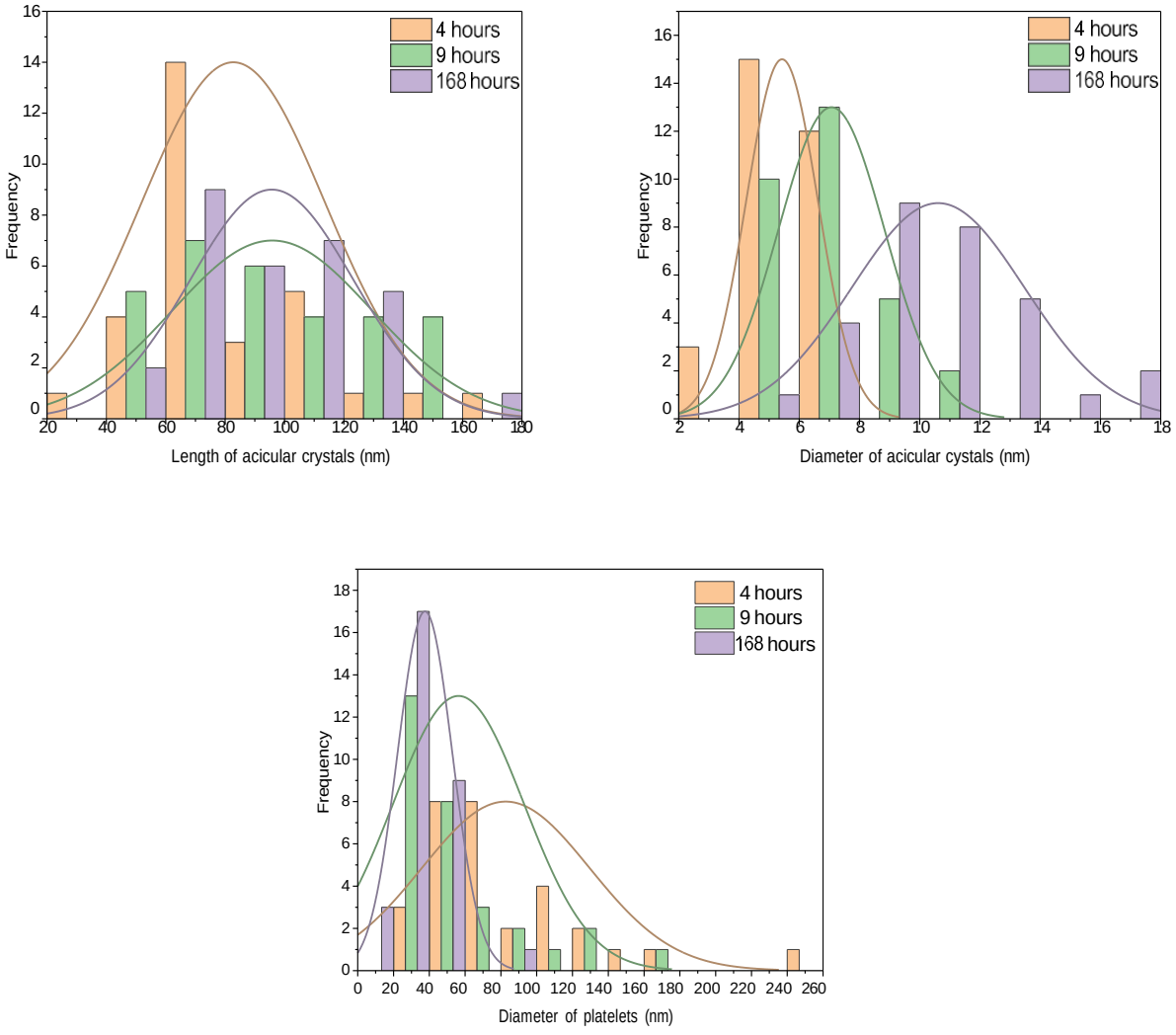

Figure 4.7 Histograms showing the size distribution for both the acicular crystals and platelets plotted as a function of time.

Collagen fibres were mineralised using pAsp of varying molecular weights, 6800, 1400 and 2700kDa. The aim was to see if the varying molecular weights affected the timescale of mineralisation and to see if there we any differences in the bone mineral ie appearance, alignment, orientation. Unfortunately, due to time constraints *ex situ* mineralisation experiments were only conducted using pAsp with a molecular weight of 27000 kDa. From the TEM image (Figure 4.8) the mineral crystals that have grown during mineralisation process appear disordered unlike the crystals that have grown during mineralisation using OPN. The crystals measure approximately 100nm in length and 2-5 nm in width. There appears to only be acicular crystals and no platelet shaped crystals that was observed in the mineralised fibres using OPN.

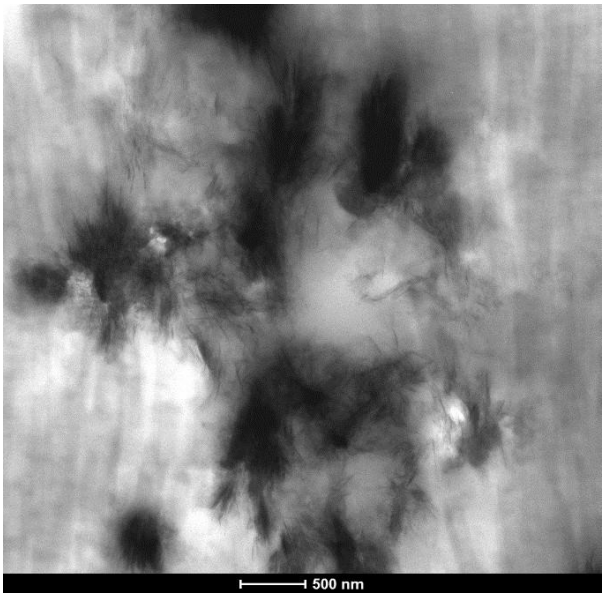

Figure 4.8 TEM image of a collagen fibre mineralised using pAsp.

Fetuin A was also used as very little mineralisation work has been conducted using Fetuin since 2009 [35]. Fetuin has never been used to mineralise collagen fibres in this way before and with the set up designed for this project. The crystals appear disordered and are not aligned with the axis of the collagen fibre nor do the crystals appear to have a specific orientation (Figure 4.9). The crystals are ~ 100 nm in length and ~ 2-5nm in width, again in line with what is written in the literature [2]. Observation show the co-existence of two morphologies of crystals, platelets and acicular cyrstals as with what can be observed in the TEM images of the collagen fibre mineralised using OPN and pAsp. Unfortunately, due to time constraints, no diffraction patterns were gathered.

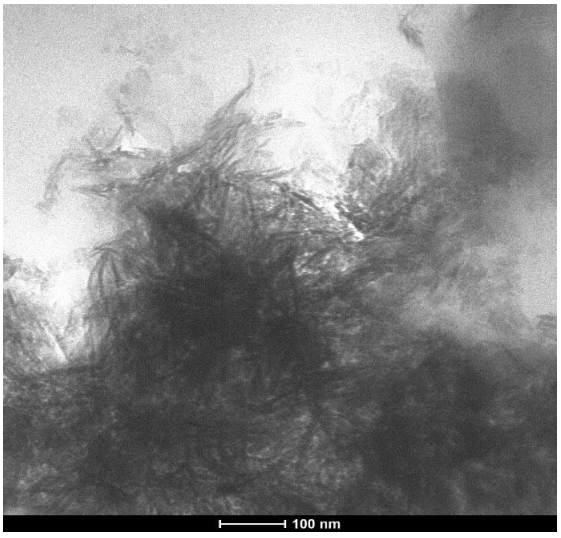

Figure 4.9 TEM image of a collagen fibre mineralised using Fetuin A.

4.2. Discussion

After several decades of research focussing on the characterisation of bone mineral there continues to be an active debate on the bone mineral structure particularly regarding the mineral morphology, mineral size, hierarchical organisation and the presence of an amorphous phase [25], [72]–[77]. Therefore, in this study TEM was used to observe and characterise the bone mineral phases in the in situ mineralised collagen fibres. TEM was used to assess the extent of mineralisation of the in situ mineralised collagen fibres, and to determine whether the mineral phase shows likeness to the mineral organisation observed in native bone. To differentiate between an amorphous phase and a crystalline phase and overall to provide a deeper insight into the size, structural morphology and organisation of the bone mineral.

Longitudinal microtome sections were prepared from collagen fibres that had been mineralised for varying periods (4 hours, 9 hours and 7 days), providing images of the collagen fibres prior

to mineralisation, during mineralisation taking place and after mineralisation. These sections were used to perform TEM imaging. Firstly, observations of the bright-field (BF) images of the collagen fibres showed mineralisation of the collagen fibres had successfully been achieved. The mineral crystals were aligned with their c-axes roughly parallel to the longitudinal axis of the fibrils, mimicking a mineral organisation pattern akin to that observed in bone [14]. The 002 and the 004 reflection arcs can be observed in the diffraction patterns further showing that the [001] c-axis of the HAP crystals are roughly aligned with the collagen fibril axis. The arc extension ranges from ca. +20˚ to –20˚ around the collagen long—axis orientation showing that the crystals' long-axis deviation range is of a similar value. Furthermore, the images closely resemble those from comparable studies focused on mineral organisation within collagen using fully mineralised bone [80], [81], [77]. The BF images and the corresponding selected area electron diffraction (SAED) patterns obtained at varying timescales of the mineralisation process show the morphological amorphous-to-crystalline evolution. The bone mineral clearly exhibits two morphologies, occurring as plate-like and acicular crystals. It is proposed here that the different morphologies of crystal represent a non-HAp phase (amorphous or crystalline) as platelets and a crystalline HAP phase as acicular crystals. The image recorded at 4 hours, the time point at which infiltration occurs, shows there is an increased amount of platelet-shaped nano crystals. At the point where the transition from a non-HAP phase to a HAP phase occurs the images show the platelet-like nano crystals diminish and the amount of acicular crystals increases. Observations of the SAED patterns indicate that both morphologies are crystalline, which means that the platelet-shaped particles could be e.g. octa-calcium phosphate (OCP). Since the lattice plane spacing in both Hap and OCP are very similar it was not possible to decide decisively if the platelets were indeed OCP. However, the SAED indicates that the orientation of the platelet crystals is random whereas the acicular crystal regions show clear arcs indicating textured HAP. A quantitative analysis of the crystal morphologies and their size distribution further supports the theory that the two crystal morphologies observed represent different mineral phases. Measurements show that the diameter of the platelets decreases as a function of time whereas the diameter and length of the acicular crystals continue to expand. Furthermore, it was not possible to measure the platelets after full mineralisation had occurred. Hence, it can be hypothesised that the acicular structures increase in occurrence on the expense of the platelet structures suggesting that the platelet structures gradually dissolve to provide calcium and phosphate for the growth of the acicular phase.

Chapter 5 **Time Resolved *in situ* Raman Spectroscopic Observations of a Biomineralisation Model**

Raman spectra provides chemically specific information of materials such as molecular structure and composition. Raman spectroscopy is a non-invasive, non-destructive technique that requires minimal sample preparation. Samples can be analysed in a variety of environments eg gas and liquid. Identification of materials and results are instant making Raman an increasingly popular technique to analyse biological materials.

[82]Walton et al [82] conducted some of the earliest works employing Raman spectroscopy to the study of calcified tissues such as bone and collagen in the early 1970's, where they obtained Raman spectra for ox tibia and reconstituted collagen of rat tail tendon. In recent decades, Raman spectroscopy has become a more popular and a widely used technique to study different aspects of bone and collagen such as, collagen structure and mineralisation levels [83], collagen fibril orientation [84], bone mineral quality [85], [86]. Most recently, Robin *et al* [63] have conducted *in situ* micro- Raman experiments combining *ex situ* nuclear magnetic resonance (NMR) to monitor the formation of biomimetic carbonated apatite from an acid aqueous solution of phosphate, carbonate and calcium ions. Increasing the pH, they identified a transformation from ACP-OCP-HAP by vapour diffusion. We have achieved similar results, however, our *in situ* set up using a bespoke *in situ* heated cell allowed for a more realistic mimic of both the physiochemical and physiological processes that occur during the mineralisation pathways. The advantages and flexible sample conditions renders Raman spectroscopy an ideal technique for *in situ* time-resolved experiments in an aqueous environment. For the purpose of this experiment Raman spectroscopy was used to mineralise collagen fibers *in situ* and to observe in real time the transition from an amorphous precursor phase to a crystalline phase (HAP) whilst collecting time-resolved data on the mineralisation/transformation process.

5.1. Experimental Design and Setup

As this is the first experiment of its kind, an experimental design was devised and implemented. Both *in situ* and *ex situ,* mineralisation experiments were conducted. Poly-aspartic acid (pAsp) and OPN were used in the *ex-situ* experiments and OPN was used for the *in-situ* experiments. The primary aim of the *ex situ* experiments was to determine the time frames of when mineralisation of the collagen fibres occur, when using the PILP process and using different

acidic polymers (OPN/pAsp) in preparation for the *in situ* experimental design. When using OPN as the mimic, mineralisation is expected to occur as early as 3-4 hours, however, when using pAsp 27000kDa mineralisation takes significantly longer, approximately 72 hours. The difference in mineralisation time scales is likely due to the varying molecular weights. pAsp has a larger molecular weight meaning that it takes longer to penetrate the collagen fibres. *Ex-situ* experiments using pAsp were also conducted for the purpose of mineralising collagen fibres for longer time periods that would not be possible to conduct *in situ* to assess the degree of mineralisation over longer time periods and to characterise them using electron microscopy. Because of the prolonged timescale of mineralisation using pAsp no *in-situ* Raman experiments were conducted. However, an experiment is in the process of being designed to surmount this problem. Once mineralisation time frames were established a time-resolved *in situ* experiment was designed and performed using Raman spectroscopy enabling us to observe and obtain spectra of the transition process of mineralisation from an amorphous phase to a crystalline phase.

Cell design for *in situ* Raman spectroscopy

To conduct the *in situ* time-resolved experiments an *in situ* heating cell was designed (Figure 5.1) to fit into the Raman microscopy stage and that had the capabilities to mimic normal physiological body temperature (37°C), pump through the PILP solution via and inlet and outlet point and hold a sealed vessel to contain the collagen fibre with a transparent window to allow the laser to interact with the collagen.

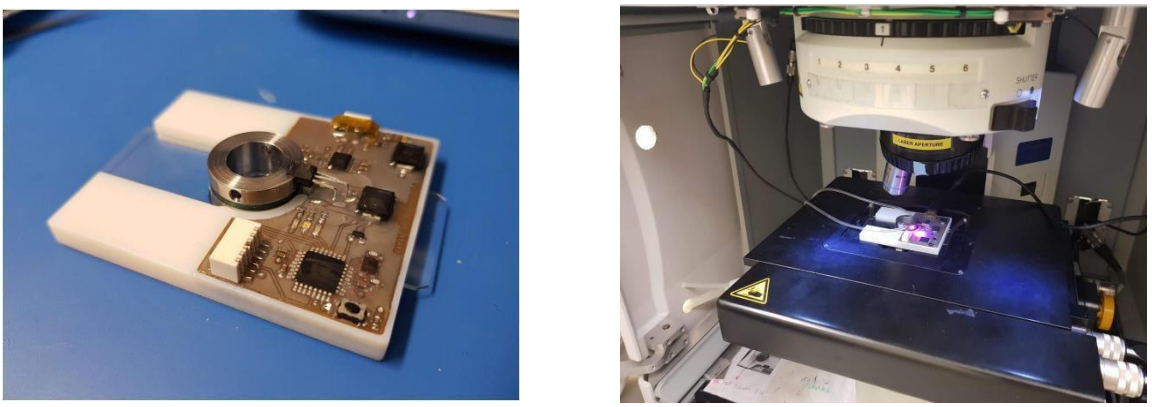

Figure 5.1 Left: An image of the in situ heating cell. Right: An image of the *in situ* heating cell in position in the Raman spectrometer.

5.2. Results

5.1.2 *Ex situ* mineralisation

Ex situ experiments were conducted in an incubator. A collagen fibre was placed into a glass vial containing 50ml PILP solution. The temperature of the incubator was set to 37°C to mimic physiological temperatures. The glass vials were placed into the incubator for varying time periods depending on the polymer being used. For pAsp 2hr, 4hr, 6hr, 8hr, 10hr, 15hr, 20hr, 22hr, 24hr, 48hr, 72hr, 4 days and 7days. For OPN 2hr, 4hr, 6hr, 8hr, 10hr, 12hr and 7days. Once in the incubator samples were gently rotated at 100rpm. Subsequent to mineralisation collagen fibres were washed three times with DI water for 20 minutes to rinse the fibre of any residues. After rinsing, the collagen fibres were then ready to be analysed in the Raman. It was of note that once mineralised, the collagen fibres are noticeably more ridged and whiter.

From, the results obtained from the *ex situ* experiments using pAsp (27kDa, Almander Polymers, Inc) timescales were deduced to 72 hours – 4 days. Between 0 hours and 72 hours no v_1PO_4 peak (962 $^{cm-1}$) can be observed indicating no presence of a crystalline phase. At 72 hours – 4 days the v_1PO_4 peak at 962 $^{cm-1}$ appeared indicating that mineralisation had taken place (Figure 5.2). Conversely, mineralisation was observed as early as 2-4 hours using OPN (Figure 5.3). When using pAsp 27000kDa mineralisation takes significantly longer, approximately 72 hours – 4 days. The difference in mineralisation time scales is likely due to the varying molecular weights. pAsp has a larger molecular weight meaning that it takes longer for the to penetrate the collagen fibres.

pAsp is polydisperse with a molecular weight of 27kDa whereas OPN is monodisperse with varying, smaller molecular weights. Consequently, pAsp will form larger PILP droplets whereas OPN will form smaller PILP droplets. The smaller molecular weights may cause the OPN PLIP droplets to migrate and penetrate the collagen fibres easier, subsequently inducing mineralisation much faster.

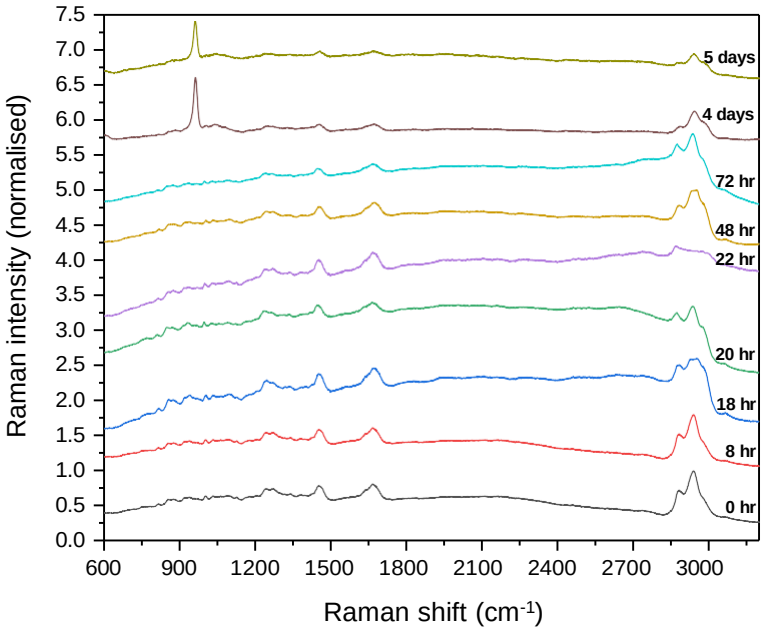

Figure 5.2 *Ex situ* time resolved Raman spectra showing the PO_4 peak shift and evolution using pAsp. At 72 hours – 4 days the v_1PO_4 peak at 962 $^{cm-1}$ can be observed indicating that mineralisation has taken place.

5.2.2 *In situ* mineralisation

In situ experiments were conducted using a Horiba Explora Plus Raman spectrometer using a bespoke heating stage set to a temperature of 37 C. The *in situ* cell was placed into the microscope stage and set to a temperature of 37℃. A single collagen fibre was placed into the vessel and covered with a glass cover slip. The heating stage was connected to a syringe pump loaded with a 60 ml syringe containing PILP solution that was flowed through at a rate of 5ml per hour for up to 8-12 hours. Throughout the experiment, a spectrum was taken every 30 minutes to compile a series of time-resolved spectra showing the mineralisation process. Subsequent to mineralisation, the collagen fibre was removed from the cell and washed three times with DI water for 20 minutes to rinse the fibre of any residues. The fibre was then freeze dried, embedded in resin and microtome sections were prepared and mounted on TEM grids to be characterised using electron microscopy.

The initial Raman spectra (t = 0hrs) from Run 1 match that of native type 1 collagen and show characteristic peaks related to the amide I (1666 $^{cm-1}$ – 1670 $^{cm-1}$) and III (1243^{cm-1}–1246^{cm-1}) bonds, C-H stretching (2939^{cm-1}–2942^{cm-1}) and proline (850^{cm-1}–860^{cm-1}) side groups (Figure 5.3). At 1.5 hours a shift in the v_1PO_4 peak from ~943^{cm-1} to ~948^{cm-1} indicating the transition from

ACP to OCP (Figure 5.3). At 3.5 hours, a distinct shoulder appeared at ~957^{cm-1} indicating the transition from an amorphous phase (OCP) to a crystalline phase (HAP) (Figure 5.3). At 5.5 hours, the intensity from the V_1PO_4 stretching dominates the spectra, indicating a significant presence of phosphate (Figure 5.3). At 8.5 hours we observed the intensity of the v_1PO_4 peak increase further relative to the C-H stretching bond peak, which may indicate an increased take up of mineral with in the collagen fibre.

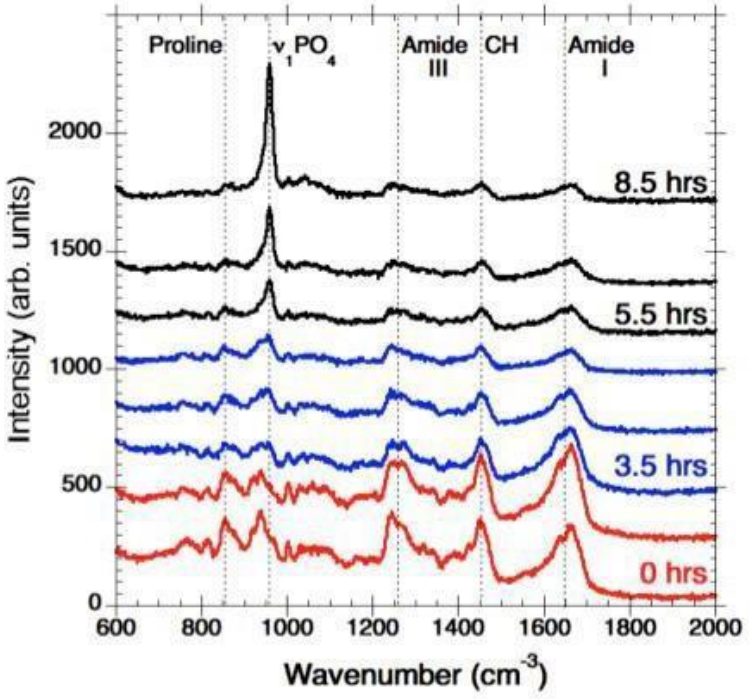

Figure 5.3 *In situ* time resolved Raman spectra (Run 1) showing the PO4 peak shift and evolution.

To determine the accuracy of the peak potions error bars were fitted. Error bars were calculated using the step size of the Raman wavelength shift. The error bars were added to the data based on the error arising from the resolution or step size in the collected data. The data points were around every 0.7^{cm-1} therefore the error in the peak position is +/- 0.35. The error bars show that there is relatively small margin of error in the recorded peak position. Although we see a rapid shift in the v_1PO_4 peak from an amorphous phase to a crystalline phase the ratio data shows this to occur over a longer time period (Figure 5.4) this may indicate that during the transformation process there is a presence of both OCP and HAP before reaching the fully crystalline phase.

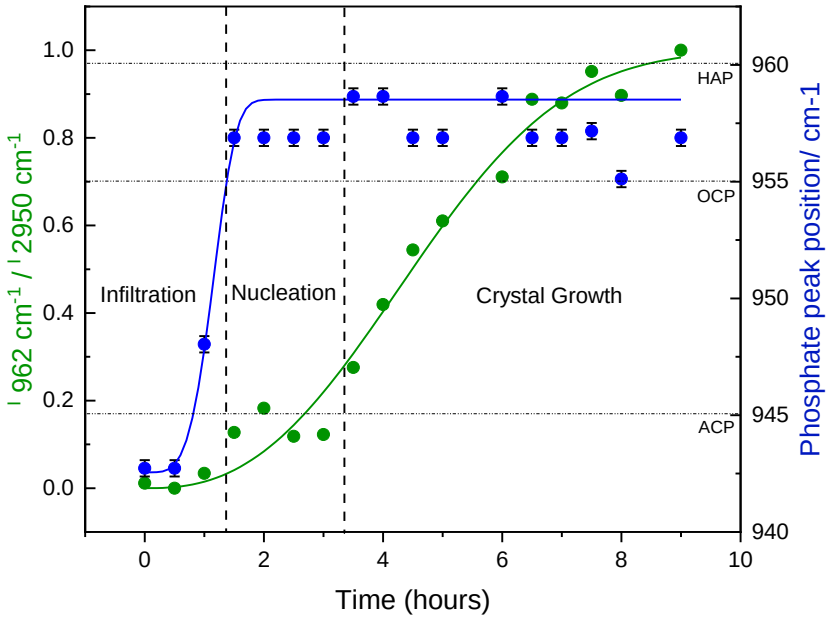

Figure 5.4 The blue circles (with error bars fitted) denote the Raman shift of the PO_4 related peak at approximately 960-2 . The blue line is the Avrami fit to the PO4 peak position. Avrami parameters n = 4.1966. The green circles denote the ratio of the peaks located around the respective wave numbers. The green line is the Avrami fit to the PO_4/CH stretching bond ratio data. Each phase of the mineralisation process has been separated to highlight the time scale of the different phases.

The combined data from the collagen to mineral ratios and the PO_4 peak position (Figure 5.4) shows that the initial infiltration stage of the mineralisation process occurred between 0 hours to 3.5 hours. The infiltration process begins rather rapidly, and then appears to slow down at 2 to 3 hours before another rapid shift occurs as the phase transformation process begins. The phase transformation occurred over approximately 2 hours. At approximately 4 to 10 hours, the transformation appears to be completed and crystal growth continues in the form of HAP. There are slight fluctuations in the v_1PO_4 peak position from approximately 2 hours; this is likely due to refocusing of the microscope as during the time resolved experiments the microscope tended to lose focus over time. There is also a slight drift on the microscope stage, therefore as well as refocusing, some repositioning was also needed.

The kinetics and mechanisms of the transformation from ACP/OCP to HAP was studied using the Avrami model

$$\Phi = 1 - \exp(-kt^n) \quad \text{Eq.7}$$

where the parameter k gives information on nucleation density and growth rates and n provides information on the dimensionality of the growth and the possible impact of diffusion. Observations show that the goodness of fit is satisfactory indicating that the transformation process follows Avrami type kinetics (Figure 5.4). Based on the values that Wong and Czernuszka give of n>3 to either zero nucleation (n = 3), decreasing nucleation rate (n = 3–4), or constant nucleation rate (n = 4) for solvent mediated re-dissolution and re-crystallization processes [87]. Values below 3 indicate diffusion-controlled growth. Observations in the data (Avrami parameters n = 2.5534.) indicate a diffusion-controlled growth followed by a rapid and constant nucleation crystal growth. A value of n = 2 also indicates two dimensional lamellar growth. Observations in this data again indicate a constant nucleation rate, which is in agreement with the ratio data however, n=4 indicates 3 dimensions of growth whereas the ratio data indicates two- dimensional lamellar growth.

5.3. Discussion

This in situ time resolved Raman study builds on recommendations from a previous study [88] of the early stages of mineralisation. It focuses on observing the amorphous precursor phase to calcium phosphate mineralization using PILP. Wingender's work, which successfully mineralized collagen fibres using this process, also established a timetable facilitating the use of advanced in situ characterisation techniques.

The bespoke heated liquid cell designed for the purpose of this Raman study has proved to be an effective new method to successfully mineralise collagen fibres under in situ conditions whilst obtaining valuable results aiding the identification of the different CaP phases during the mineralisation process.

The results show, using the PILP mineralisation process and maintaining a temperature of 37°C, HAP precipitation begins with the formation of ACP that transforms into OCP and then crystallises into HAP. A peak at 945 cm-1 associated with ACP was observed until approximately 2-3 hours when the peak maximum shifted to 955 cm-1, which could be indicative of OCP, at 8.5 hours the intensity of the v_1PO_4 position increased indicating that the majority of the mineral phase was HAP.

The data strongly supports previous findings with regards to the question whether OCP is a precursor of HAP. This theory of the transient phases has already been reported as early as 1970’s whereby, in vitro precipitation studies conducted at room temperature demonstrated that, at a pH of 7.4, amorphous

calcium phosphate transformed into a mineral resembling OCP within 24 hours [89]. A precipitation study conducted by [90] reported similar results and demonstrated that at a pH of 7.4 a complete transformation from OCP to HAP occurred within 24 hours. A more recent in situ Raman study by Robin et al (65) has also shown that (ACP) is initially formed to transform to HAP via OCP. Their experiments closely monitored the pH value and they conclude that the increase in pH value facilitates the transformation of ACP-OCP-HAP. Although pH was not measured during the current experiment, our results are consistent with those reported in literature. In fact, this experiment saw transformation taking place significantly faster than found in the reported work suggesting that using OPN as the process directing agent could in principle speed up the process of phase transformation.

The presented work clearly demonstrates the strength of the heatable flow cell approach for investigating in situ the collagen infiltration and crystal formation. However, there are several limitations that should be noted if conducting further in situ time resolved experiments using the heatable flow cell:

- There are limitations with long precipitation times since the cell can experience defects, such as leakage, which disrupt the experiment and hence requires constant attention by the operator. A more reliable seal could help to remediate this problem.
- The microscope can lose focus over time due to liquid flow related variations of sample position. This leads to the necessity of regularly refocussing to collect spectra.
- Modifications to the experiment and cell would be favourable to monitor pH to add important information on the reaction kinetics.

To summarise this experiment, the bespoke heating cell and the experiment design has been successful in not only mineralising collagen fibres but has produced consistent and convincing data identifying precursor phases. It is known that the close crystallographic structures of OCP and HAP makes a reliable distinction between the two minerals using X-ray or electron diffraction practically impossible. However, Raman spectroscopy is able to allow for a distinction between the different phases. The formation pathway ACP -> OCP -> HAP has previously been reported. This study goes one-step further to observe this transformation in situ and provide its time dependence to gain a better understanding of mineralisation under physiological and pathological conditions.

Chapter 6 *In* situ SAXS/WAXS studies of infiltration and mineralisation of collagen using the PILP process

In situ SAXS and WAXS experiments were conducted with several aims:

- To investigate how the formation of the bone mineral effects the collagen d- banding and hence the overall structure of the collagen fiber, in an attempt to obtain information on where the bone mineral was nucleating and being deposited.
- To obtain information on the size and shape of the mineral crystals as well as their evolution. WAXS was used to study the crystal structure of the bone mineral to determine if it was possible to distinguish between different mineral phases and the possible gradual transformation of amorphous precursor phases into carbonated HAp.
- To compliment the obtained data with those resulting from *in situ* Raman data using the same flow cell.

6.1. Results

Comparing the SAXS/WAXS studies with the Raman measurements provides a unique insight into the impact of mineralisation on the collagen matrix, possible phase transitions and the dynamics and morphological evolution of the mineral phase. It was found that the Raman experiments showed clear evidence of a precursor phase and the SAXS/WAXS studies allow for an identification of collagen and mineral modifications as a function of time.

6.1.1 SAXS

Figure 6.1 shows the SAXS data collected from the *in situ* mineralisation experiment, which ran over the course of 16 hours. The plots relate to the data collected from cake 0 on, the collagen fibre (Figure 6.1). The periodic array of peaks corresponds to the collagen d banding position along the collagen fibre. A variation of the d-banding periodic width was recorded during the mineralisation process revealing a shift of the peak position. This shift indicates either a contraction (shift to higher q-values) or expansion (shift to lower q-values) of the collagen upon mineralisation.

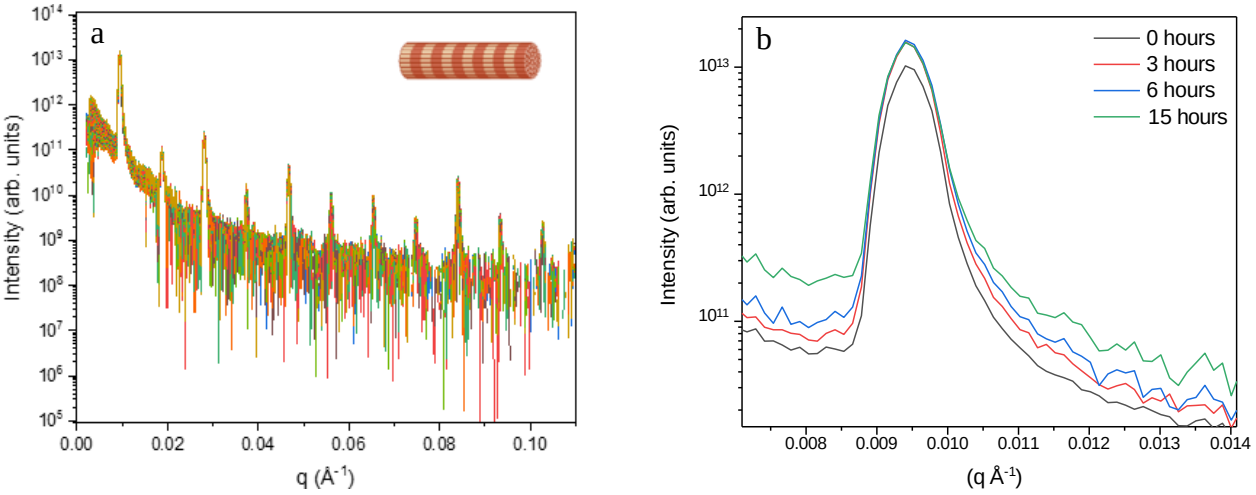

Figure 6.1 1D data taken from on the collagen fiber. The periodic array of peaks relate to the collagen d banding. Inset image: a schematic of a collagen fibre showing individual collagen fibrils. The insert is a schematic of the periodic collagen d-banding b) Expanded area around the first d-banding related maximum in the SAXS pattern at q = 0.01 Å^{-1} at varying time points during the mineralisation process. A slight shift of the peak and it its shoulder at higher q-values can be seen.

Initially, up to 3 hours (120 min) into the mineralisation process, the d-banding width increases as the PILP precursor phase is being taken up into the collagen gap regions (Figure 6.2). After 120 min, the d banding shrinks suggesting that once

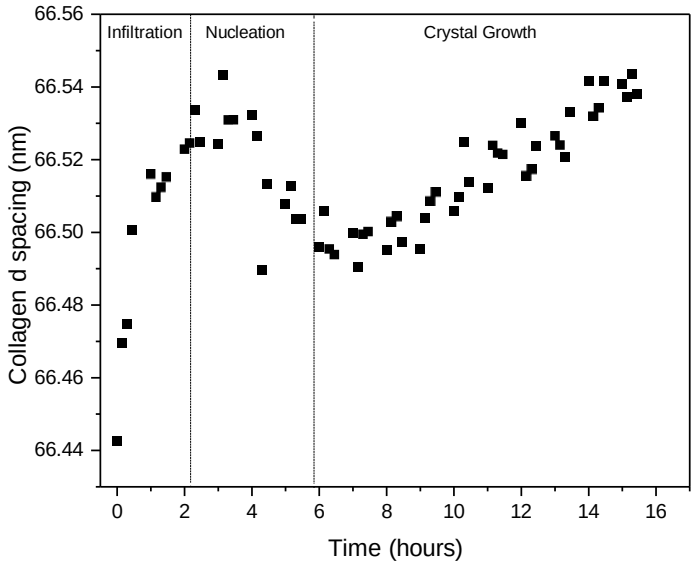

Figure 6.2 SAXS data showing expansion and contraction of the collagen d spacing during the mineralisation process from infiltration to crystal growth process. Three phases of mineralisation can be observed: infiltration, nucleation and crystal growth.

nucleation occurs tthe bone crystals begin to form. Subsequently, after 720 min the d banding again expands as the crystals continuously grow. Calculations show an overall d-spacing expansion of 0.17% averaging across the whole fibre over the time interval of observation (16 hrs or 960 min).

Observations show that the d-banding related peak area is increasing as a function of time (Figure 6.3). During the infiltration period up to 120 min or 2 hrs the peak area remains largely constant to increase rapidly between 3 and 6 hrs as nucleation and initial crystal growth occur, indicating that perhaps a more ordered fashion of growth causing the collagen and the gap regions to expand in long axis direction, suggesting that the collagen experiences mineralisation related stress. After 6 hrs, the peak area plateaus with a slight subsequent decrease, suggesting that no further collagen expansion occurs and a continuous mineral phase has formed.

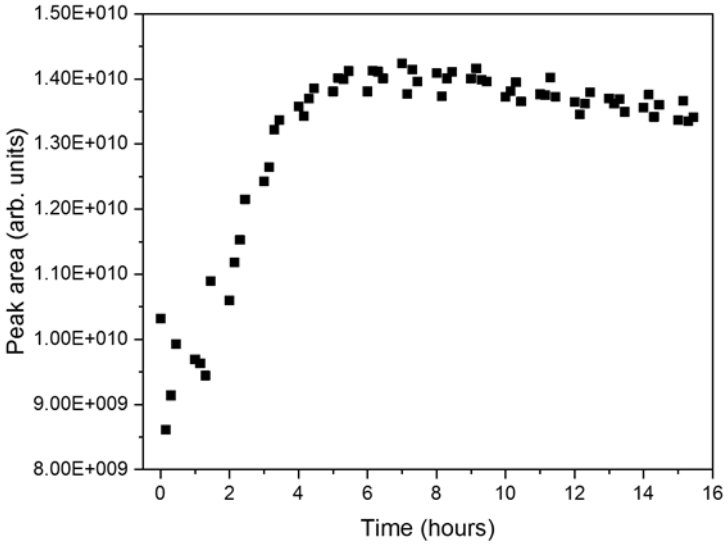

Figure 6.3 D-banding related peak area plotted as a function of time.

For the FWHM observations show, that during the infiltration phase, there is an almost constant behavior up to 3 hours (Figure 6.4). During the nucleation phase, the FWHM increases rapidly. The FWHM is getting broader over time as the crystals are continuously growing, suggesting that the collagen and gap regions experience growth related stress (Figure 6.4).

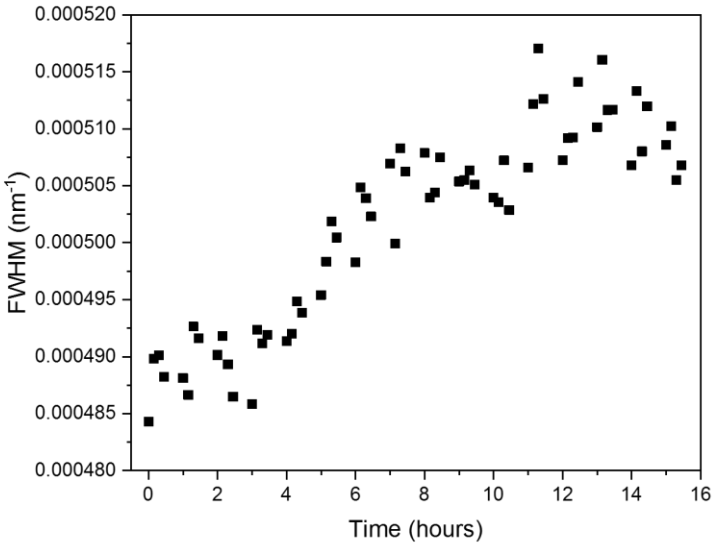

Figure 6.4 FWHM of the first d-banding related peak plotted as a function of time.

A slight peak in the time resolved SAXS patterns appeared at 3 hours and shifts to lower q at 6 hours indicating crystal growth (Figure 6.5a and b). However, at 15 hours the peak is no longer visible possibly indicating that the crystals were no longer growing (Figure 6.5b). These results are consistent with the crystal growth trends that have been observed in the *in situ* Raman and WAXS experiments.

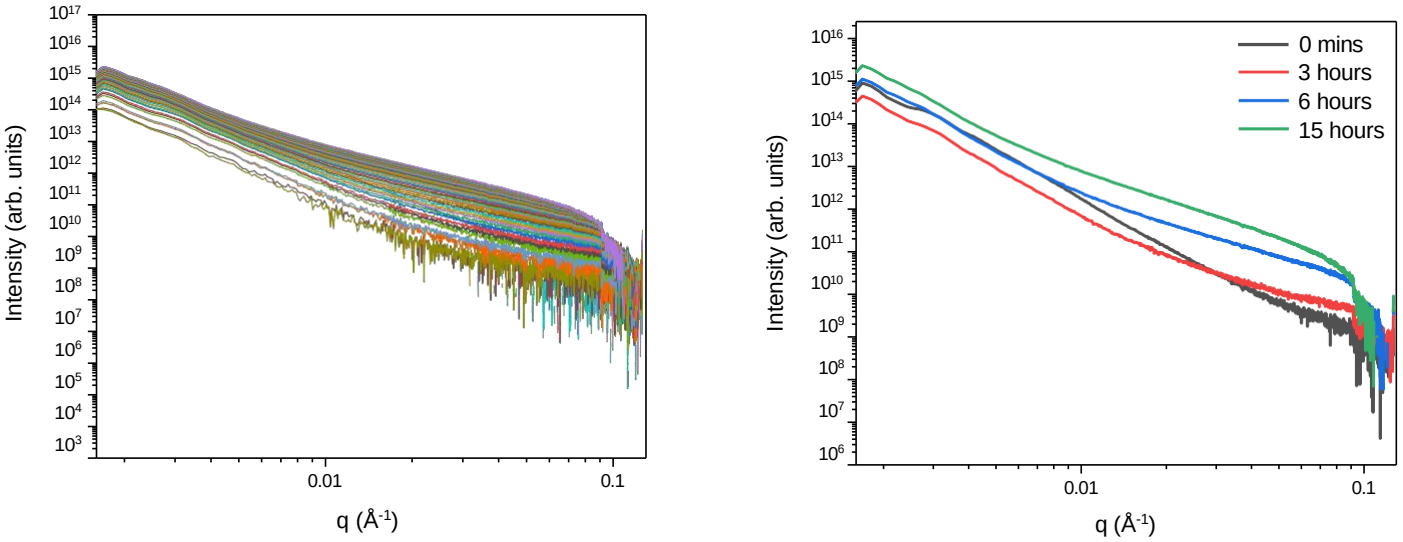

Figure 6.5 a 1D plot of the SAXS scattering intensities from the forming particles within the collagen plotted as a function of time b) A 1D plot of the SAXS scattering intensities from the forming particles within the collagen from inflection points plotted as a function of time.

Given the formation and growth of the particle described from the SAXS patterns, we can use the change in the gradient as a measure of the rate of mineralisation. To obtain the gradient data the 1D SAXS data from the direction perpendicular to the collagen fibre long axis was fitted (Figure 6.5a). During the infiltration phase up to 3 hours there are very few particles formed and the gradient is the lowest (Figure 6.6). The gradient increases between 3 and 16 hours reflecting the increased rate of particle formation (Figure 6.6). This observation is consistent with the findings of the *in situ* Raman experiments.

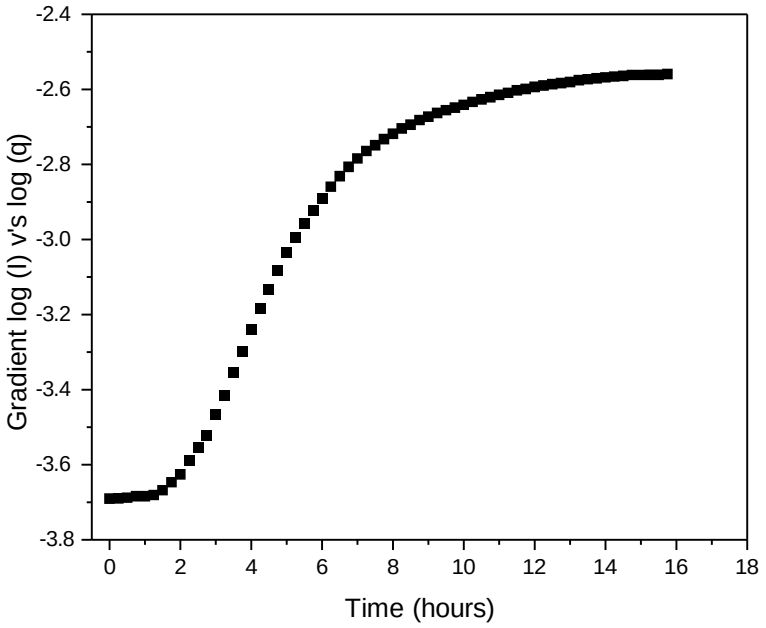

Figure 6.6 WAXS gradient monitoring the evolution and growth of the crystals plotted as a function of time.

A similar trend is observed for the WAXS data, where the {002} peak does not occur during the infiltration phase and, while nucleation and crystal growth progress, subsequently continuously increases. During the initial mineralisation phase, the gradient of the {002} intensity gradually changes (Figure 6.6). As seen from the TEM data mineral crystals evolve as small needle-shaped crystals, continuously aggregating alongside the formation of platelet-shaped nanoparticles. An unambiguous identification of particle and aggregate morphologies is not possible based on the WAXS data since the convolution of different morphological patterns over time does not allow for a specific particle morphology to be matched to the observed scattering curves.

Further analysis of this data provides information on particle size and shape as a function of reaction time. To evaluate the data to this effect and to reduce the signal to noise ratio, five 1D scattering data sets were used to create an average data set. These data sets were chosen for the time interval after the infiltration phase at 3 hours and above since before that no presence of a mineral phase could be detected. In a first step the data sets was subjected to background subtraction. Subsequently the data set for the first time point (no indication of mineral present) was used as background spectrum to be subtracted from all other spectra. The resulting averaged data set was then used for fitting using the SAS software package [ref]. Since due to the

aforementioned difficulty of an unambiguous shape determination no single shape could be assumed, the focus was laid on the size evolution and TEM images were used to provide information on the particle shape. As there is much debate surrounding the shape of HAP crystals an educated guess had to be made on the collective data obtained in this study. Therefore, it was decided to model the data based on a parallelepiped model as this most closely fits the shape of a needle (Figure 6.7). It is worth noting here that only a very limited q range was used when fitting the data (from 0.0092 nm^{-1} to 0.0927 nm^{-1}) only covering particles of a certain corresponding size. Scattering outside this q range should be related to the scattering by aggregating particles. At the onset of the mineralisation process, small crystals appear and then different levels of hierarchy evolve as a function of time. Hence, it is not possible to use one model fit for all of time points. Furthermore, it was found that throughout the experiment the crystals grew at a constant rate in all directions of the model parallelepiped (Figure 6.7 b, c and d). It would appear that initially, small crystals form and they continue to grow into extended needles.

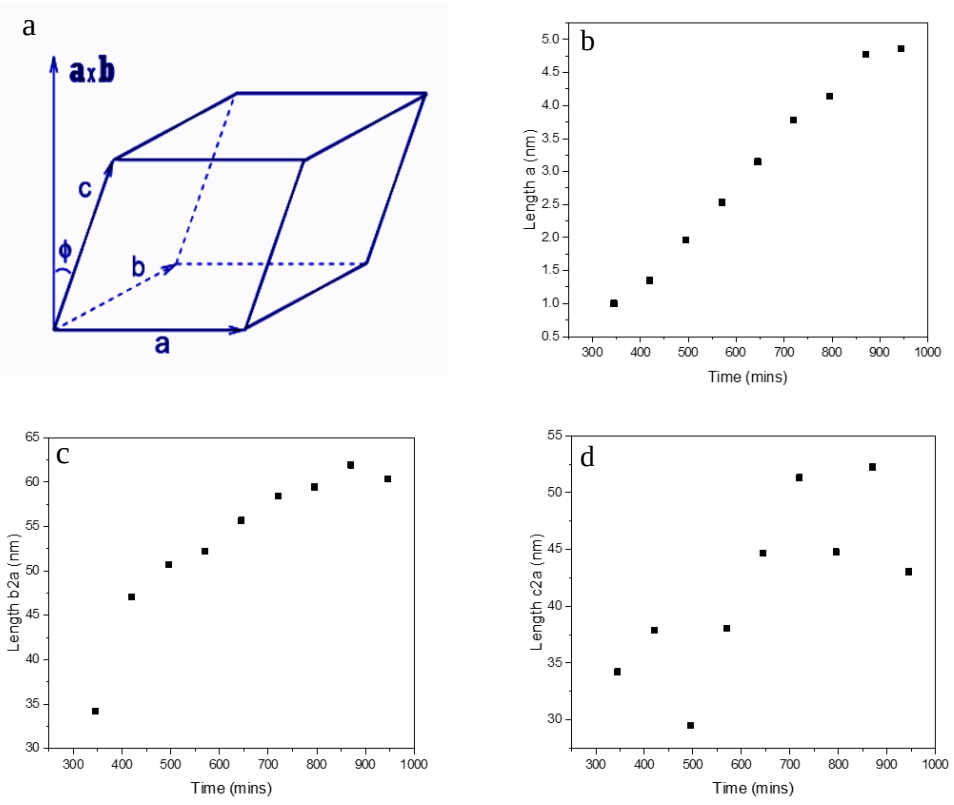

Figure 6.7 Scatter graphs showing a constant growth rate of the crystals in all directions plotted as a function of time.

6.2.1 WAXS

The data shows the evolution of the of the HAP peak around q = 1.83 nm^{-1} (Figure 6.8a). No peak is visible before 2 hours as would be expected, as there is no crystalline phase present during the infiltration phase. At approximately 3 to 4 hours during the phase transformation phase a peak begins to evolve indicating the formation of OCP/HAP.

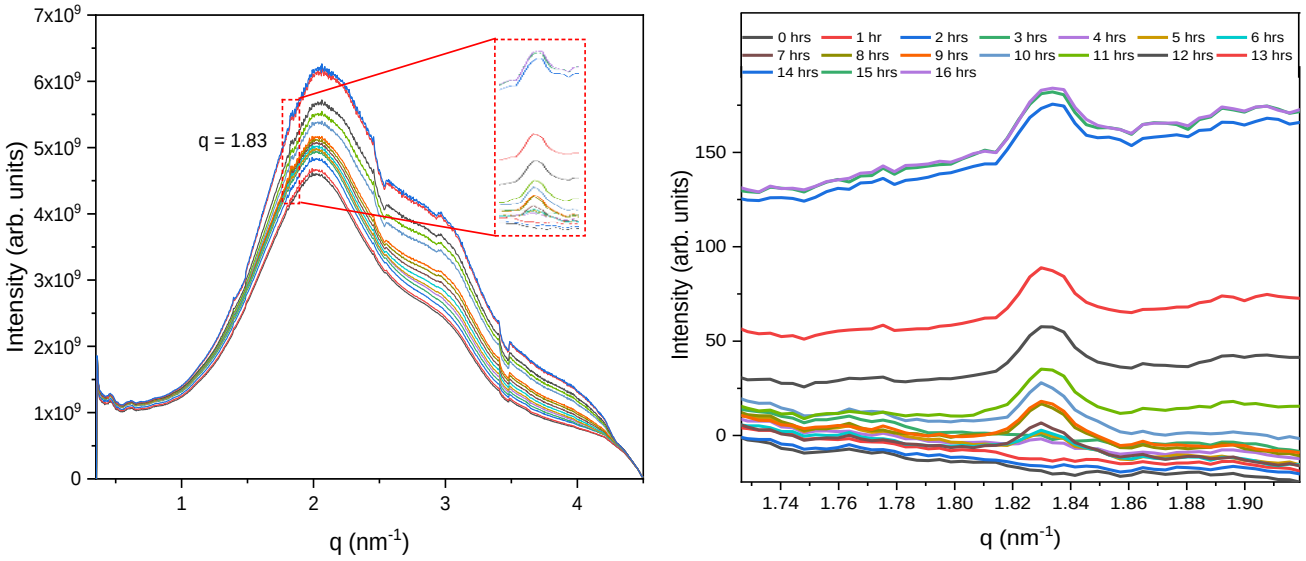

Figure 6.8 a) Time resolved 1D WAXS data showing the evolution of the HAP mineral phase over 16 hours. b) Time resolved data showing the evolution of the HAP peak at q = 1.83 nm-1.

The data below is the data taken from the 1D data in figure 6.8 and plotted as a function of time to give a clearer indication of the shift in the peak position. From 0 to 3 hours, no peak is observed, as already established, there is no mineral present during the infiltration phase (Figure 6.9). At approximately 3 to 5 hours, a peak begins to evolve at q = 1.83 $Å^{-1}$ relating to mineralisation from ACP/OCP to HAP taking place (Figure 6.9). As the mineral continues to grow and mineralise the peak position continues to stay within the region of 1.83 $Å^{-1}$ (Figure 6.9). Again, data and timescales are consistent with observations made in the *in-situ* Raman and SAXS data.

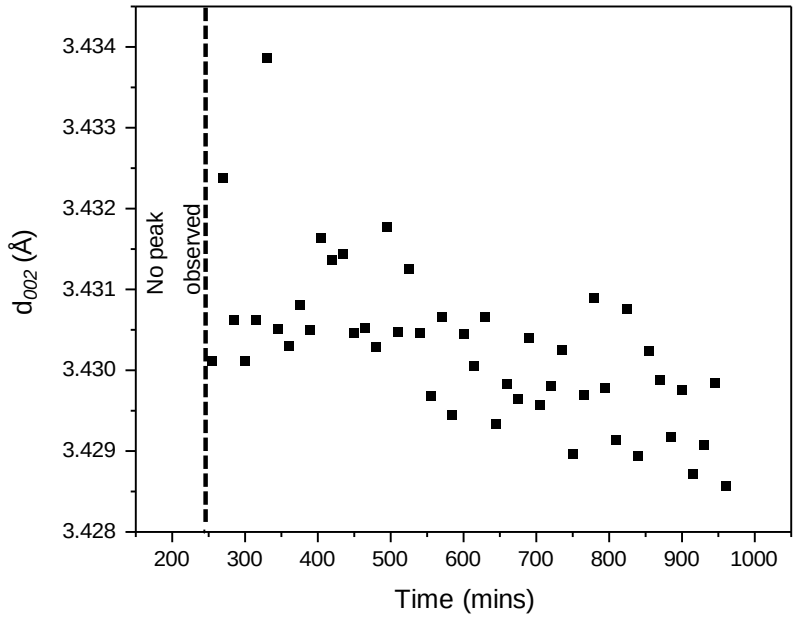

Figure 6.9 The evolution of HAP peak position plotted as a function of time.

Observations show the peak area broaden as function of time (Figure 6.10). Between 0 to 4 hours during the infiltration period there is no mineral present therefore we see no peaks. From approximately 4 to 14 hours, the peak continues to broaden (Figure 6.10). The peak broadening is possibly due to the crystals growing and transforming from ACP to HAP. Between 13 to 16 hours, the peak continues to broaden quite rapidly, further indicating the crystals have mineralised and formed into HAP (Figure 6.10).

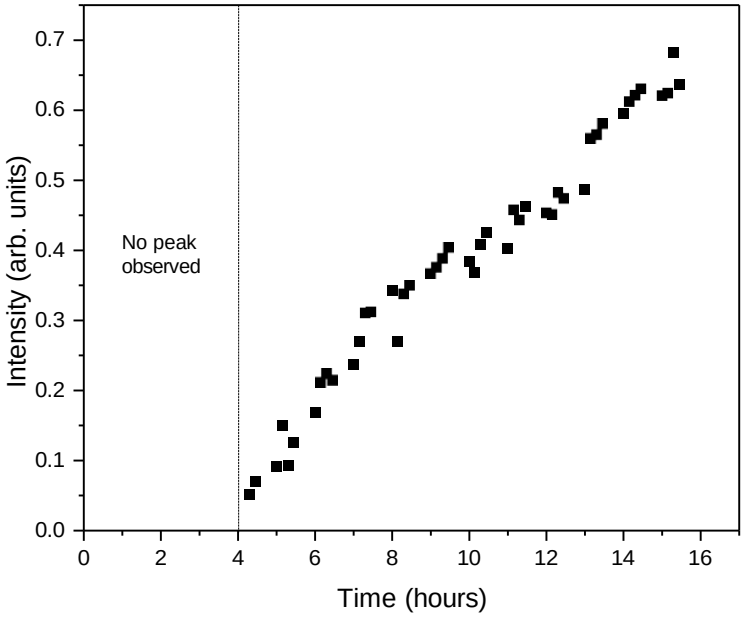

Figure 6.10 A plot of the peak area relating to the WAXS peak at q = 1.83 Å-1 plotted as a function of time.

The FWHM peak broadens between 4 and 6 hours as the crystal start to grow and mineralise (Figure 6.11). The peak width is inversely proportional to the particle size so as the peak broadens slightly overtime this would suggest a smaller size crystal hence the broader peak. Conversely, if the crystals were getting bigger it would be expected that the peak would get narrower. Because the crystal size is not changing enough there is not a significant difference in the peak width. Furthermore, the broadening of the peak is possibly due to crystal strain, as the crystal grows and gets narrower/wider the peak broadens.

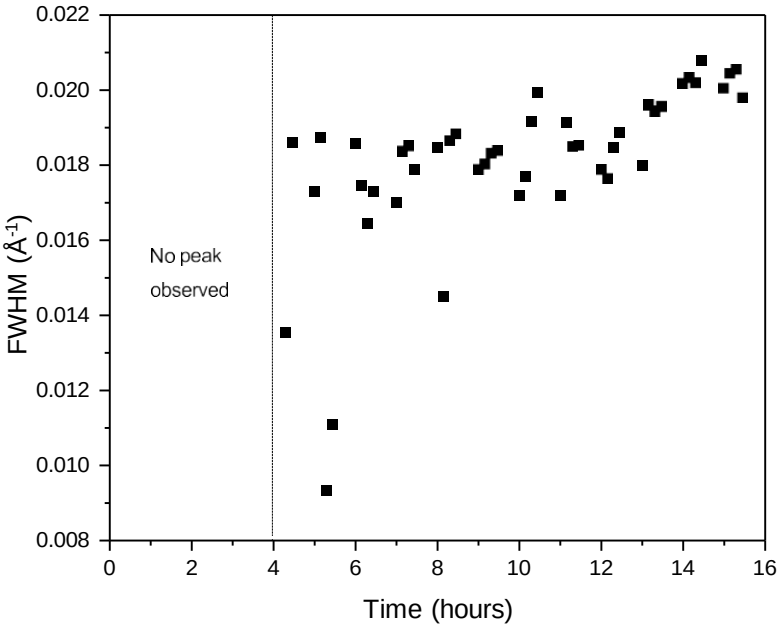

Figure 6.11 A plot of the FWHM relating to the WAXS peak at q = 1.83 Å-1 plotted as a function of time.

6.2. Discussion

Using the custom-designed flow cell to conduct a time-resolved in situ SAXS and WAXS experiment yielded insights into how mineralisation affects the structure of collagen through monitoring the d-band spacing. The results unveiled an initial expansion upon infiltration, followed by contraction during nucleation, and subsequent expansion once the crystal growth phase commenced. Additionally, *in situ* WAXS allowed for the examination of the time-dependent evolution of crystallinity of the hydroxyapatite mineral phase, monitoring changes in the {002} lattice plane reflections. This analysis revealed an increase in peak area over time as more mineral phase is formed and a gradual reduction in lattice plane, correlating with an increased degree of crystallinity.

From the SAXS and WAXS data obtained, it is proposed that in the early stage of mineralisation infiltration of the collagen gap regions occur. This is supported by the observation of an expansion in the D-spacing as a function of time. The results show the D-banding continues to expand during the infiltration phase (approx. 2 hrs) and, after a nucleation phase accompanied by a reduction of the D-spacing, during the crystal growth phase strongly implying that this expansion is related to the crystals forming within the gaps. These results are consistent with the results of the D-banding peak area and the FWHM of the D-banding related SAXS peak. These findings are in line with the model proposed by Traub *et al*. (79) whereby using turkey leg tendon in the early stages of mineralisation they observed with TEM small crystals originating and located in the gap regions of the collagen fibril, proposing these as the sites of crystal nucleation. Furthermore, using cryogenic electron microscopy (cryoTEM),cryogenic electron tomography and low-dose selected area electron diffraction (LDSAED), Nudelman *et al*. (33) demonstrated that the gap and overlap regions are nucleation sites that control the conversion of ACP into apatite crystals. More recently, [91] have observed the similar results using electron tomography (ET) and X-ray diffraction (XRD). Based on their previous studies it is further suggested that crystal shape and size are defined by the geometry of the channels in the gap and overlap regions.

In addition, WAXS patterns show that very little or no crystalline material formed during the infiltration phase (0-2 hours), further signifying a non-crystalline amorphous phase being present in the early phases of the mineralisation process. However, during the nucleation phase (2-6 hours) a peak was observed at q = 1.83 Å−1, corresponding to the (002) lattice plane spacing indicating the formation of HAp. This finding is in line with the time resolved in situ Raman observations.

To obtain further detailed information about the individual crystals size and shape as a function of time the form factor was analysed. To do this a simplistic model, assuming that the mineral phase has a shape of a uniform parallelepiped, proposed by Wagermaier [92] was adapted and fitted to the time resolved SAXS data gathered in this study. The findings showed that the model was too simplistic for a time resolved study of such a complex system comprising mineral particles at different levels of assembly. Therefore, a meaningful fitting was only possible over a very small range at smaller angles in the lower q range. It is assumed the limited, quantitative data gathered was on the smaller isolated structures. The data showed that the crystals continue to grow in all directions however, no defined shape could be determined. Similarly, the gradient plotted from the SAXS data showed increased and continuous mineral

growth. The model did not fit the larger structures where the crystals are beginning to aggregate and cluster together. The TEM images show that there is a distribution of size and morphologies of the crystals making it impossible to fit the data to a model based on a single particle morphology. Since a simplified model was not suitable for this time resolved study a similar model could be designed for gaining further insights into the shape and size of mineral crystals. Some ways this could be done are:

- Redesign the *in situ* cell to reduce liquid thickness and optomise the window materials to reduce the SAXS background scatter, improving the signal to noise in the data for better fitting.
- Obtain data *ex situ* not *in situ*- mineralised the collagen fibres and remove from solution at more defined time points. This would be more advantageous in proving additional information during the infiltration abd transition phase. This will eliminate the problem of scatter from the cell walls and solution.
- Gathering SAXS data from regions of interest i.e. isolated crystals with varied morphologies.
- Scan for longer- this will provide an opportunity to gather better quality data. Increasing the signal to noise ratio will enable better fitting of the data however, beam damage is a potential limiting factor to the exposure times, and it must be remembered that for an *in situ* system the crystal shapes will be constantly evolving so a measurement will therefore be averaged over that given time period.
- Increasing the complexity of the model to incorporate multiple crystal shapes e.g. an ellipsoid shape however, this must go hand in hand with increasing the data quality with the number of variables in the model to ensure the fitting of the model to the data is meaningful.

This study demonstrates that the custom designed cell can be effectively used on I22 beamline for conducting in situ time-resolved experiments while controlling multiple variables, such as temperature and solution flow rate, over an extended period. The cell has successfully facilitated the mineralisation of collagen fibres, enabling the collection of new and insightful data on the mechanisms and kinetics of biomineralisation.

Chapter 7 **A Nano-XRF study of the Infiltration and Mineralisation of Collagen by Polymer Induced Liquid Precursor Phases**

For the purpose of this study, n-XRF mapping was performed on I14 Hard X-ray nanoprobe beamline to give structural and chemically specific information of the mineralised collagen fibres. Using nano-X-ray fluorescence, this study conducted elemental characterisation of a mineralised collagen fibre and to assess the Ca and P distributions with the collagen fibre, giving valuable insights into the mechanism of collagen mineralisation. Previous *in situ* SAXS measurements (I22) have demonstrated a change in the collagen d spacing as the fibre is infiltrated by the PILP phase. Probing the location and distribution of Ca and P within the PILP infiltrated collagen fibre with a 50nm X- ray beam will provide important evidence for the infiltration mechanism. These techniques were also used to compliment the TEM data and to give a multi length scale approach.

7.1. Results

The n- XRF maps show some interesting results in terms of elemental distribution of Ca and P across the mineralised collagen fibre using OPN. Some interesting observations are also made surrounding the mineralisation pattern seen in the collagen fibres mineralised with OPN. The n- XRF map of the mineralised collagen fibre shows that mineralistion throughout the fibre is not homogeneous (Figure 7.1a). The overview map (Figure 7.1a) shows the Ca-Kα intensity at each postion throughout the fibre indicating higher concentrations at the edge of the fibre rather than in the centre of the fibre. There appears to be three distinct bands across the fibre, and outer region, inner region and a central region (Figure 7.1a). The outer region of the mineralised fibre is composed of larger elongated tesselles (Figure 7.1a). The Ca and P map shows lower Ca/P ratios than in the inner region shown by the less intense yellow colour (Figure 7.1b). The inner region has the highest density of Ca and P within the fibre suggesting that the inner region is the most mineralised (Figure 7.1b). The tesselles are more densely packed in the inner region as opposed to the outer and the central region (Figure 7.1 a and b). The central region of the collagen fibre contains much smaller dispersed crystals structures with more isolated Ca rich regions. The presence of bone crystals and P within the inner and central region of the fibres shows evidence of intra fibrillar mineralisation that is observed in native bone [32].

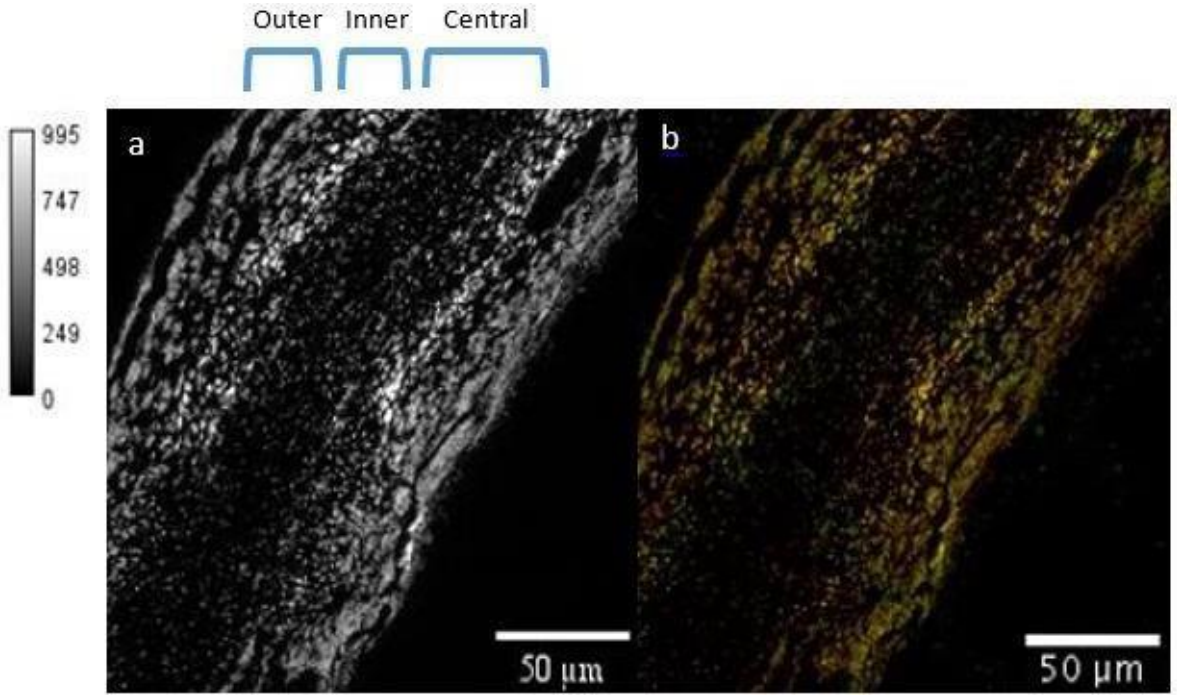

Figure 7.1 a) An overview map showing the Ca-Ka intensity at each position b) A map showing the distribution of Ca and P across the mineralised collagen fibre (yellow = Ca and green = P). The fibre appears to have three distinct regions. The blue indicators are used to define the regions. The distinct regions show and outer region, inner region and a central region.

Further observations show that the collagen fibre is not fully homogeneously mineralised but forms rhombohedral shape tesselles (Figure 7.2 a, b, c and d) again, a similar hierarchical structure that is observed in human and murine bone. Another interesting observation is that the tesselles have a margin surrounding them (Figure 7.2 b and d) suggesting they can move slightly with respect to each other and add an element of elasticity whilst there also being a level of hardness due to the mineralisation. Additionally, if the collagen fibre was fully mineralised it would be expected that this would be seen as one solid block. The periphery of the collagen fibre is much easier to mineralise (extra fibrillar mineralisation) than the centre of the fibre (intra fibrillar mineralisation) therefore, a higher degree of mineralisation can be seen at the prorifery of the fibre, then an intermediate front can be seen as much smaller dispersed mineral aggregates within the centre of the fibre indicating a lower degree of mineralisation (Figure 7.2 a and c). Furthermore, the mineralisation patterns observed in Figure 7.2 b and d reveal a tessellation motif similar to the one reported for human and murine bone (Figure 7.3) [93].

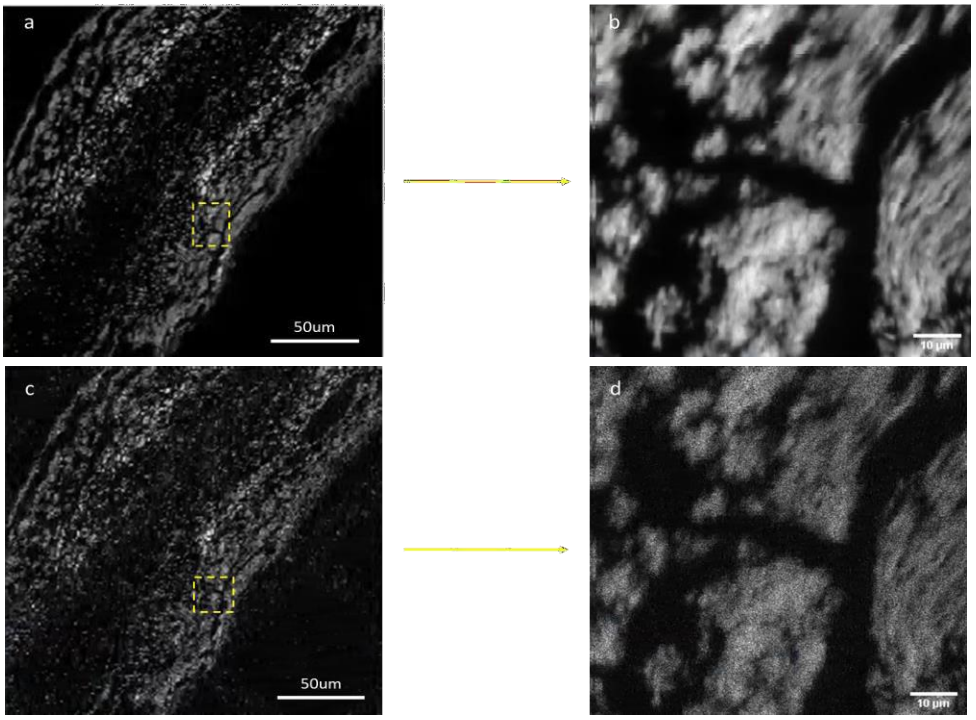

Figure 7.2 A Ca coarse map showing a mineralised collagen fibre, mineralised using OPN. The yellow box indcates the ROI and in particular and regions that clearly show tesselles b) A Ca fine map of the ROI of interest showing a closer image of the tesselles c) A P coarse map showing a mineralised collagen fibre, mineralised using OPN. The yellow box indcates the ROI and in particular and regions that clearly shows tesselles d) A P fine map of the ROI of interest showing a closer image of the tesselles.

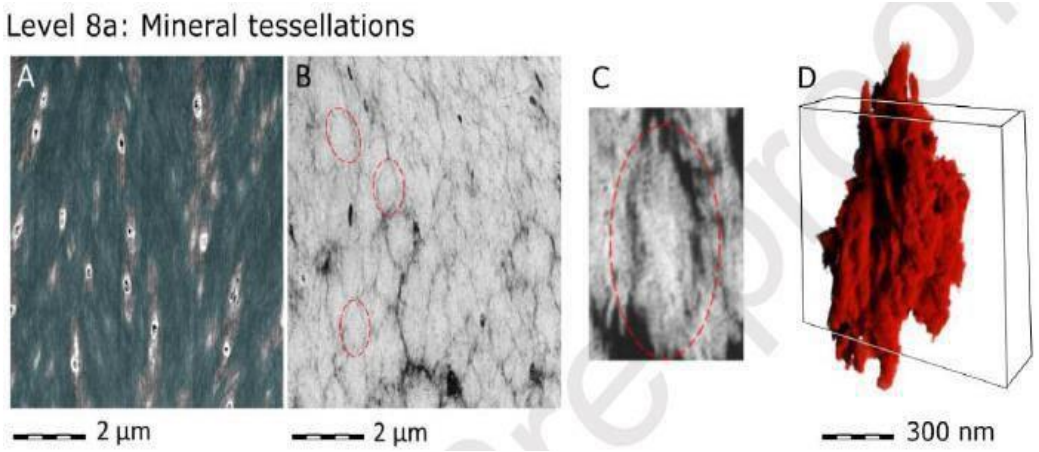

Figure 7.3 An image showing a view of mineral tessellations at different levels in human bone. The image to note is figure C, a magnified 2D image of a mineral aggregate, a "tesselle" observed in human bone.

A fine map of the tesselles at the outer region of the fibre was collected and shows the Ca-Kα intensity at each point across the fibre (Figure 7.4a). The Ca and P distribution map shows the

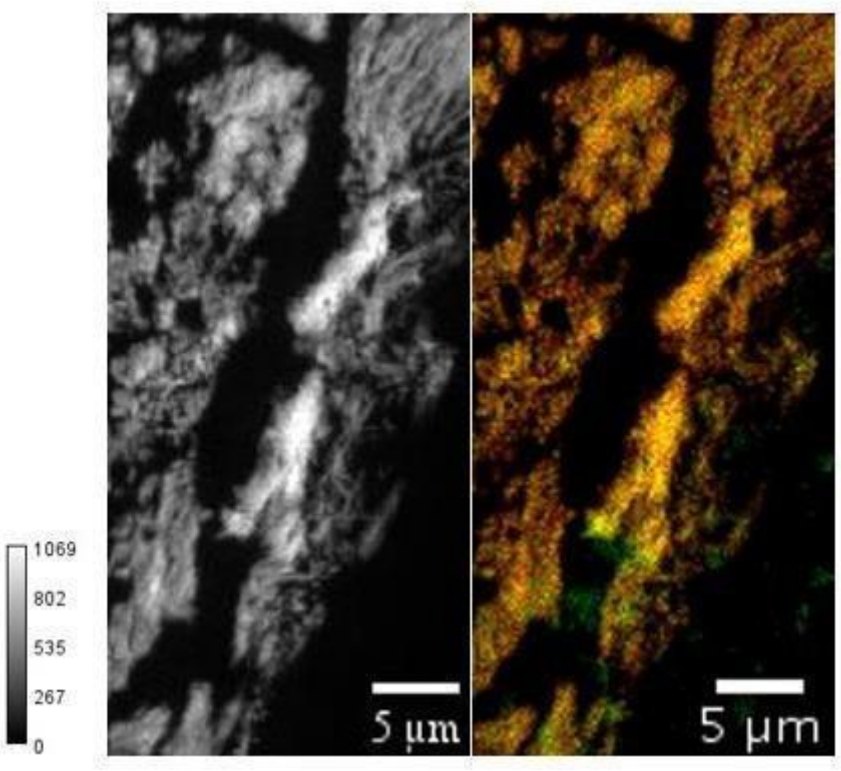

Figure 7.4 a) An overview map showing the Ca-Kα intensity at each position b) A map showing the distribution of Ca and P within the tesselles at the outer edge of the fibre (yellow = Ca and green = P).

regions where there is a P-Ka signal are not correlated with a Ca-Kα signal. The P-Kα signal is seen around the edges of the Ca/P regions with higher concentrations. This suggest that these areas are related to the initial bone mineral formation phase.

For a more quantitative analysis a number of the tesselles observed in the mineralised collagen fibre were measured at their longest axis to determine the diameter and subsequently the size distribution of the tesselles and to compare the measurements with measurements of tesselles observed in native bone (Figure 7.5 a). Measurements were taken using the freehand tool in ImageJ. Interestingly, the quantitative data do in fact show that the measurements of the tesselles are of a similar size to that seen in bone, where measurements have been recorded in the region of 1-2µm [93] (Figure 7.3 a and c). The histogram shows the tesselles measure in the range of 0.5µm to 3µm (Figure 7.5 b). The tesselles at the prorifory of the fibre, where the fibre is more mineralised measure larger, in the region of 2µm to 3µm (Figure 7.5b). Whereas in the centre

of the fibre the tesselles measure much smaller, in the region of 1.5µm to as small as 0.5µm in the less mineralised regions of the fibre (Figure 7.5 a and b). The tessels at the periphery of the fibre appear to be larger and quite closely packed however there is still a margin surrounding them and the tesselles in the centre of the fibre appear more dispersed (Figure 7.5a). Overall the majority of the tesselles measure in the region of 1-2µm which is in line with the measurements recorded in native bone (Figure 7.5b) [93].

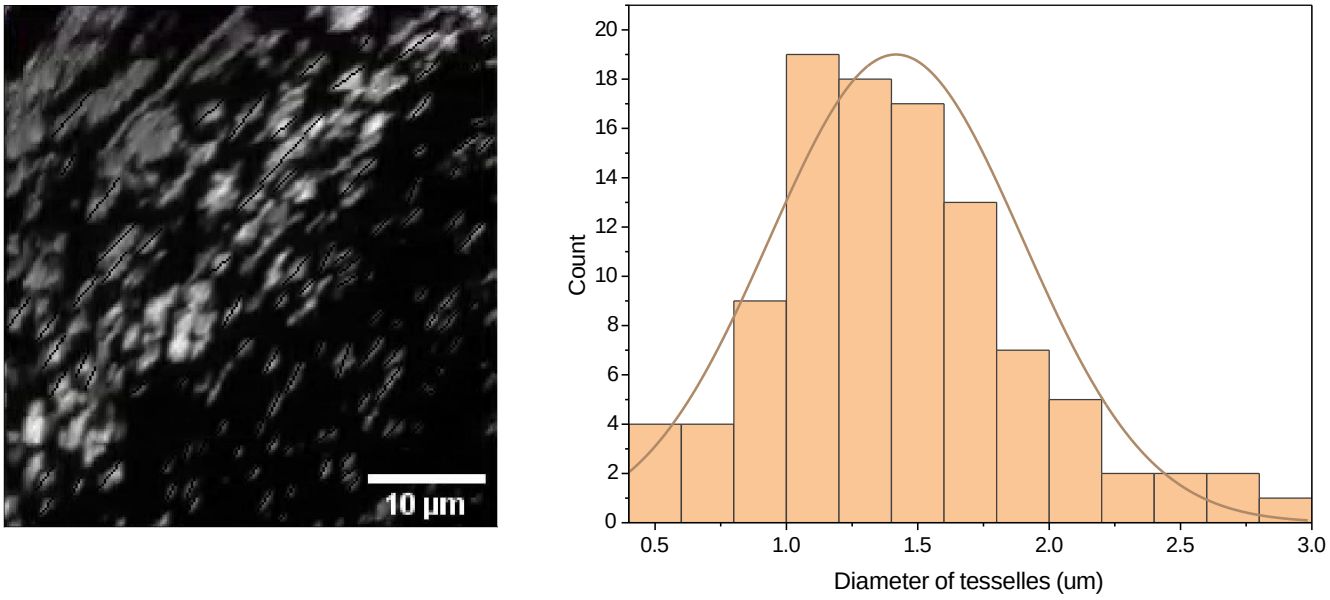

Figure 7.5 An XRF fine map showing the distribution of tesselles with in the mineralised collagen fibre. The black lines indicate the tesselles that were measured. Tesselles were measured along the longest axis to determine their diameter b) A histogram showing the size distribution of the tesselles. The measurements show the tesselles range in size from 0.5µm to 3µm with the majority of the tesselles measuring between 1µm and 2µm.

7.2. Discussion

Using n-XRF to analyse the distribution of the elements Ca and P within the mineralised collagen fibre, this study has revealed an inhomogeneous mineral distribution indicating varying degrees of mineralisation throughout the fibre. The n-XRF maps have provided structural information regarding the bone crystals showing several distinct regions characterised by varying morphologies, from larger more aggregated domains at the fibre periphery, to more isolated domains in the central region.

The inhomogeneous mineralisation of the collagen fibres observed in this study could possibly

be attributed to the sequence of infiltration, nucleation and mineralisation. Initially, the PILP permeates the periphery of the collagen fibres, gradually infiltrating the fibre centre through diffusion, which may result in a longer dwell-time and hence increased mineralisation at the periphery. Notably, it is observed that the mineral phase forming initially at the periphery shows an inhomogeneous pattern, resulting in a tesselle-like formation of mineralised patches, with the mineralisation front gradually moving towards the centre of the fibre. This leads to mineralisation domains very similar to the rhombohedral-shaped tessellations, observed in human and murine bone studies [94]. McKee *et al* [94] demonstrated that there is initially an inhomogeneous mineral distribution with "foci" which then evolve into tesselles that continue to grow until the collagen volume is fully mineralised. The resemblance to human and murine bone mineralisation patterns indicates that the internal collagen structure forms the template for this mineralisation pattern further validating the importance of our findings and suggesting potential applications in biomaterials development and bone disease research since a bone-like mineralisation pattern can be obtained with the PILP process.

Investigations of the Ca and P distribution within the mineralised collagen fibre provided interesting but limited information. Initial studies have shown that n-XRF mapping is a useful and promising technique in this context. Beyond this work, there are several possibilities to build on these. This study was conducted in air, which produces air scatter and absorption, and because the P fluorescence line is low in energy, this attenuation hampers the quantitative analysis of the data. Hence, conducting the n-XRF studies under vacuum could be a way forward to reduce the attenuation and enable better quantitative fitting of the fluorescence data.

X-ray nanoprobe studies allow for the observation of larger sample areas compared to TEM albeit at a lower spatial resolution. It is therefore ideal as a complementary tool for multi-scale characterisation of the mineralised fibres allowing for a better contextualisation of the microstructural studies. Using this technique gives the advantage that we were able to investigate the whole width of the fibre of more than 100 µm, providing insights into the tesselle pattern formation. Combining these studies with spatially resolved XRD (e.g. at micro or even nanoscale scanning X-ray beamlines) would provide interesting complementary information on the presence and distribution of amorphous crystalline phases. Furthermore, the thickness of the sample would need to be optimised to be thick enough to obtain a good diffraction signal without compromising the spatial resolution. Additionally, SEM-EDX could be employed to gather data on chemical composition.

To obtain 3D information on the mineral distribution throughout the collagen fibres synchrotron XRF tomography could be considered. Nano-XRF tomography could provide more detailed structural information on the different morphologies of the bone crystals as well as simultaneously obtaining data on their chemical composition as shown by [95] Walker *et al* who applied this to coccolith biomineralisation of calcite. Focussed ion beam (FiB) or cryo-FiB can be used to prepare thin sections of the mineralised collagen fibres for mapping using n-XRF or XRD techniques. Additionally, FiB-SEM can be employed for volume EM imaging. However, preparing thin sections of mineralised collagen using FiB, easily results in damaged collagen therefore a bespoke preparation protocol would need to be developed. Moreover, cryo-FiB could further enable the preservation of water in the structure. Beside this, X-ray ptychography would be a promising technique offering the resolution needed to visualise the tesselles and their spatial distribution. In fact, successful X-ray ptychography studies have been conducted using bone samples allowing for the observation of osteons [96]. Overall, the reported observations enhance our understanding of the role of physio-chemical processes during collagen mineralisation.

Chapter 8 Conclusion

Collagen mineralisation is a central process in bone formation resulting in a fractal-like organization of the mineral phase within the collagen matrix with the control of the crystal growth being essential for bone to obtain its unique mechanical properties [1]. However, the dynamics of the mineralization process remains a matter of intensive research.

To shed light on these dynamics we applied the polymer-induced liquid precursor (PILP) process [2] using osteopontin as an active protein polymer to mimic this process in vitro using rat-tail derived collagen fibers.

Mineralisation was carried out *in situ* in a custom-made heatable flow-cell allowing for Raman micro spectroscopy as well as small-angle and wide-angle X-ray scattering (SAXS, WAXS) characterisation. The resulting mineralised collagen fibers were subsequently analysed using nano-X-ray fluorescence (nano-XRF) microscopy to map the distribution of Ca and P within the fibers and transmission electron microscopy (TEM) for microstructural investigations.

In situ Raman spectroscopy allowed us to monitor the dynamics of collagen mineralization showing some indications of the presence of an intermediate calcium phosphate phase before hydroxyapatite dominates the spectra. Using the same flow cell, we could perform in situ SAXS obtaining vital information on the impact of mineralization on the collagen D-banding (a periodic pattern caused by repeat sequences of overlap and gap regions in the staggered collagen molecule organisation) revealing initial expansion upon infiltration with subsequent contraction during nucleation followed by expansion once the crystal growth phase was initiated. *In situ* WAXS permitted the study of the time dependent evolution of crystallinity monitoring the {002} lattice planes in the hydroxyapatite mineral phase with a gradual reduction of lattice plane spacing over time related to the increased degree of crystallinity. The in vitro mineralization experiments show significant similarities to the mineralisation patterns observed in bone with Raman microscopy and SAXS/WAXS data being in strong agreement. The mineralisation pattern observed by n-XRF reveals a tessellation motif similar to the one reported for human and murine bone with the crystal morphologies observed by TEM indicating a similar crystal organisation pattern compared to that found in bone.

Monitoring the collagen D-banding and mineralization progress as a function of time, we reveal the occurrence of at least one intermediate mineral phase within the first two hours of mineralization and a change of the D-banding indicating the infiltration, nucleation and growth

phases of the calcium phosphate formation within the collagen matrix.

This further confirms a strong similarity of the physico-chemical processes controlling collagen mineralisation in our in vitro system compared to that found for bone

Appendix

To test that the results of the time-resolved experiment from the *in situ* set up were not a "one off" we repeated the experiments several times. The timescales of the mineralisation process for the time resolved *in situ* data were approximately the same each time for each experiment. This demonstrates that this experiment not only works but that it is repeatable using the same experimental instrumentation, set up and conditions.

As with the first dataset the initial Raman spectra (t = 0hrs) match that of native type 1 collagen and show characteristic peaks related to the amide I and III bonds, C-H stretching and proline side groups (fig 1).

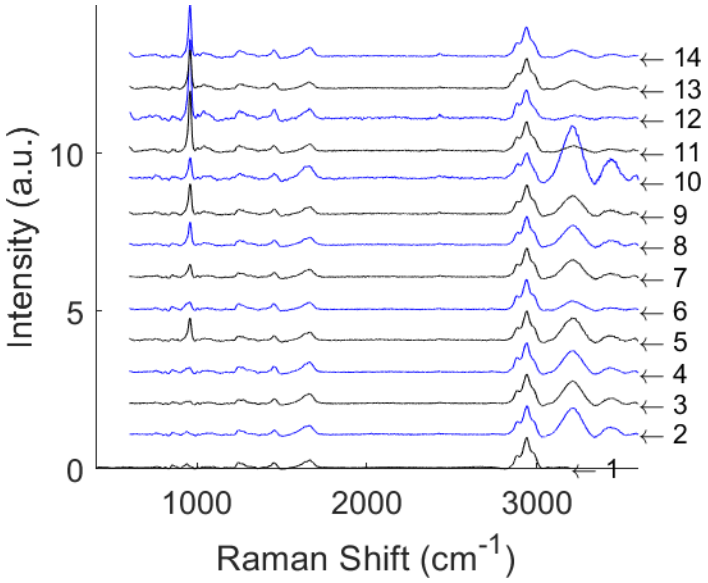

Figure 1. *In situ* time resolved Raman spectra (Run 2) showing the PO_4 peak shift and evolution.

The data from Run 2 (fig 1) show that at approximately 2 to 3 hours the phosphate peak gradually shifts from ~936^{cm-1} to 955^{cm-1} indicating the transformation of an amorphous phase from ACP to OCP. At approximately 4 hours, a shoulder appeared at 957 $^{cm-1}$ indicating the transition from amorphous phase (OCP) to a crystalline phase (HAP). Again, the intensity of the v_1PO_4 peak continues to grow indicating continued mineralisation and an increase in crystallinity of the mineral.

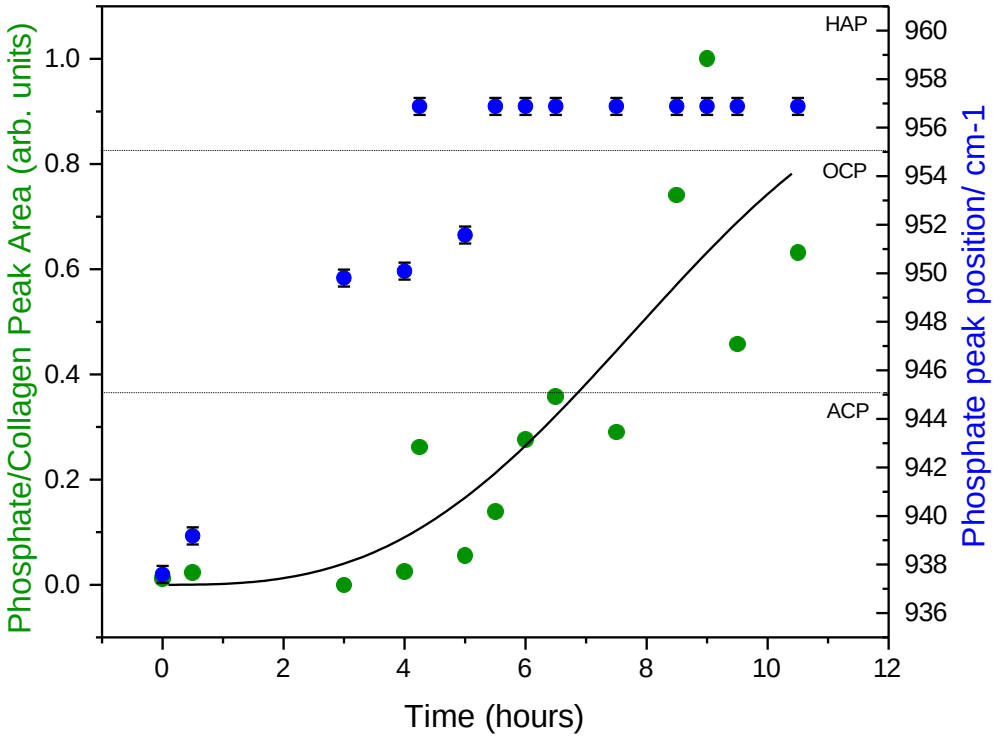

Figure 2. The blue circles (with error bars fitted) denote the Raman shift of the v_1PO_4 related peak at approximately 962 cm^{-1}. The green circles denote the ratio of the peaks located around the respective wave numbers. The black line is the Avrami fit to the v_1PO_4 /CH stretching bond ratio data. Avrami parameter n = 3.003.

The data from the collagen to mineral ratios and the Raman shift of the v_1PO_4 related peak (figs 2 and 3) show that the initial infiltration stage of the mineralisation process occurred quickly between 0 hours to 2 hours. The phase transformation process occurred over approximately 6 to 8 hours (much longer than Run 1). At approximately 6 to 8 hours, the transformation appears to be completed and crystal growth continues in the form of HAP. Observations show that the goodness of fit is unsatisfactory indicating that the transformation process does not follow Avrami type kinetics (fig 2). This may be due to the transformation process occurring over a much slower time scale meaning that there was more amorphous material than crystalline and that the growth of the crystals took longer. However, observations in the data again indicate a diffusion-controlled growth followed by a rapid and constant nucleation crystal growth. The value of n=3 suggests nucleation may be random and the growth of the bone crystals are unhindered.

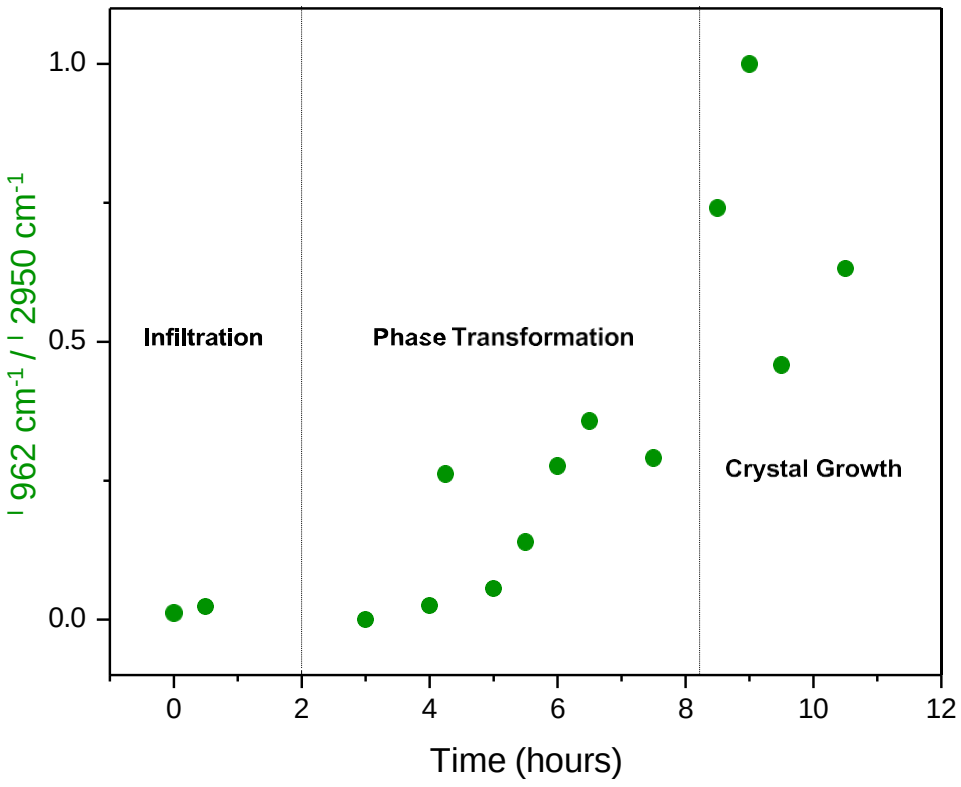

Figure 3. The green circles denote the ratio of the peaks located around the respective wave numbers. Each phase of the mineralisation process has been separated to highlight the different phases.

Again, observations show an overlap in the ratio data and v_1PO_4 peak position data (figs 2 and 3). The ratio data shows that an amorphous phase is present for longer, again, indicating that during the transformation process there is a presence of both OCP and HAP before reaching the crystalline phase.

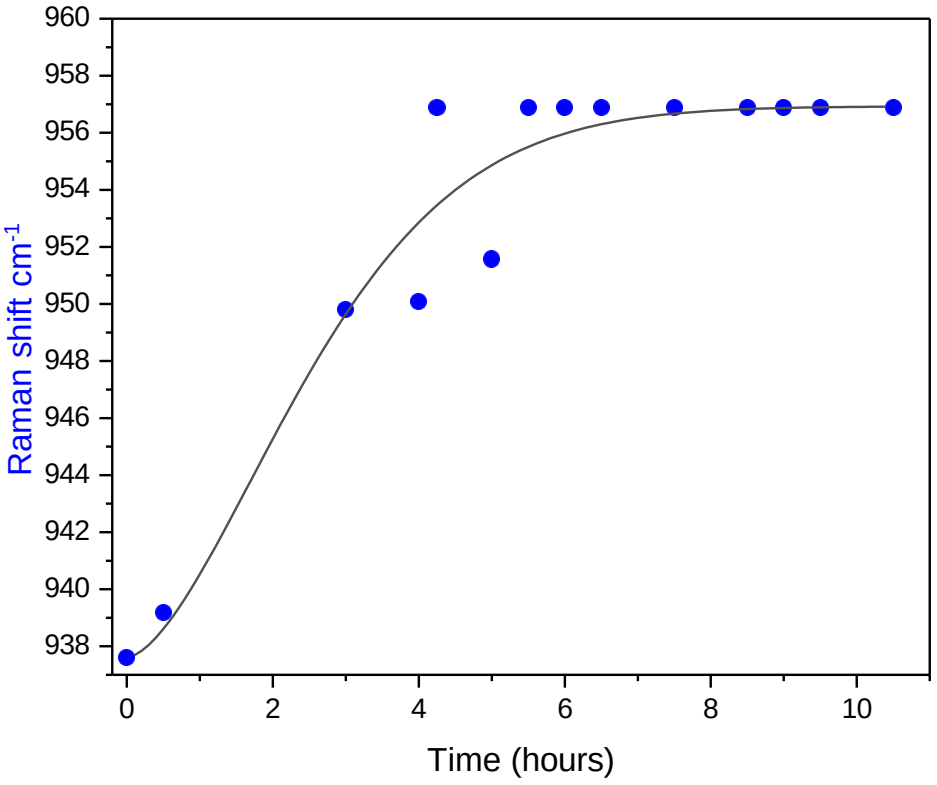

Figure 4. The blue circles denote the v_1PO_4 peak shift. The black line is the Avrami fit to the v_1PO_4 peak shift data. Avrami parameters n=2.1395.

The Avrami fit for the v_1PO_4 peak position does not represent a good fit (fig 4). Observations in this data indicate a diffusion-controlled growth followed by a rapid and constant nucleation crystal growth. A value of n = 2 indicates two dimensional lamellar growth. This is in agreement with the ratio data from Run 1.

The data from the third *in situ* experiment (fig 5) again show that at approximately 1 to 2 hours the v_1PO_4 peak gradually shifts from ACP ~932 $^{cm-1}$ to OCP ~955 $^{cm-1}$ and at approximately 2 to 2.5 hours the peak shifts again to ~959 $^{cm-1}$. The intensity of the v_1PO_4 peak continues to grow indicating continued mineralisation and an increase in crystallinity of the mineral as with the previous experiments.

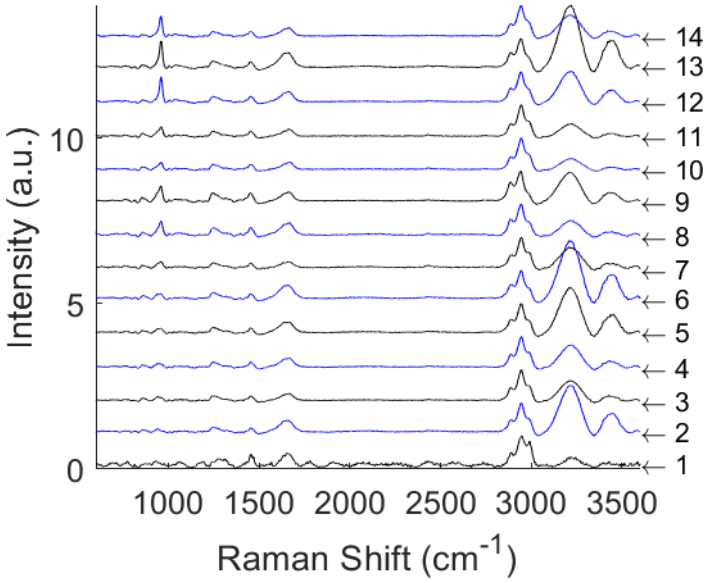

Figure 5. *In situ* time resolved Raman spectra (Run 3) showing the v_1PO_4 peak shift and evolution.

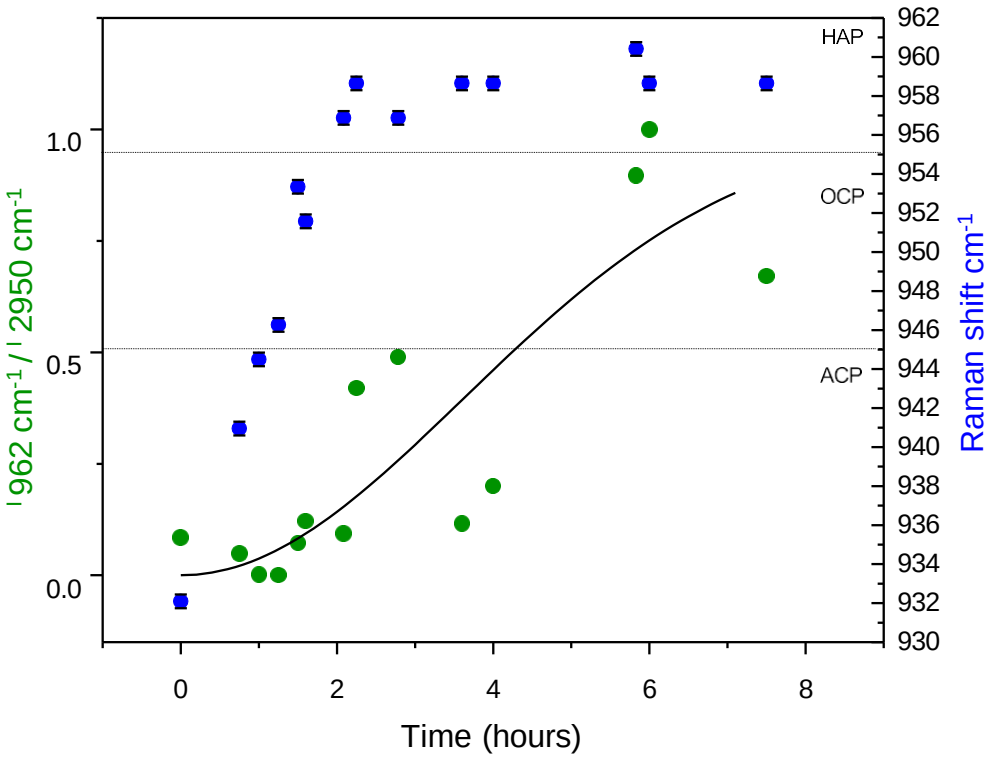

Figure 6. The blue circles denote the Raman shift of the v_1PO_4 related peak at approximately 962 cm^{-1}. The green circles denote the ratio of the peaks located around the respective wave numbers. The black line is the Avrami fit to the v_1PO_4/CH stretching bond ratio data. Avrami parameters n=2.2144.

The data from the collagen to mineral ratios and the Raman shift of the v_1PO_4 related peak (figs 5and 6) shows that the initial infiltration stage of the mineralisation process occurred quickly between 0 hours to 2.5 hours. The phase transformation process occurred over approximately 3.5 hours (approximately the same time as run 1 but much quicker than run 2). At approximately 6 hours, the transformation appears to be completed and crystal growth continues in the form of HAP. Again, the goodness of fit is unsatisfactory indicating that the transformation process does not follow Avrami type kinetics (fig 6). This may be due to the transformation process occurring over a much slower time scale as with the transformation process in Run 1 meaning that there was more amorphous material than crystalline and that the growth of the crystals took longer. The results are agreement with the ratio data from Run 1 and further indicates a diffusion-controlled growth followed by a rapid and constant nucleation crystal growth. A value of n = 2 also indicates two dimensional lamellar growth.

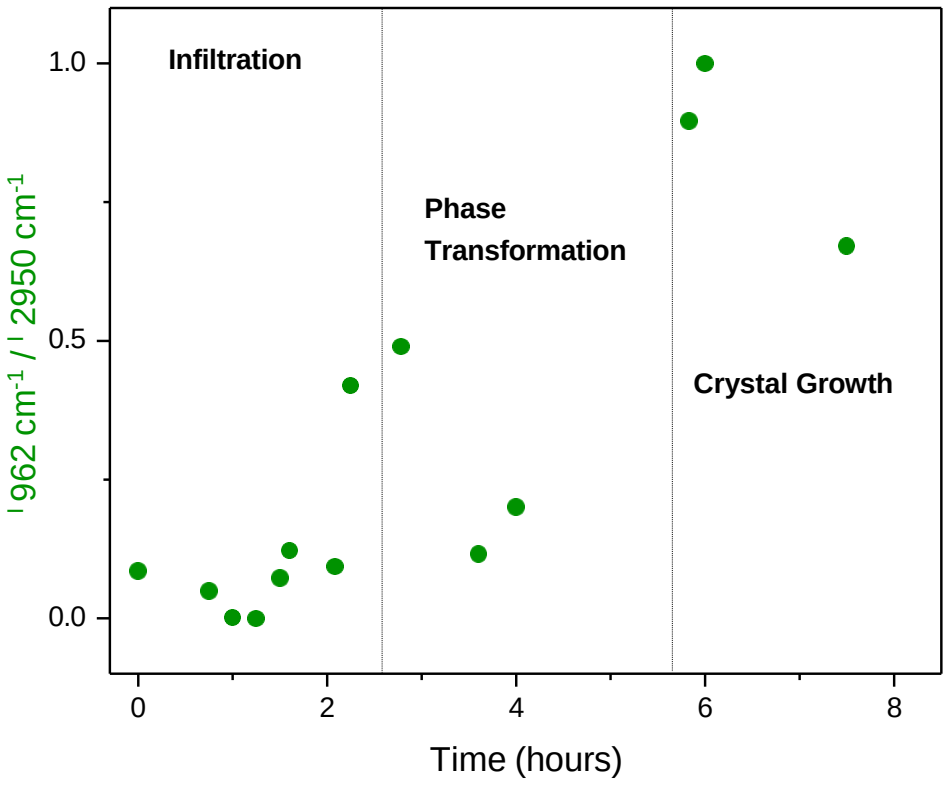

Figure 7. The green circles denote the ratio of the peaks located around the respective wave numbers. Each phase of the mineralisation process has been separated to highlight the different phases.

Again, observations show an overlap in the ratio data and v_1PO_4 peak position data (figs 6 and 7). The ratio data shows that an amorphous phase is present for longer, again, indicating that during the transformation process there may be presence of both OCP and HAP before reaching the crystalline phase.

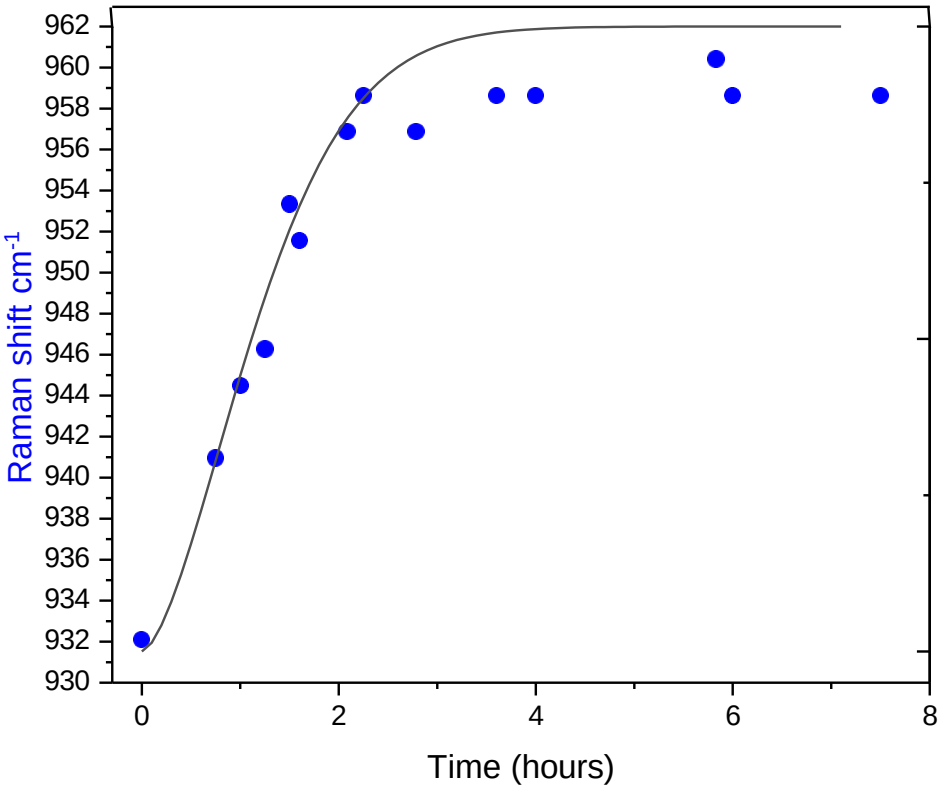

Figure 8. The blue circles denote the v_1PO_4 peak shift. The black line is the Avrami fit to the v_1PO_4 peak shift data. Avrami parameters n=2.3745.

Observations show that the goodness of fit is satisfactory indicating that the transformation process follows Avrami type kinetics (fig 8). Observations in the data further indicate a diffusion-controlled growth followed by a rapid and constant nucleation crystal growth also indicating two dimensional lamellar growth.

Fetuin was also used in the *in situ* experiments. Unfortunately, due to restricted working hours and issues with the experimental set up it was not possible to collect a large part of the data. The data shows the transition from an amorphous phase (ACP) to a crystalline phase (HAP). therefore, only data from the beginning and final hours of the *in situ* experiment were collected. The phase transformation data is missing.

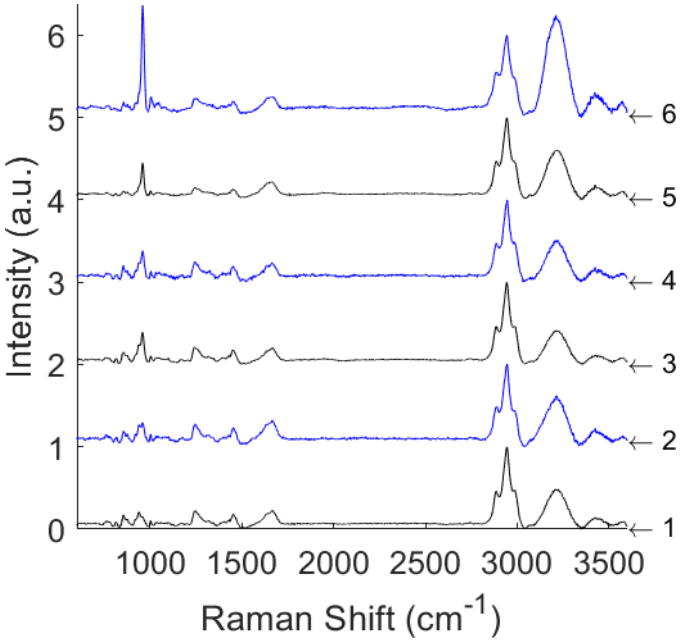

Figure 9. Time-resolved Raman spectra from the *in situ* experiment using Fetuin. Monitoring the PO_4 peak.

As with OPN the initial Raman spectra (t = 0hrs) match that of native type 1 collagen and show characteristic peaks related to the amide I and III bonds, C-H stretching and proline side groups (fig 9). However, mineralisation occurred much at a much faster rate when using Fetuin. We observed a distinct shoulder appear at ~958^{cm-1} as early as 1 hour (figs 9 and 10) whereas in the previous experiments using OPN we do not observe this shift until approximately 2-3 hours. At 24 hrs we observed the intensity of the v_1PO_4 peak increase further relative to the C-H stretching bond peak (figs 9 and 10), which as with the OPN data again, indicating an increased take up of mineral with in the collagen fibre.

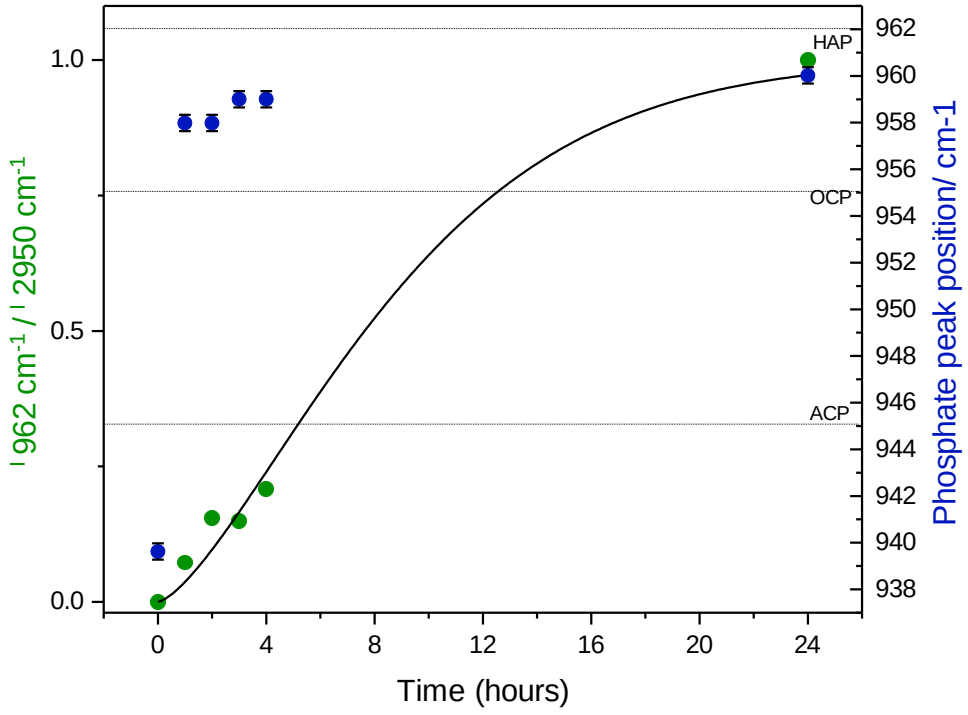

Figure 10. The blue circles denote the Raman shift of the PO_4 related peak at approximately 962 cm^{-1}. The green circles denote the ratio of the peaks located around the respective wave numbers. The black line is the Avrami fit to the PO_4/CH stretching bond ratio data. Avrami parameters n=1.4356.

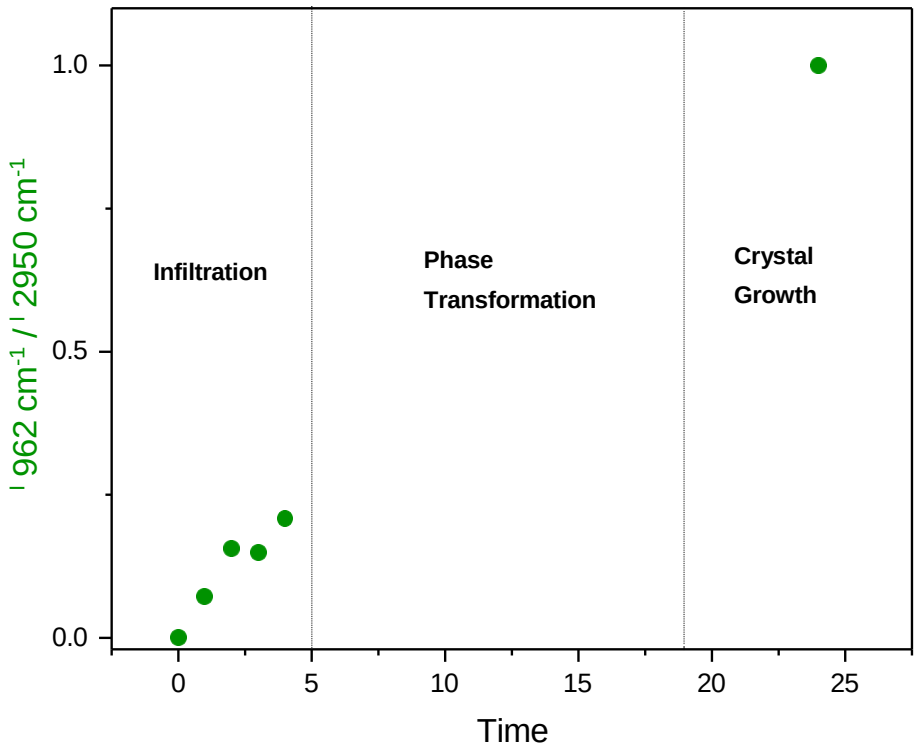

Figure 11. The blue circles denote the Raman shift of the v_1PO_4 related peak at approximately 962 cm^{-1}. The green circles denote the ratio of the peaks located around the respective wave numbers. Each phase of the mineralisation process has been separated to highlight the different phases.

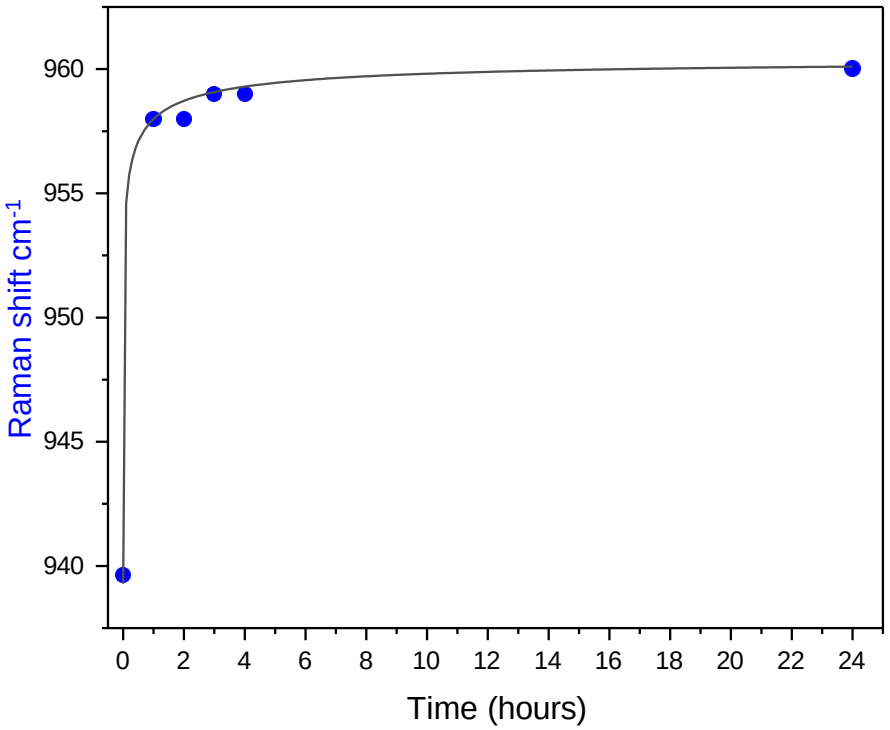

Figure 12. The blue circles denote the PO_4 peak shift. The black line is the Avrami fit to the PO_4 peak position data. Avrami parameters n=0.22757.

Bibliography

[1] L.B. Gower, “Biomimetic Model Systems for Investigating the Amorphous Precursor Pathway and Its Role in Biomineralization Laurie,” *Chem. Rev.*, vol. 1, no. 3, pp. 233–245, 2012.

[2] M. J. Olszta *et al.*, “Bone structure and formation: A new perspective,” *Mater. Sci. Eng. R Reports*, vol. 58, no. 3–5, pp. 77–116, 2007.

[3] N. K. Dhami, M. S. Reddy, and M. S. Mukherjee, “Biomineralization of calcium carbonates and their engineered applications: A review,” *Front. Microbiol.*, vol. 4, no. OCT, pp. 1–13, 2013.

[4] O. B. Boggild, *The shell structure of the mollusks*. Kjobenhavn: A.F Host, 1930.

[5] S. WJ, *Die Bausteine des Tierkorpers in Polarisiertem Lichte*. Bonn: F. Cohen., 1924.

[6] W. W. Clarke FW, “The inorganic constituents of marine invertebrates,” *US Geol. Surv.*, vol. 124, 1922.

[7] S. Weiner, J. Mahamid, Y. Politi, Y. Ma, and L. Addadi, “Overview of the amorphous precursor phase strategy in biomineralization,” *Front. Mater. Sci. China*, vol. 3, no. 2, pp. 104–108, 2009.

[8] E. E. Meyer JL, “A thermodynamic analysis of the amorphous to crystalline calcium phosphate transformation,” *Calcif Tissue Res*, vol. 25, no. 1, pp. 59–68, 1978.

[9] R. PG, “Noncollagenous bone matrix protiens,” in *Principles of bone biology*, 3rd ed., M. T. Bilezikian JP, Raisz, Ed. Amsterdam: Elsevier, 2008, pp. 156–181.

[10] B. Clarke, “Normal bone anatomy and physiology.,” *Clin. J. Am. Soc. Nephrol.*, vol. 3 Suppl 3, pp. 131–139, 2008.

[11] S. Weiner and H. D. Wagner, “The material bone: Structure-mechanical function relations,” *Annu. Rev. Mater. Sci.*, vol. 28, no. 1, pp. 271–298, 1998.

[12] S. Weiner and L. Addadi, “Crystallization Pathways in Biomineralization,” *Annu. Rev. Mater. Res.*, vol. 41, no. 1, pp. 21–40, 2011.

[13] J. Y. Rho, L. Kuhn-Spearing, and P. Zioupos, “Mechanical properties and the hierarchical structure of bone,” *Med. Eng. Phys.*, vol. 20, no. 2, pp. 92–102, 1998.

[14] N. Reznikov, M. Bilton, L. Lari, M. M. Stevens, and R. Kröger, “Fractal-like hierarchical organization of bone begins at the nanoscale,” *Science (80-.).*, vol. 360, no. 6388, May 2018.

[15] S. Weiner, W. Traub, and H. D. Wagner, “Lamellar bone: Structure-function relations,” *J. Struct. Biol.*, vol. 126, no. 3, pp. 241–255, 1999.

[16] H. Lodish, A. Berk and SL. Zipursky, *Molecular Cell Biology 5th Ed*. 2000.

[17] S. Park, T. E. Klein, and V. S. Pande, “Folding and misfolding of the collagen triple helix: Markov analysis of molecular dynamics simulations,” *Biophys. J.*, vol. 93, no. 12, pp. 4108–4115, 2007.

[18] J. P. R. O. Orgel, A. Miller, T. C. Irving, R. F. Fischetti, A. P. Hammersley and T. J. Wess, “The In Situ Supermolecular Structure of Type I Collagen,” *Structure*, vol. 9, pp. 1061– 1069, 2001.

[19] B. Alberts, A. Johnson, J. Lewis, M. Raff, K. Roberts and P. Walter, *Molecular Biology of the Cell*. New York: Garland Science, 2002.

[20] R. Shoulders, M. D and Raines, “COLLAGEN STRUCTURE AND STABILITY,” *Annu. Rev. Biochem.*, vol. 78, pp. 929–958, 2009.

[21] J. A. Petruska and A. J. Hodge, “A Subunit Model for the Tropocollagen Macromolecule,” vol. 51, pp. 871–876, 1964.

[22] B. Wopenka and J. D. Pasteris, “A mineralogical perspective on the apatite in bone,” *Mater. Sci. Eng. C*, vol. 25, no. 2, pp. 131–143, 2005.

[23] C. Combes, S. Cazalbou, and C. Rey, “Apatite biominerals,” *Minerals*, vol. 6, no. 2, pp. 1–25, 2016.

[24] O. Suzuki, “Octacalcium phosphate (OCP)-based bone substitute materials,” *Jpn. Dent. Sci. Rev.*, vol. 49, no. 2, pp. 58–71, 2013.

[25] S. Weiner and W. Traub, “Organization of hydroxyapatite crystals within collagen fibrils,” *FEBS Lett.*, vol. 206, no. 2, pp. 262–266, 1986.

[26] A. Boskey, “Bone mineral crystal size.,” *Osteoporos. Int.*, vol. 14 Suppl 5, pp. 16–21, 2003.

[27] H. J. Höhling, R. Kreilos, G. Neubauer, and A. Boyde, “Electron microscopy and electron microscopical measurements of collagen mineralization in hard tissues,” *Zeitschrift für Zellforsch. und Mikroskopische Anat.*, vol. 122, no. 1, pp. 36–52, 1971.

[28] J. H. Clark, “A study of tendons, bones and other forms of connective tissue by means of X-ray diffraction patterns.,” *Am. J. Physiol.*, vol. 98, pp. 356–358, 1931.

[29] R.A. Robinson and M.L. Watson, “Collagen-crystal relatioships in bone as seen in the electron microscope.,” *Anat. Rec.*, vol. 114, no. 3, pp. 383–409, 1952.

[30] W. E. Brown, N. Eidelman, and B. Tomazic, “Octacalcium phosphate as a precursor in biomineral formation.,” *Adv. Dent. Res.*, vol. 1, no. 2, pp. 306–313, 1987.

[31] A. Eanes, E., Gillessen, I. & Posner, “Intermediate States in the Precipitation of Hydroxyapatite,” *Nature*, vol. 208, pp. 365–367, 1965.

[32] F. Nudelman, A. J. Lausch, N. A. J. M. Sommerdijk, and E. D. Sone, “In vitro models of collagen biomineralization,” *J. Struct. Biol.*, vol. 183, no. 2, pp. 258–269, 2013.

[33] N. A. McKee MD, Farach-Carson MC, Butler WT, Hauschka PV, “Ultrastructural immunolocalization of noncollagenous (osteopontin and osteocalcin) and plasma (albumin and α2HS-glycoprotein) proteins in rat bone,” *J. Bone Miner. Res.*, vol. 8, no. 4, pp. 485–496, 1993.

[34] A. I. Al-Qtaitat, “A Review of Non-Collagenous Proteins; their Role in Bone,” *Am. J. Life Sci.*, vol. 2, no. 6, p. 351, 2014.

[35] P. A. Price, D. Toroian, and J. E. Lim, “Mineralization by inhibitor exclusion. The calcification of collagen with fetuin,” *J. Biol. Chem.*, vol. 284, no. 25, pp. 17092–

17101, 2009.

[36] Z. M. Wang, P. Deurenberg, W. Wang, A. Pietrobelli, R. N. Baumgartner, and S. B. Heymsfield, “Hydration of fat-free body mass: Review and critique of a classic body-composition constant,” *Am. J. Clin. Nutr.*, vol. 69, no. 5, pp. 833–841, 1999.

[37] E. E. Wilson, A. Awonusi, M. D. Morris, D. H. Kohn, M. M. J. Tecklenburg, and L. W. Beck, “Three structural roles for water in bone observed by solid-state NMR,” *Biophys. J.*, vol. 90, no. 10, pp. 3722–3731, 2006.

[38] R. Florencio-Silva *et al*, “Bone tissue: composition and function,” *Johns Hopkins Med J*, vol. 1, no. 145, pp. 10–24, 1979.

[39] M. A. Fernández-Seara, S. L. Wehrli, and F. W. Wehrli, “Diffusion of exchangeable water in cortical bone studied by nuclear magnetic resonance,” *Biophys. J.*, vol. 82, no. 1, pp. 522–529, 2002.

[40] Y. Wang *et al.*, “Water-mediated structuring of bone apatite,” *Nat. Mater.*, vol. 12, no. 12, pp. 1144–1153, 2013.

[41] Y. A. Lazarev, B. A. Grishkovsky, T. B. Khromova, A. A. Lazareva, and V. S. Grechishko, “Bound water in the collagen-like triple-helical structure,” *Biopolymers*, vol. 32, no. 2, pp. 189–195, 1992.

[42] M. Unal, S. Yang, and O. Akkus, “Molecular spectroscopic identification of the water compartments in bone,” *Bone*, vol. 67, pp. 228–236, 2014.

[43] M. Granke, M. D. Does and J. S. Nyman, “The Role of Water Compartments in the Material Properties of Cortical Bone,” *Calcif. Tissue Int.*, vol. 97, no. 3, pp. 292–307, 2015.

[44] N. Kohli *et al.*, “Bone remodelling in vitro: Where are we headed?: -A review on the current understanding of physiological bone remodelling and inflammation and the strategies for testing biomaterials in vitro,” *Bone*, vol. 110, pp. 38–46, 2018.

[45] D. J. Hadjidakis and I. I. Androulakis, “Bone remodeling,” *Ann. N. Y. Acad. Sci.*, vol. 1092, pp. 385–396, 2006.

[46] F. Xu and S. L. Teitelbaum, “Osteoclasts: New Insights,” *Bone Res.*, vol. 1, pp. 11–26,

2013.

[47] S. L. Teitelbaum, “Bone remodeling and the osteoclast,” *J. Bone Miner. Res.*, vol. 8, no. S2, pp. 523–525, 1993.

[48] J.-M. Delaisse, “The reversal phase of the bone-remodeling cycle: cellular prerequisites for coupling resorption and formation,” *Bonekey Rep.*, vol. 3, no. AUGUST, pp. 1–8, 2014.

[49] T. T. Thula, F. Svedlund, D. E. Rodriguez, J. Podschun, L. Pendi, and L. B. Gower, “Mimicking the nanostructure of bone: Comparison of polymeric process-directing agents,” *Polymers (Basel).*, vol. 3, no. 1, pp. 10–35, 2011.

[50] H. Libouban, R. Filmon, A. Mauréac, M. F. Baslé, and D. Chappard, “Fetuin and osteocalcin interact with calcospherite formation during the calcification process of poly(2-hydroxyethylmethacrylate) in vitro: A Raman microspectroscopic monitoring,” *J. Raman Spectrosc.*, vol. 40, no. 9, pp. 1234–1239, 2009.

[51] W. Jahnen-Dechent *et al.*, “Cloning and targeted deletion of the mouse fetuin gene,” *J. Biol. Chem.*, vol. 272, no. 50, pp. 31496–31503, 1997.

[52] C. B. Williams, D.B., Carter, “The Transmission Electron Microscope,” in *Transmission Electron Microscopy*, Boston, MA: Springer US, 2009, pp. 3–22.

[53] C. B. Williams, D.B., Carter, “Scattering and Diffraction,” in *Transmission Electron Microscopy*, Boston, MA: Springer, 2009, pp. 23–38.

[54] C. B. Williams, D.B., Carter, “Elastic Scattering,” in *Transmission Electron Microscopy*, Boston, MA: Springer, 2009, pp. 39–51.

[55] C. B. Williams, D.B., Carter, “Inelastic Scattering and Beam Damage,” in *Transmission Electron Microscopy*, Boston, MA: Springer, 2009, pp. 53–71.

[56] H. Schwarz and K. R. Asmis, “Identification of Active Sites and Structural Characterization of Reactive Ionic Intermediates by Cryogenic Ion Trap Vibrational Spectroscopy,” *Chem. - A Eur. J.*, vol. 25, no. 9, pp. 2112–2126, 2019.

[57] N. Pleshko, A. Boskey, and R. Mendelsohn, “Novel infrared spectroscopic method for

the determination of crystallinity of hydroxyapatite minerals," *Biophys. J.*, vol. 60, no. 4, pp. 786–793, 1991.

[58] E. P. Paschalis, R. Mendelsohn, and A. L. Boskey, "Infrared assessment of bone quality: A review," *Clin. Orthop. Relat. Res.*, vol. 469, no. 8, pp. 2170–2178, 2011.

[59] W. Querido, N. Shanas, S. Bookbinder, M. C. Oliveira-nunes, B. Krynska, and N. Pleshko, "Mineral : From Amorphous Precursor to Mature Crystal," vol. 145, no. 3, pp. 764–776, 2021.

[60] S. J. Gadaleta, E. P. Paschalis, F. Betts, R. Mendelsohn, and A. L. Boskey, "Fourier transform infrared spectroscopy of the solution-mediated conversion of amorphous calcium phosphate to hydroxyapatite: New correlations between X-ray diffraction and infrared data," *Calcif. Tissue Int.*, vol. 58, no. 1, pp. 9–16, 1996.

[61] W. Hędzelek, R. Wachowiak, A. Marcinkowska, and L. Domka, "Infrared spectroscopic identification of chosen dental materials and natural teeth," *Acta Phys. Pol. A*, vol. 114, no. 2, pp. 471–484, 2008.

[62] J. Dietzek, B., Cialla, D., Schmitt, M., Popp, "Introduction to the Fundamentals of Raman Spectroscopy," in *Confocal Raman Microscopy. Springer Series in Optical Sciences*, vol. 158, Berlin, Heidelberg: Springer, 2010.

[63] M. Robin *et al.*, "Insights into OCP identification and quantification in the context of apatite biomineralization," *CrystEngComm*, vol. 22, no. 16, pp. 2728–2742, 2020.

[64] Terrill, N. J., Grant, A. F., Marshall, A. R., Smith, A. D., and Sawhney, K. J., "The non-crystalline Diffraction beamline for Diamond − An Update," *Fibre Diffr. Rev.*, vol. 12, pp. 9–14, 2004.

[65] P. D. Quinn *et al.*, "The Hard X-ray Nanoprobe beamline at Diamond Light Source,"

J. Synchrotron Radiat., vol. 28, pp. 1006–1013, 2021.

[66] O. Glatter, "New Method for Evaluation of Small-Angle Scattering Data," *New Method Eval. Small-Angle Scatt. Data*, vol. 10, pp. 415–421, 1977.

[67] O. Glatter, and O. Kratky, *Small Angle X-Ray Scattering*. London: Academic Press, 1982.

[68] Porod, G., "Die Rontgenkleinwinkelstreuung Von Dichtgepackten Kolloiden Systemen .1.," *Kolloid-Zeitschrift Zeitschrift Fur Polym.*, vol. 124, pp. 83–114, 1951.

[69] M. Basham *et al.*, "Data Analysis WorkbeNch (DAWN)," *J. Synchrotron Radiat.*, vol. 22, pp. 853–858, 2015.

[70] B. R. Pauw, A. J. Smith, T. Snow, N. J. Terrill, and A. F. Thünemann, "The modular small-angle X-ray scattering data correction sequence," *J. Appl. Crystallogr.*, vol. 50, no. 6, pp. 1800–1811, 2017.

[71] V. A. Solé, E. Papillon, M. Cotte, P. Walter, and J. Susini, "A multiplatform code for the analysis of energy-dispersive X-ray fluorescence spectra," *Spectrochim. Acta - Part B At. Spectrosc.*, vol. 62, no. 1, pp. 63–68, 2007.

[72] A. L. Arsenault and M. D. Grynpas, "Crystals in calcified epiphyseal cartilage and cortical bone of the rat," *Calcif. Tissue Int.*, vol. 43, no. 4, pp. 219–225, 1988.

[73] A. L. Arsenault, "Image Analysis of Collagen-Associated Mineral Distribution in Cryogenically Prepared Turkey Leg Tendons," *Calcif Tissue Int*, vol. 48, pp. 56–62, 1991.

[74] G. Boivin, C. Anthoine-Terrier, and K. J. Obrant, "Transmission electron microscopy of bone tissue: A review," *Acta Orthop.*, vol. 61, no. 2, pp. 170–180, 1990.

[75] S. F. Hall CE, Jakus MA, "Electron Microscope Observations of Collagen," *J Am Chem Soc*, vol. 64, pp. 1234–1234, 1942.

[76] W. Traub, T. Arad, and S. Weiner, “Origin of Mineral Crystal Growth in Collagen Fibrils,” *Matrix*, vol. 12, no. 4, pp. 251–255, 1992.

[77] E. A. McNally, H. P. Schwarcz, G. A. Botton, and A. L. Arsenault, “A model for the ultrastructure of bone based on electron microscopy of ion-milled sections,” *PLoS One*, vol. 7, no. 1, pp. 1–12, 2012.

[78] V. Ziv & S. Weiner, “Bone Crystal Sizes: A Comparison of Transmission Electron Microscopic and X-Ray Diffraction Line Width Broadening Techniques,” *Connect. Tissue Res.*, vol. 30, no. 3, pp. 165–175, 1994.

[79] M. J. Turunen *et al.*, “Bone mineral crystal size and organization vary across mature rat bone cortex,” *J. Struct. Biol.*, vol. 195, no. 3, pp. 337–344, 2016.

[80] F. Nudelman, A. J. Lausch, N. A. J. M. Sommerdijk, and E. D. Sone, “In vitro models of collagen biomineralization,” *J. Struct. Biol.*, vol. 183, no. 2, pp. 258–269, 2013.

[81] N. Reznikov, M. Bilton, L. Lari, M. M. Stevens, and R. Kröger, “Fractal-like hierarchical organization of bone begins at the nanoscale,” *Science (80-.).*, vol. 360, no. 6388, May 2018.

[82] A. G. Walton, M. J. Deveney, and J. L. Koenig, “The Raman spectrum of calcified tissue,” *Calcif. Tissue Res.*, vol. 167, pp. 162–167, 1970.

[83] K. Buckley, P. Matousek, A. W. Parker, and A. E. Goodship, “Raman spectroscopy reveals differences in collagen secondary structure which relate to the levels of mineralisation in bones that have evolved for different functions,” *J. Raman Spectrosc.*, vol. 43, no. 9, pp. 1237–1243, 2012.

[84] S. Schrof, P. Varga, L. Galvis, K. Raum, and A. Masic, “3D Raman mapping of the collagen fibril orientation in human osteonal lamellae,” *J. Struct. Biol.*, vol. 187, no. 3, pp. 266–275, 2014.

[85] M. Khalid, T. Bora, A. Al Ghaithi, S. Thukral, and J. Dutta, “Raman spectroscopy detects changes in bone mineral quality and collagen cross-linkage in staphylococcus infected human bone,” *Sci. Rep.*, vol. 8, no. 1, pp. 1–9, 2018.

[86] A. Carden and M. D. Morris, “Application of vibrational spectroscopy to the study of mineralized tissues (review),” *J. Biomed. Opt.*, vol. 5, no. 3, p. 259, 2000.

[87] A. T. C. Wong and J. T. Czernuszka, “Transformation behaviour of calcium phosphate 1. Theory and modelling,” *Colloids Surfaces A Physicochem*, vol. 78, pp. 245–253, 1993.

[88] B. Wingender, "Development of Collagen-Apaptite Composites with Lamellar Microstructures that Template Bone-like Mineral Nanostructures via the PILP Process", PhD thesis, University of Florida, 2017.

[89] L. Brečević and H. Füredi-Milhofer, “Precipitation of calcium phosphates from electrolyte solutions - II. The formation and transformation of the precipitates,” *Calcif. Tissue Res.*, vol. 10, no. 1, pp. 82–90, 1972.

[90] P. T. Cheng, “Formation of octacalcium phosphate and subsequent transformation to hydroxyapatite at low supersaturation: A model for cartilage calcification,” *Calcified Tissue International*, vol. 40, no. 6, pp. 339–343, Nov. 1987.

[91] Y. Xu *et al.*, “Intermolecular channels direct crystal orientation in mineralized collagen,” *Nature Communications*, vol. 11, no. 1, Oct. 2020.

[92] W. Wagermaier, A. Gourrier, and B. Aichmayer, in Materials Design Inspired by Nature: Function Through Inner Architecture, ed. P. Fratzl, J. Dunlop, and R. Weinkamer, The Royal Society of Chemistry, pp. 46-73, 2013.

[93] D. J. Buss, R. Kröger, M. D. McKee, and N. Reznikov, “Hierarchical organization of bone in three dimensions: A twist of twists,” *J. Struct. Biol. X*, vol. 6, pp. 0–9, 2022.

[94] M. D. McKee, D. J. Buss, and N. Reznikov, “Mineral tessellation in bone and the stenciling principle for extracellular matrix mineralization,” *Journal of Structural Biology*, vol. 214, no. 1, p. 107823, 2022.

[95] J. M. Walker, H. J. M. Greene, Y. Moazzam, P. D. Quinn, J. E. Parker, and G. Langer, “An uneven distribution of strontium in the coccolithophore Scyphosphaera apsteinii revealed by nanoscale X-ray fluorescence tomography,” *Environmental Science: Processes & Impacts*, vol. 26, no. 6, pp. 966–974, 2024.

[96] A. Karunaratne, L. Xi, L. Bentley, D. Sykes, A. Boyde, C.T. Esapa, N.J. Terrill, S.D.M. Brown, R.D. Cox, R.V. Thakker, H.S. Gupta,"Multiscale alterations in bone matrix quality increased fragility in steroid induced osteoporosis," *Bone*, vol. 84, pp 15-24, 2016.